Department of Physics and Astronomy
Heidelberg University

Bachelor Thesis in Physics
submitted by

Tim Florian Weinreich

born in Heidelberg (Germany)

June 2024

Ξ-baryon reconstruction with ALICE in LHC Run 3 data

This Bachelor Thesis has been carried out by Tim Florian Weinreich at the
Physikalisches Institut at the University of Heidelberg
under the supervision of
Prof. Dr. Silvia Masciocchi

Abstract

The precise reconstruction of strange baryons such as the Ξ is crucial to study charm baryons via their decay to strange baryons and the production of strange baryons themselves.
In order to extract a signal even in high charged particle multiplicity environments and low transverse momentum regions with high combinatorial background a precise reconstruction of the decay topology is invaluable for obtaining high invariant mass resolutions and reducing background for longer decay chains.
The Kalman Filter Particle (KFParticle) package is a complete reconstruction algorithm for complex decay topologies, fully taking into account the uncertainties of the daughter particles.
In this work, the KFParticle package is used to reconstruct the cascade-like decay structure of the Ξ-baryon in simulated ALICE Run 3 proton-proton data at a centre of mass energy of $\sqrt{s} = 13.6$ TeV. The reconstruction performance is compared to a reconstruction algorithm currently used for ALICE Run 3 data analysis, which is based on the minimisation of the distance of closest approach between daughter tracks. A comparison of the two reconstruction methods regarding secondary vertex, transverse momentum and invariant mass resolutions is presented.
It is demonstrated, that the KFParticle package offers a compatible reconstruction performance while providing the most accurate estimation of secondary vertex uncertainties. For the current ALICE Run 3 reconstruction, it is the optimal choice for the reconstruction of the decay chain of the Ξ baryon.

Zusammenfassung

Die präzise Rekonstruktion von Baryonen mit Strangeness wie dem Ξ ist von entscheidender Bedeutung für die Untersuchung von Charm-Baryonen über ihren Zerfall in Strange-Baryonen und die Produktion von Strange-Baryonen selbst.
Um ein Signal auch in Umgebungen mit einer hohen Multiplizität geladener Teilchen und Regionen mit niedrigem Transversalimpuls, in denen der kombinatorische Hintergrund groß ist, zu extrahieren, ist eine präzise Rekonstruktion der Zerfallstopologie nötig. Dadurch kann der Hintergrund für längere Zerfallsketten reduziert und eine hohe Auflösung der invarianten Masse zu erzielt werden.
Das Kalman Filter Particle (KFParticle) Package ist ein vollständiger Rekonstruktionsalgorithmus für komplexe Zerfallstopologien, der die Unsicherheiten der Tochterspuren vollständig berücksichtigt.
In dieser Arbeit wird das KFParticle Package verwendet, um die kaskadenartige Zerfallsstruktur des Ξ-Baryons in simulierten Run 3 Proton-Proton-Daten bei einer Schwerpunktsenergie von $\sqrt{s} = 13.6$ TeV zu rekonstruieren.
Die Rekonstruktionsleistung wird mit einem Rekonstruktionsalgorithmus verglichen, der derzeitig für die Analyse der ALICE Run 3-Daten verwendet wird und auf der Minimierung des Abstands der engsten Annäherung zwischen den Tochterspuren beruht. Es wird ein Vergleich der beiden Rekonstruktionsmethoden in Bezug auf die Auflösung des sekundären Vertex, des transversalen Impulses und der invarianten Masse vorgestellt.
Es wird gezeigt, dass das KFParticle Package eine kompatible Rekonstruktionsleistung bietet und gleichzeitig die genaueste Abschätzung der sekundären Vertex-Unsicherheiten liefert. Für die aktuelle ALICE Run 3 Rekonstruktion ist es die optimale Wahl für die Rekonstruktion der Zerfallskette des Ξ-Baryons.

Contents

1 Motivation

The investigation of high-energy hadronic collisions plays a crucial role in advancing our understanding of particle physics, particularly in probing the fundamental nature of strongly interacting matter governed by its underlying theory of quantum chromodynamics (QCD).
Unlike up (u) and down (d) quarks, which form ordinary matter, strange (s) quarks are not present as valence quarks in the initial state of high-energy proton-proton (pp) and heavy-ion collisions. Therefore, any strange quarks or antiquarks observed in experiments through measurements of strange hadrons are created during the collision.

The enhanced production of strangeness in heavy-ion collisions compared to pp collisions was historically one of the earliest proposed signatures of the predicted quark-gluon plasma (QGP) [1]. The QGP is a nuclear matter state predicted at extreme temperatures and high baryon chemical potential which is believed to have existed in the first microseconds after the big bang. In the QGP, where quarks and gluons are deconfined and move freely over distances larger than the size of a nucleon, the dominant production mechanism of strange quark and antiquark pairs was found to be gluon-gluon fusion by Müller and Rafelski [2]. The gluon fusion process is fast enough for the abundance of strange quarks to reach its equilibrium value during the lifetime of the QGP resulting in a higher abundance of strangeness per participating nucleon in heavy-ion collisions than in pp collisions.
More recent studies of high-multiplicity pp collisions show observations of strangeness enhancement and several other effects typical of heavy-ion phenomenology in pp interactions [3]. These measurements might be an indication that the phenomenon of QGP is partly independent from the initial collision system and may point towards a common underlying physics mechanism.
Thus, investigating the production of strange hadrons, like the Ξ baryon, in high-energy pp and heavy-ion collisions provides a unique way to study the properties of QCD and the QGP.

The study of heavy-flavour hadron production in high-energy pp collisions provides fundamental tests of perturbative quantum chromodynamic calculations. Furthermore, these measurements serve as a valuable reference point for studying heavy-ion collisions, where heavy-flavour hadrons act as sensitive probes for the predicted QGP. Unlike strange or even lighter quarks, charm (c) and beauty (b) quarks can only be produced in the initial hard scattering of the collision due to their large masses. Consequently, they experience the complete lifetime and evolution of the QGP, while interacting with the medium through exchange of energy and momentum.
The production cross section ratios of heavy-flavour hadrons are sensitive to the so-called *fragmentation functions* which describe the transition of a heavy quark into a specific hadron species. While they were previously assumed to be universal across different collision systems, recent measurements of charm-quark fragmentation fractions into various charmed hadron species in ultra-relativistic pp collisions show a deviation from measurements in e^+e^- and e^-p collisions and thus indicate a non-universal charm fragmentation [4–6]. These measurements allow the investigation of different possible hadronisation mechanisms which are at play in high energy pp collisions. In order to systematically study the modification of the fragmentation for different collision systems, the measurements of the charmed hadron production cross sections need to be as precise as possible over the entire transverse momentum (p_{T}) range of the heavy-flavour hadron. Extending the measurements of the charm hadron production cross-sections to low p_{T}, which is the main contribution to this cross-section, would also enable a more precise measurement of the total charm production cross-section.
The latest p_{T}-differential cross section measurement of the Ξ_c^+ baryon in ALICE is shown as the blue markers in figure 1 [7]. The measurement was performed in pp collisions at a centre of mass energy of $\sqrt{s} = 13$ TeV recorded by the ALICE detector during LHC Run 2 in the transverse momentum range $3 < p_{\mathrm{T}} < 12$ GeV/c. The Ξ_c^+ baryon was reconstructed via its hadronic decay channel $\Xi_c^+ \rightarrow \Xi^-\pi^+\pi^+$. With the upgraded ALICE detector capable of measuring the high interaction rates of the currently ongoing Run 3 at the LHC, the new data will allow to extend this measurement to even lower p_{T}. In the low transverse momentum region the combinatorial background of the reconstruction via the hadronic decay channel is very high due to the increased production rates of primary pions. For the reconstruction of the Ξ_c^+ vertex, the reconstructed Ξ baryon is combined with two charged primary pion tracks. Furthermore, a precise vertex reconstruction together with the high data-taking rates will make the measurement of the Ξ_c^+ in Run 3 heavy-ion collisions possible, where the charged particle multiplicity is increased compared to pp collisions.

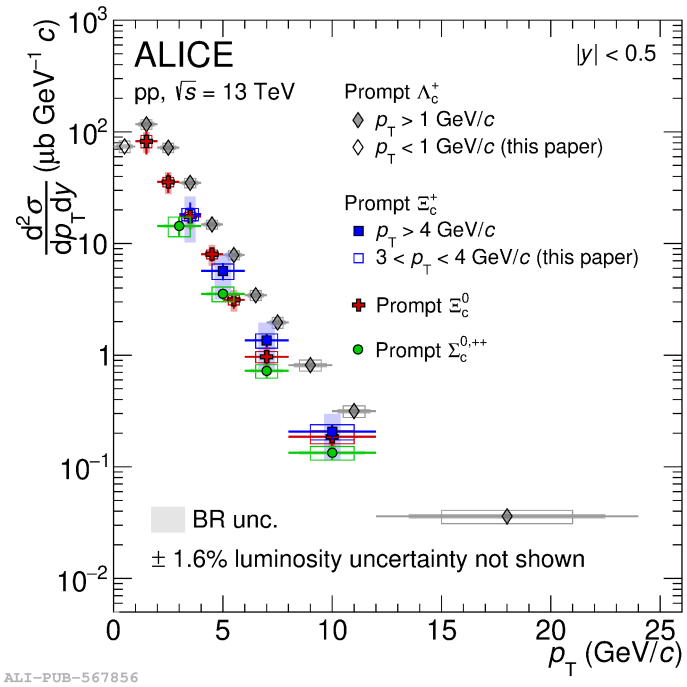

Figure 1: p_{T}-differential production cross sections of prompt Λ_c^+, Ξ_c^0, Ξ_c^+, and $\Sigma_c^{0,++}$ baryons at midrapidity ($|y| < 0.5$) in pp collisions at $\sqrt{s} = 13$ TeV. The statistical (systematic) uncertainties are shown as vertical bars (boxes). The shaded boxes report the BR uncertainty. Figure taken from [4]

.

In summary, the precise reconstruction of strange baryons like the Ξ is crucial not only to study charm baryons, in particular the Ξ_c^+, via their decay to strange baryons but also to study the production of strange baryons themselves. Both analyses contexts require an accurate extraction of signal even in high charged particle multiplicity environments and low transverse momentum regions with high combinatorial backgrounds. A precise reconstruction of the entire decay topology becomes pivotal for obtaining high invariant mass resolutions and reducing background for longer decay chains over the entire p_{T} range.

This work aims to contribute to enhancing the reconstruction precision of the Ξ baryon decay to a Λ baryon and a pion. A comparison of the performance of the KFParticle package for decay chain reconstruction and the reconstruction algorithm currently used for ALICE Run 3 data analysis is presented.

2 ALICE detector and tracking of charged particles

2.1 Detector overview

The A Large Ion Collider Experiment (ALICE) detector at CERN's Large Hadron Collider (LHC) is a general-purpose detector for relativistic heavy-ion and proton-proton collisions to study the physics of strongly interacting matter at extreme energy densities and is designed specifically for the study of the quark-gluon plasma.
For the current Run 3 at the LHC, the ALICE detector was upgraded in the Long Shutdown 2 from 2019 to 2021 to cope with the high interaction rates reached in Run 3 which require a continuous readout of data, and to enhance the capabilities of the detector for precise tracking in high charged particle multiplicity environments. To fulfil its physics objectives, ALICE aims to collect data in Run 3 at the target interaction rate of 50 kHz for heavy-ion and up to 1 MHz for proton-proton collisions.

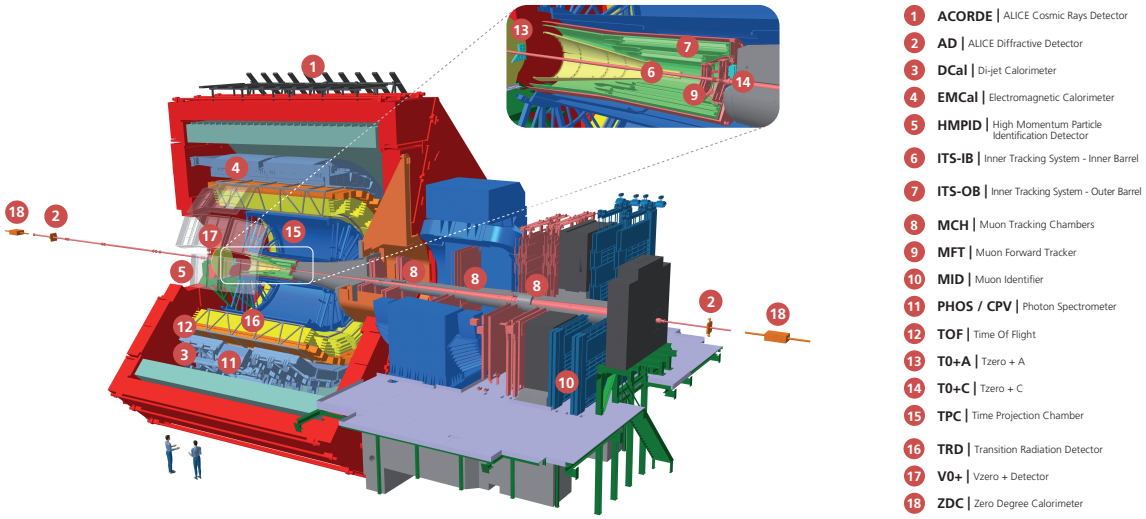

Figure 2: Schematic view of the ALICE-detector with its subdetector systems during Run 3 [8].

The ALICE detector is a complex apparatus comprising several different subdetector systems. Most of these are arranged in layers around the beam pipe as seen in figure 2 in the so-called *central barrel*. The detector is designed for various purposes, including tracking, particle identification, and calorimetry. Especially for tracking and identification of particles, the new Inner Tracking System of Run 3 (ITS2) and the Time Projection Chamber (TPC), both located in the central barrel, play pivotal roles. The entire central barrel is embedded in a large solenoid magnet reused from the L3 experiment at LEP which provides a magnetic field of 0.5 T parallel to the beam axis.

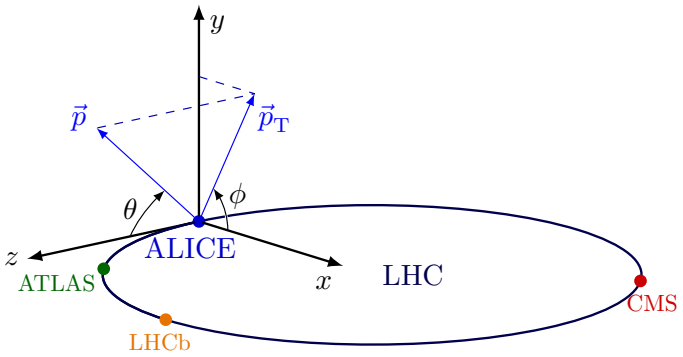

Figure 3: Sketch of the ALICE coordinate system and the LHC.

A Cartesian coordinate system defined for ALICE according to the standard rules of the LHC is

illustrated in figure 3. The point of origin denotes the nominal interaction point (IP) in the centre of the detector with the z-axis aligned parallel to the mean beam direction, the x-axis points towards the centre of the LHC, and the y-axis is oriented vertically upwards. Because the central barrel tracking detectors are mostly radially symmetrical in the xy-plane the kinematics of a particle inside the detector are often described by three independent variables, its momentum in xy-direction, referred to as transverse momentum p_{T} (here $p_{\mathrm{T}} = |\vec{p}_{\mathrm{T}}|$), the azimuth angle ϕ and the polar angle θ. To describe the polar angle dependency, θ is typically replaced by the pseudorapidity η, which is Lorentz-invariant along the z-axis.

2.1.1 Inner Tracking System

The ITS2, as shown in the enlarged image section of figure 2, is the innermost subdetector system of ALICE in the central barrel. It consists of seven cylindrical layers of silicon pixel detectors. The first three layers are grouped in the so-called inner barrel which is located only a few centimetres away from the beam pipe and thus optimised to achieve an improved performance in terms of pointing resolution to the IP. The outer barrel is arranged in two double layers with different radial positions which can be found in table 1. The whole ITS2 is designed to optimise p_{T} resolution and tracking efficiency for low p_{T}-particles in the high track-density environment of Pb–Pb collisions.

	Inner barrel			Outer barrel			
Layer number	0	1	2	3	4	5	6
Average radius [mm]	23	31	39	196	245	344	393

Table 1: Average radial positions of ITS2 layers [9].

The pseudorapidity coverage of the detector is $|\eta| < 1.22$ at full azimuthal coverage for interaction vertices located in the range of approximately $\pm 10\,\mathrm{cm}$ around the nominal interaction point along the beam axis. The total surface area of the sensors is $\approx 10\,\mathrm{m}^2$ instrumented with about 12.5 billion pixels with binary readout providing a spatial resolution ($r\phi \times z$) of $5\,\mu\mathrm{m} \times 5\,\mu\mathrm{m}$ [9].
The main tasks of the ITS2 are charged particle tracking for both primary and secondary particles even down to low p_{T} and the reconstruction of the primary vertex (PV), which is the measured collision point. Its small spatial resolution allows measuring the distance of closest approach (DCA) between the trajectory of tracks and the PV, which is often referred to as *impact parameter*, with high precision of only up to $30\,\mu\mathrm{m}$ spatial resolution even for low transverse momentum particles ($p_{\mathrm{T}} < 1$ GeV/c) [10]. Furthermore, a precise reconstruction of decay points or secondary vertices of short-lived hadrons is possible. Both are fundamental quantities for the reconstruction of weakly decaying strange hadrons like the Ξ and especially heavy flavour hadrons.

2.1.2 Time Projection Chamber

The TPC is a large gaseous detector that envelops the ITS2 and plays a central role in reconstructing charged particle trajectories in three dimensions. Its cylindrical design covers a broad pseudorapidity range of $|\eta| < 0.9$ for particles produced in the collision.
The primary functions of the TPC are charged particle tracking and particle identification (PID) through the measurement of the mean specific ionisation energy loss per unit path length $\langle dE/dx \rangle$ and the momentum of charged particles.
In the $88\mathrm{m}^3$ of active gas volume charged particles ionise the gas and the resulting free electrons drift towards the segmented endplates of the TPC. The gas mixture, a specific combination of the noble gas neon with carbon dioxide and nitrogen, enables efficient ionisation and drift of the particles in the electric field of the TPC and at the same time provides small radiation lengths and low multiple scattering rates. Then at the endplates, the electron signal is amplified by Gas Electron Multiplier (GEM) chambers for readout. Using the timing information of the signal to reconstruct the position along the beamline and the signal position on the readout plate, the three-dimensional trajectory of the charged particle can be reconstructed. The PID information is then extracted by comparing the measured energy loss in the TPC with the expected dE/dx for a specific particle species and momentum parameterised by the Bethe-Bloch equation.

For Run 3, the TPC underwent upgrades to cope with high interaction rates of up to 50 kHz for heavy nuclei collisions where on average tracks from five collisions pile up in the gas volume during the TPC drift time window of 100 µs. With triggered readout not all of these interactions can be read out, thus requiring a continuous readout mode. So the GEM chambers were introduced for signal amplification to enable continuous readout, allowing for a full reconstruction of all collisions. At such high interaction rates the amount of positive ions produced in the amplification region would lead to substantial space-charge distortions because these positively charged ions would drift back into the drift volume of the TPC, where they can accumulate and distort the electric field hence the name space-charge distortions. The GEM chambers provide a viable solution to this challenge by efficiently blocking the path of back-drifting ions and thus fulfil the requirement to keep the ion-induced space-charge distortions at a tolerable level of up to 2% [9].

2.2 Track and vertex reconstruction

A collision occurring with a single primary interaction point, or primary vertex, around which various tracks are measured within the detector is referred to as an *event*. Particle tracking within the ITS2 and the TPC, in general, the entirety of the central barrel, is crucial for the reconstruction of an event. Each charged particle generates signals, such as hits in the ITS2 layers or ionisation of the gas in the TPC, enabling the measurement of its spatial position within the detector. The goal of event reconstruction is to assign these spatial points to individual tracks and reconstruct their corresponding kinematics. This task presents significant challenges, primarily due to the high density of charged particles involved in track finding and especially due to the continuous data readout mode in Run 3.
Tracking in the central barrel comprises multiple reconstruction steps. Initially, the clusterisation process is performed separately for each detector converting detector signals into clusters characterised by the positions, signal amplitudes, and their corresponding errors. These clusters can be interpreted as the crossing point of a particle traversing the detector.
The first step in track reconstruction involves estimating a preliminary interaction vertex using clusters in the inner barrel of the ITS2. In Run 3, track finding in the TPC and ITS2 start separately from each other, as the TPC is read out continuously. With the absence of a trigger, hits in the TPC do not have a relatively well-defined z-position as in the case of triggered data readout but only a time value. This is due to the z-position depending on the time of the interaction that produced the measured hit, which is ambiguous in continuous readout. ITS2 standalone tracking is mandatory since extrapolating TPC tracks into the ITS2 is infeasible due to the lack of an absolute z-coordinate in the TPC before the TPC tracks are matched with tracklets in the ITS2.
Track finding starts in the outermost regions of the TPC by building track seeds from two aligned clusters at large radii and the estimated interaction vertex as a constraint. These seeds are then propagated inwards and updated with matching clusters in the vicinity of the estimated trajectory of the particle by using the Kalman Filter algorithm. At this stage, a preliminary PID based on the energy loss due to ionisation is determined for the propagated tracks. Track finding in the ITS2 follows in principle the same scheme used for the TPC but taking into account the higher track density. Finally, tracks reconstructed in the TPC and the ITS2 are matched in a compatible time window, which fixes the time and thus the z-position of the TPC tracks. Unused clusters from the standalone ITS2 tracking are then matched again to tracks reconstructed in the TPC in the so-called *Afterburner algorithm*. This is important to reconstruct V0 or Cascade particles like the Ξ baryon because they mainly decay inside the ITS2 and thus their daughter particles may only produce hits in the outer layers of the ITS2.
In the second step, the reconstructed and matched tracks are propagated in the outward direction using the Kalman Filter and clusters found in the track-finding stage. At each updating step, several pieces of information are updated until the filtering reaches the outer layers of the TPC, where an attempt is made to match tracks with clusters in the Transition Radiation Detector and the Time of Flight Detector, respectively. In a similar way, the tracks are then matched with signals in the Electromagnetic Calorimeter, the Photon Spectrometer, and the High Momentum Particle Identification Detector.
In the last step, the reconstructed tracks are again propagated from the outer radius of the TPC inwards to the innermost update (IU) which is the spatial point of the closest measurement of the track to the interaction vertex. This final refit is performed by combining tracking information from multiple subdetectors and using the full PID information. At the IU, the track state vector parameters together with its covariance matrix are determined. The last stage of the event reconstruction procedure is the final determination of the PV by a precise vertex fit.

2.3 Multiple scattering

After a charged particle passes through a material of thickness x, it has typically undergone numerous small-angle scattering events, resulting in a statistical distribution of the scattering angle relative to its original direction. In the relevant energy range, the charged particles are predominantly scattered in the Coulomb fields of the nuclei in the traversed medium. In the case of ALICE, the particles pass the detector material, e.g. the layers of the ITS2 or the TPC gas, and air in between the various detector layers. For these cases, it can be assumed that enough small-angle scatter processes occur to expect that the distribution of the scattering angle is Gaussian according to the central limit theorem [11]. An approximation of the root mean square or width of the angular distribution projected onto a plane perpendicular to the direction of motion of the incoming particle $\theta^{\text{rms}}_{\text{plane}}$ is given by the so-called *Highland formula*

$$\theta^{\text{rms}}_{\text{plane}} = \frac{13.6\,\text{MeV/c}}{p\beta} z \sqrt{\frac{x}{X_0}} (1 + 0.038 \ln \frac{x}{X_0}) \propto \frac{1}{p} \tag{1}$$

where p is the momentum, β is the ratio of the velocity to the speed of light and z is the charge number of the incoming particle passing through a medium of thickness x/X_0 in units of radiation length. The radiation length of a material is defined as the mean distance over which a high-energy electron loses all but $1/e$ of its energy by bremsstrahlung. The radiation length appears here because it characterises processes in the Coulomb field of a nucleus, as it does for the bremsstrahlung of electrons in the field of a nucleus, for which X_0 has been defined. As $\theta^{\text{rms}}_{\text{plane}} \propto \frac{1}{p}$, high momentum particles are less affected by multiple scattering. In general, multiple scattering limits the momentum and tracking resolution of the detector, particularly at low momentum [11].

2.4 Track parameter resolution

2.4.1 Transverse momentum resolution

The momentum of a charged particle can be determined by tracking its path in a magnetic field. A particle with momentum p and charge q traversing a magnetic field with strength B is deflected by the Lorentz force. The solution of the equation of motion describes a rotating velocity vector with constant magnitude in the plane perpendicular to the magnetic field. The radius of curvature of this circular motion in the plane perpendicular to the magnetic field is given by equation 2

$$R = \frac{p_{\text{T}}}{|q| \cdot B} \quad \Rightarrow \quad p_{\text{T}} = |q| \cdot B \cdot R \tag{2}$$

where p_{T} is the transverse momentum, the momentum component in the plane perpendicular to the magnetic field, of the incoming particle. It is related to its absolute momentum by $p = p_{\text{T}}/\sin\theta$ with the angle θ between the momentum direction and the direction of the magnetic field. As discussed in section 2.1, ALICE uses a solenoid magnet that provides a magnetic field of 0.5 T parallel to the beam axis and therefore θ is equal to the polar angle. Thus, measuring the trajectory of a particle inside the detector, which measures the radius of curvature and the polar angle, determines the transverse and absolute momentum if the charge of the particle is known.
The resolution of the transverse momentum measurement can typically be described by the following common parameterisation

$$\frac{\sigma_{p_{\text{T}}}}{p_{\text{T}}} = \sqrt{\left(\frac{\sigma_{p_{\text{T}}}}{p_{\text{T}}}\right)^2_{meas} + \left(\frac{\sigma_{p_{\text{T}}}}{p_{\text{T}}}\right)^2_{scat}} \tag{3}$$

The first contribution scales linearly with p_{T} and is caused by the limited resolution of the position measurements inside the detector, which complicates measuring the radii of curvature of tracks corresponding to high-momentum particles as their tracks become straighter. The second, constant contribution is due to multiple scattering in the detector material discussed in section 2.3 and dominates the transverse momentum resolution for low p_{T} particles [11].

2.4.2 Impact parameter resolution

As described in section 2.1.1, the impact parameter d is defined as the distance of closest approach between the reconstructed trajectory of a track and the primary vertex. It is determined by extrapolating the tracks from their innermost measurement point to the point of closest approach to the primary vertex. The impact parameter is used as a selection criterion that allows selecting whether tracks come from the primary or a secondary vertex. The significance of the impact parameter determination is given by the ratio of the determined value to its resolution, d/σ_d.
In an approximation, the impact parameter resolution σ_d can be described by two separate contributions presented in equation 4.

$$\sigma_d = \sqrt{(\sigma_d)^2_{meas} + (\sigma_d)^2_{scat}} \tag{4}$$

Similar to equation 3, the first contribution is due to the limited resolution of the position measurements inside the detector. It depends on the ratio of the extrapolation lever arm to the length over which the track measurements are distributed and the total number of measurements. Thus, as the innermost measurement point of a track moves away from the primary vertex the resolution decreases and vice versa. Since this contribution primarily depends on the geometry of the detector and the extrapolation position, it is referred to as *geometric effect* in the following. The second contribution is caused by multiple scattering discussed in section 2.3 and is therefore especially relevant for tracks belonging to low p_{T} particles. Furthermore, it depends on the amount of material in the extrapolation length i.e. the material between the innermost measurement point and the primary vertex.
The previous considerations are not only valid for the impact parameter resolution of a track to the primary vertex but also for the position resolution of tracks extrapolated to the point of closest approach to a secondary vertex.

3 Analysis strategy and methodology

3.1 Decay chain reconstruction

Ξ baryons are baryons that consist of two strange quarks and either one up or down quark. They are characterised by their different electrical charges: Ξ^- (dss), Ξ^+ ($\bar{\mathrm{d}}\bar{\mathrm{s}}\bar{\mathrm{s}}$), Ξ^0 (uss). In a broader sense, Ξ baryons also include baryons in which one or both strange quarks are replaced by a heavier charm or bottom quark i.e. the Ξ_c^+ baryon (usc) which can decay into a Ξ^- baryon. For notation, the subscripts "c" and "b" are added for each heavy charm or bottom quark that replaces one of the two strange quarks.

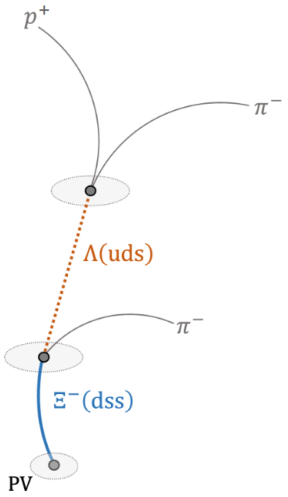

Figure 4: Sketch of the dominant cascade decay (BR = 99.9%) of a prompt Ξ^- baryon.

Figure 4 schematically shows the weak hadronic decay of a prompt Ξ^- baryon, where prompt means that the Ξ^- baryon is created in the primary vertex of the collision and not created as a secondary particle like in the decay of the Ξ_c^+ baryon. The Ξ^- baryon decays into a Λ baryon and a π^- which is often called *bachelor particle*. The Λ baryon has no electric charge and thus cannot be measured directly by the detector, but it decays further into a p^+ and a π^-. Because of this characteristic decay into two charged particles, which are measured as a V-shape in the detector, the Λ baryon is often referred to as a *V0 particle*. An overview of the particles involved in the decay chain of the Ξ^- baryon with values from the Particle Data Group is given in table 2.

particle	quark content	mass [GeV/c^2]	decay length cτ [cm]
Ξ^-	dss	1.32171 ± 0.00007	4.9136
Λ	uds	1.115683 ± 0.000006	7.8905
p^+	uud	$0.93827208816 \pm 0.00000000029$	-
π^-	$\bar{\mathrm{u}}$d	0.13957039 ± 0.0000001	780.99

Table 2: Properties of particles involved in the Ξ^- decay chain [12].

Here, cτ denotes the proper lifetime or the mean decay length of the corresponding decaying particles. The Ξ^- baryon together with the Ξ^+ baryon, which has the same decay topology as the Ξ^- baryon but with the corresponding antiparticles, is reconstructed via the discussed weak hadronic decay. Because of the two-stage decay into lighter particles, the Ξ baryons are often called *cascade particles*. These complex decay topologies require a precise vertex reconstruction and can be used to compare different reconstruction algorithms and their performance.

One method of reconstructing such short-lived particles is by determining the secondary vertex of their decay as the point at the distance of closest approach (DCA) between the daughter particle trajectories. In the case of a two-body decay like the hadronic decay of the Ξ baryon, it is the centre of the line connecting the trajectories of the daughter particles at their point of closest approach. Determining

the DCA between trajectories in 3d space from a finite amount of measurements is a complex process. The mother particle is then directly reconstructed by extrapolating the parameters of the daughter particles to that vertex, where their momentum and energy are summed up taking into account the conservation of energy and momentum. In the current Run 3 data taking, ALICE is using a vertexing algorithm which is based on the minimisation of the DCA between daughters which will be called *DCA fitter* in the following. For the reconstruction of the mother particle, the DCA fitter treats the momentum and spatial coordinates of the daughter particles separately and thus neglects the correlations between them. The DCA fitter is therefore not able to fully consider the entire covariance matrix of the daughter tracks in the reconstruction of the mother particle and concentrates on the reconstruction of the production and decay vertices.

The KFParticle package [13–15], on the other hand, provides a method for the estimation of the parameters and the entire covariance matrix of decayed particles in addition to the reconstruction of the production and decay vertices. It has been developed by the CBM collaboration and is a flexible software framework based on the Kalman filter designed for vertex reconstruction in high-energy physics experiments. Case studies and examples of its successful implementation in various experiments further demonstrate its versatility and reliability in short-lived hadron reconstruction [16] [17].
Kalman filtering is a mathematical algorithm used to estimate the state of a dynamic system based on a series of measurements with their introduced noise. Given a finite set of such measurements, it provides an optimal estimation for the state vector r and its covariance matrix C which describe the state of the dynamic system. In the general case, r and C can change between two measurements. For example, a charged particle moving through a detector experiences multiple scattering and energy losses altering its trajectory between hits or crossing points in the detector. Kalman filtering allows to properly handle not only measurements with their introduced errors but also the effects of propagation between measurements with their process noise. This makes the use of the Kalman filter natural for the reconstruction of high-energy physics events.
For the complete reconstruction of short-lived hadrons and their decay chains, the KFParticle package follows the general algorithm of the Kalman filter. Therefore mother and daughter particles are described with the same state vector components, given in equation 5, and associated covariance matrix components.

$$r = (x, y, z, p_x, p_y, p_z, E, s)^T \tag{5}$$

The KFParticle package parameterises all particles using key quantities such as spatial coordinates x, y, z, three components of momentum p_x, p_y, p_z, and energy E in the state vector. The parameter $s = \frac{l}{p}$, where l is the length of the particle trajectory in the laboratory coordinate system and p is the momentum, is used to transport the particle between the decay and production vertex on its trajectory. After the optimal estimator of the state vector is obtained, additional physical parameters of the particle such as mass, momentum, decay length, lifetime and rapidity can be easily calculated.
The first step in the reconstruction of a decayed mother particle is the initialisation of the state vector and associated covariance matrix at the decay vertex without the parameter s because the production vertex is not known at that stage. Given a finite number of reconstructed daughter particles, the estimates of r and C of the mother particle are iteratively updated for every daughter particle. That means every daughter serves as a measurement for the state vector of the mother particle. Often it is possible to improve the estimate of the state vector of the mother particle by applying a mass constraint, so to require all daughter particles to form the invariant mass of the reconstructed particle. This is particularly important for long decay chains like the hadronic decay of the Ξ baryon, where the mass distribution of the reconstructed Λ baryon introduces uncertainty to the mass of the reconstructed Ξ baryon. In the last optional step, all parameters of the mother particle are transported to its production vertex, which is also used as a measurement for the filtering of the particle's parameters at this vertex. After constraining the mother particle to its production vertex, the parameter s is added to the state vector. The final optimal estimation of the state vector and its covariance matrix contains all the information needed to obtain a full description of the particle. In summary, KFParticle allows the determination of a particle's decay vertex to its full extent, while fully considering the uncertainties of each daughter track.

The analysis presented in this work provides a comparison between the KFParticle package and the DCA fitter which are used to reconstruct the cascade-like decay structure of the Ξ-baryon with all its daughter particles. Their reconstruction performance is compared regarding secondary vertex, transverse momentum, and invariant mass resolutions of the Ξ baryon and its daughters.

3.2 Residuals and pulls

One way to test the performance of the two discussed reconstruction algorithms is to investigate the residual and pull distributions for different parameters. Residuals and pulls are indispensable statistical analysis tools providing a quantitative assessment of the agreement between experimental observations and theoretical predictions.

Residuals, in the context of particle physics analyses, represent the discrepancies between observed experimental data and the predictions derived from theoretical models or Monte Carlo simulations. In this thesis, Monte Carlo simulations are used to simulate pp collisions in the ALICE detector and provide the generated value of a parameter e.g. the generated momentum of a generated Ξ baryon. The reconstruction of the Ξ baryons itself is then performed in the generated events using the two reconstruction algorithms discussed in section 3.1. Therefore, the reconstructed value of a parameter, e.g. the reconstructed momentum of a reconstructed Ξ baryon, is not observed experimental data but rather the output of the two different reconstruction algorithms reconstructing the Ξ baryon in the generated events, which is ideal to compare their performance. Mathematically, the residual of a parameter p is the difference between the reconstructed or fitted value p^{Rec} and the generated value p^{MC}:

$$\text{residual} = p^{\mathrm{Rec}} - p^{\mathrm{MC}} \tag{6}$$

In the best case, the residuals exhibit a symmetric distribution around 0. An asymmetric or shifted distribution can be an indication for a bias in the reconstruction of a investigated parameter. The width of the residual distribution determines the accuracy or resolution of the reconstruction. If the distribution is narrow and symmetric around 0, the reconstruction of the investigated parameter is non-biased and has a higher resolution than with a broader residual distribution.
Especially when discussing momentum residuals the actual distribution will be scaled by the generated value p^{MC}:

$$\text{scaled residual} = \frac{p^{\mathrm{Rec}} - p^{\mathrm{MC}}}{p^{\mathrm{MC}}} \tag{7}$$

This scaled residual has the advantage of being a dimensionless quantity which represents the relative deviation of the reconstructed value to the simulated value. For example, if a scaled residual distribution has a mean of 0.03, there is a bias to reconstruct 3% larger values of the parameter compared to the simulated value.

Pulls, closely related to residuals, provide a standardised measure for the significance of the deviation between experimental data and theoretical expectations. The pull is defined as the residual divided by the corresponding measurement uncertainty of the reconstructed parameter, σ_p^{Rec}. In the case of the reconstructed vertex or mother particle, σ_p^{Rec} is obtained from the covariance matrix of the fit. The pull is calculated as:

$$\text{pull} = \frac{p^{\mathrm{Rec}} - p^{\mathrm{MC}}}{\sigma_p^{\mathrm{Rec}}} \tag{8}$$

The pull quantifies how many standard deviations the reconstructed data deviates from the simulated values and allows for checking whether the uncertainties are correctly estimated or calculated during the reconstruction. In the case of correctly handled uncertainties, the distribution of the pulls should resemble a Gaussian distribution with mean $\mu = 0$ and standard deviation $\sigma = 1$, or a standard normal distribution. If $\sigma < 1$, the uncertainties are overestimated and vice versa.

3.3 Multi-Gaussian fits

The investigation and characterisation of pull distributions often involve the fitting of probability density functions (PDFs) to quantify the agreement between experimental data and theoretical expectations. In a first approximation, the width of a pull distribution can be extracted by fitting it with a Gaussian of the form

$$\mathrm{G}(x; A, \mu, \sigma) = \frac{A}{\sigma\sqrt{2\pi}} \exp\left(-\frac{(x-\mu)^2}{2\sigma}\right), \tag{9}$$

where μ is the mean or expectation of the distribution, while σ is its standard deviation and A is a normalisation constant.
Pull distributions can exhibit intricate shapes due to several effects such as systematic uncertainties of the experimental measurement which arise from imperfect calibrations or detector effects. Other effects might be correlations between the measured value of a reconstructed parameter and its uncertainties or imprecise assumptions and models used in the reconstruction process. A simple Gaussian profile might therefore not be a suitable description of the distribution. In practice, it often underestimates the tails or does not capture asymmetries of the distribution. A more general approach is a fit of multiple Gaussians for a better description of the described complexities. Let n be the number of individual Gaussians, then the overall fit-function is of the form:

$$\mathrm{G}_n(x; A_1, ..., A_n, \mu_1, ..., \mu_n, \sigma_1, ..., \sigma_n) = \sum_{i=1}^{n} \frac{A_i}{\sigma_i\sqrt{2\pi}} \exp\left(-\frac{(x-\mu_i)^2}{2\sigma_i}\right) \tag{10}$$

To prevent overfitting and to keep the balance between needed accuracy and computational expense it is in practice often sufficient to use a double or triple Gaussian, the sum of two or three Gaussians. In order to obtain the position and the width of the fitted distribution, the extracted values for the means μ_i and standard deviations σ_i are weighted with the corresponding amplitudes A_i:

$$\mu_w = \frac{\sum_{i=1}^{n} A_i \cdot \mu_i}{\sum_{i=1}^{n} A_i} \quad ; \quad \sigma_w = \frac{\sum_{i=1}^{n} A_i \cdot \sigma_i}{\sum_{i=1}^{n} A_i} \tag{11}$$

In the case of correctly handled uncertainties, the distribution should have a weighted mean $\mu_w = 0$ and weighted standard deviation $\sigma_w = 1$ if the errors of the various effects that contribute to the pull distributions are Gaussian distributed.

3.4 Fits for invariant mass distributions

The study of particle decays and resonances in high-energy physics often involves the analysis of invariant mass distributions. In the case of a high enough detector resolution, these distributions provide crucial insights into the properties of particles, including their masses, widths, and lifetimes. Thus, the choice of an appropriate fit-function for fitting invariant mass distributions to accurately model the observed data becomes pivotal.

Invariant mass distributions arising from particle decays or resonances can exhibit complex shapes that are not adequately described by simple analytical functions. In general, the invariant mass distribution of a particle follows a relativistic Breit-Wigner (or Lorentzian) distribution according to equation 12 if the resolution of the detector is high enough to resolve the natural decay width of the particle.

$$\mathrm{BW}(E; M, \Gamma) = \frac{k}{(E^2 - M^2)^2 + M^2\Gamma^2}, \quad k = \frac{2\sqrt{2}M\Gamma\gamma}{\pi\sqrt{M^2+\gamma}} \quad \text{and} \quad \gamma = \sqrt{M^2(M^2+\Gamma^2)} \tag{12}$$

In this case, E is the centre-of-mass energy that produces the resonance or decayed particle, M is the mass of the resonance or decayed particle, and Γ is the resonance or decay width, related to its mean lifetime according to $\tau = 1/\Gamma$.

If the resolution is not high enough, the distribution will follow a Gaussian distribution according to equation 9 or has at least Gaussian components. Other complexities arise from instrumental effects such as detector efficiencies, experimental uncertainties, and background contributions which can introduce asymmetric broadening or tails in the invariant mass distribution.

The Voigt profile, a convolution of the Gaussian and Lorentzian distributions, presents an elegant solution to address the shortcomings of simplistic models when describing invariant mass distributions.

$$\mathrm{V}(x; A, \mu, \sigma, x_0, \gamma) = \int_{-\infty}^{\infty} \mathrm{G}(x'; A, \mu, \sigma)\mathrm{L}(x - x'; x_0, \gamma)dx', \quad \mathrm{L}(x; x_0, \gamma) = \frac{\gamma}{\pi((x - x_0)^2 + \gamma^2)} \tag{13}$$

where $\mathrm{G}(x'; A, \mu, \sigma)$ is the Gaussian profile according to equation 9 and $\mathrm{L}(x; x_0, \gamma)$ is the Lorentzian profile where x_0 determines the position of the maximum and γ being the width of the curve. It combines the Gaussian and the Lorentzian shape into a single, versatile function taking into account both the normal distribution of events and the natural decay widths of decaying particles.

Another compelling choice due to its versatility in capturing various features encountered in experimental data is the Double-sided Crystal Ball (DSCB) function:

$$\mathrm{DSCB}(x; N, \mu, \sigma, n_1, n_2, \alpha_1, \alpha_2) = N \cdot \begin{cases} e^{-0.5\alpha_1^2} \cdot \left(\frac{n_1}{\alpha_1}\right)^{n_1} \cdot \left(\frac{n_1}{\alpha_1} - \alpha_1 - t\right)^{-n_1} & \text{if} \quad t < -\alpha_1 \\ e^{-0.5t^2} & \text{if} \quad -\alpha_1 \leq t \leq \alpha_2 \\ e^{-0.5\alpha_2^2} \cdot \left(\frac{n_2}{\alpha_2}\right)^{n_2} \cdot \left(\frac{n_2}{\alpha_2} - \alpha_2 - t\right)^{-n_2} & \text{if} \quad t > \alpha_2 \end{cases} \tag{14}$$

where $t = (x - \mu)/\sigma$, N is a normalisation parameter, μ is the peak position of the Gaussian distribution, σ represents the width of the Gaussian part of the function, α_1 (α_2) parameterises the mass value where the distribution of the invariant mass becomes a power-law function on the low-mass (high-mass) side, with n_1 (n_2) being the exponent of this function.
The Double-sided Crystal Ball function presents a robust solution that effectively models complex signal shapes within the invariant mass distributions. It accommodates asymmetric tails on both sides of the peak, providing a more realistic representation of the non-Gaussian shapes often observed in experimental data.

4 Signal extraction studies in data

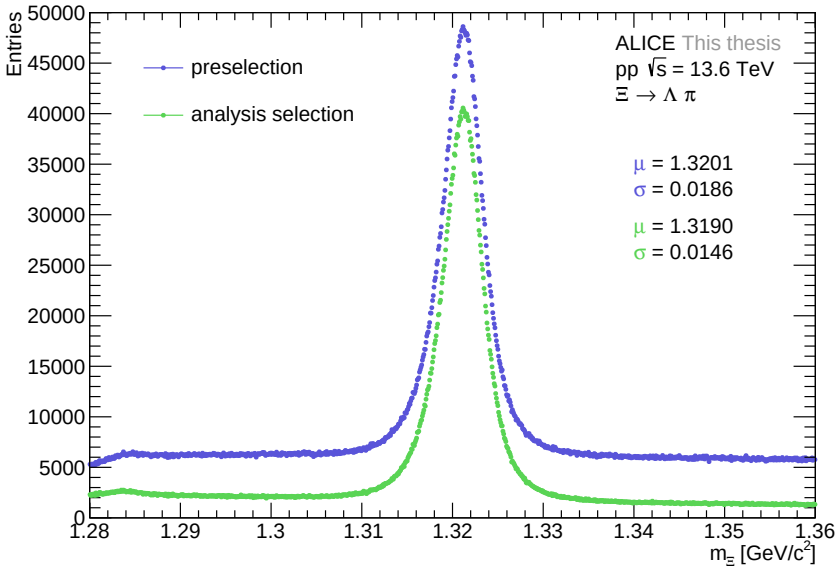

Figure 5: Invariant mass distributions of reconstructed cascade candidates with preselection criteria, shown in table 9, applied (blue markers) and with analysis selection criteria as listed in table 3 applied (green markers).

In this work, the $\Xi^{\pm}$ candidates are reconstructed via their hadronic decay chain discussed in section 3.1 by combining a pion with a Λ baryon, which is reconstructed from a proton and a pion itself.
For the first part of the analysis, the used data sample consists of pp collisions at the centre-of-mass energy $\sqrt{s} = 13.6$ TeV recorded by ALICE in 2022 during Run 3. The cascade candidates are reconstructed with the KFParticle package and preselected based on the topological selection criteria listed in table 9 in the appendix. In addition, a mass constraint to the Λ mass is applied on the V0 candidates in the decay chain. The analysed sample consists of 1.7 billion events with approximately 20 million cascade candidates.
In general, the number of signal candidates, or the number of Ξ baryons, is extracted from a fit to the invariant mass spectrum of all candidates, so both signal and background candidates. The background candidates stem mainly from combinatorial effects in the reconstruction of the Ξ baryon, so the random mismatch of two particles which are combined to reconstruct a cascade candidate. To efficiently extract signal, the background needs to be reduced by using topological selections. Therefore, the signal extraction from the invariant mass spectrum of the reconstructed Ξ baryons is investigated depending on the topological selection criteria and the choice of the fit-function.

The invariant mass distribution of the reconstructed cascade candidates is shown in figure 5. Once with only the preselection criteria from table 9 applied and once with three topological cuts applied in addition to the initial preselection criteria. These additional cuts, given in table 3, are applied on the distance of closest approach (DCA) in 3d between the cascade and V0 daughters respectively, and on the cosine of the pointing angle (PA) of the cascade candidate to the PV. The pointing angle of a particle to the PV is defined as the angle between the line connecting the primary vertex with its decay vertex and the momentum vector of the particle.

Cut	Description
DCAV0Dau <= 0.1 cm	Distance of closest approach between V0 daughters
DCACascDau <= 0.3 cm	Distance of closest approach between Cascade daughters
cos(PACascToPV) >= 0.995	Cosine of pointing angle of Cascade pointing back to the PV

Table 3: Analysis selection criteria for signal extraction

Since the Ξ baryon is abundantly produced in pp collisions, a signal peak structure can be observed at the mass of the Ξ even in the case where only preselection criteria are applied to the reconstructed cascade candidates. In both cases, the combinatorial background in the reconstruction of the Ξ baryon, which is homogeneously distributed across the displayed mass range, is small compared to the amount of reconstructed signal and even uniformly reduced in the case of the applied analysis selection criteria. To further quantify the effect of the analysis selection criteria on background reduction and signal extraction, two different signal fit-functions are compared regarding their performance in describing the invariant mass distribution.

Figure 6 shows a comparison between the DSCB function (green), as described in equation 14, and the Voigt profile (red), as described in equation 13, as a signal fit-function for fitting the invariant mass distribution of reconstructed cascade candidates with only the preselection criteria applied. On the upper panel of figure 6 the fitted invariant mass distribution is plotted, whereas on the lower panel of figure 6 the ratio of the invariant mass distribution and the total fit-functions is shown. The invariant mass distribution was fitted simultaneously modelling the background shape with a quadratic polynomial, given in equation 15, and the signal with the discussed signal fit-functions respectively.

$$\text{Total-Fit}(x; ..., p_0, p_1, p_2) = \begin{cases} \text{DSCB}(x; N, \mu, \sigma, n_1, n_2, \alpha_1, \alpha_2) & + p_2x^2 + p_1x + p_0 \\ \text{V}(x; A, \mu, \sigma, x_0, \gamma) & + p_2x^2 + p_1x + p_0 \end{cases} \tag{15}$$

The total fit-function is indicated with the solid lines while the quadratic polynomial background fit is indicated with the dashed lines in figure 6. In addition, the corresponding χ^2_{red} values are reported as an overall measure of the fit quality as well as the values of the fitted means and widths of the signal part of the distribution.
The Voigt profile is not able to describe the asymmetries of the distribution, especially in the region of the tails. It underestimates the tail structure on the left side of the Ξ baryon mass peak and overestimates it on the right side of the mass of the Ξ baryon, which can be seen in the ratio plot. Furthermore, the Voigt profile is not able to perfectly describe the shape of the signal peak in the region of its maximum and tends to underestimate the signal height, which results in deviations from 1 in the mass region of the Ξ baryon in the ratio plot. Both shortcomings of the Voigt-fit are also reflected by the large deviation of χ^2_{red}-Voigt = 6.74 from 1.
The DSCB function, however, better describes the asymmetries of the distribution and accurately estimates the tails on both sides. Similar to the Voigt, the DSCB is not able to describe the shape of the signal peak at the region of its maximum but the deviations from the data are smaller as seen in the ratio plot. This result is also confirmed by the smaller deviation of χ^2_{red}-DSCB = 2.66 from 1. Thus, the DSCB function provides a better description of the invariant mass distribution and is therefore used for signal extraction. In general, for extracting the particle yield for a physics analysis a more precise description of the distribution is needed. However to estimate the effect of the analysis selection criteria on background reduction, the precision of the DSCB is found to be sufficient.

To extract the number of signal candidates, the integrals below the fitted background function, which corresponds to the number of background candidates, as well as under the total fit are calculated and the signal counts are extracted as the difference between both:

$$s = \int_{\mu-3\sigma}^{\mu+3\sigma} \text{Total-Fit}(x; ..., p_0, p_1, p_2)\, dx \quad - \quad b, \quad \text{with} \quad b = \int_{\mu-3\sigma}^{\mu+3\sigma} p_2x^2 + p_1x + p_0\, dx \tag{16}$$

The signal region for this integration is defined as a 3σ interval around the extracted mean from the signal fit-function. This range is not sufficiently large to capture all signal candidates as the width of the DSCB is not fully described by the width of the Gaussian part alone. However, this interval is sufficient for comparing the effects of the different selections as the interval mainly is chosen consistently. Both, the mean μ_{DSCB} and sigma σ_{DSCB} from the Gaussian part of the DSCB-fit are reported in figure 6. The results with values of the number of signal candidates s, the number of background candidates b, the signal-to-background ratio s/b, and the signal purity $P = \frac{s}{s+b}$ within the 3σ signal region are reported in table 4.

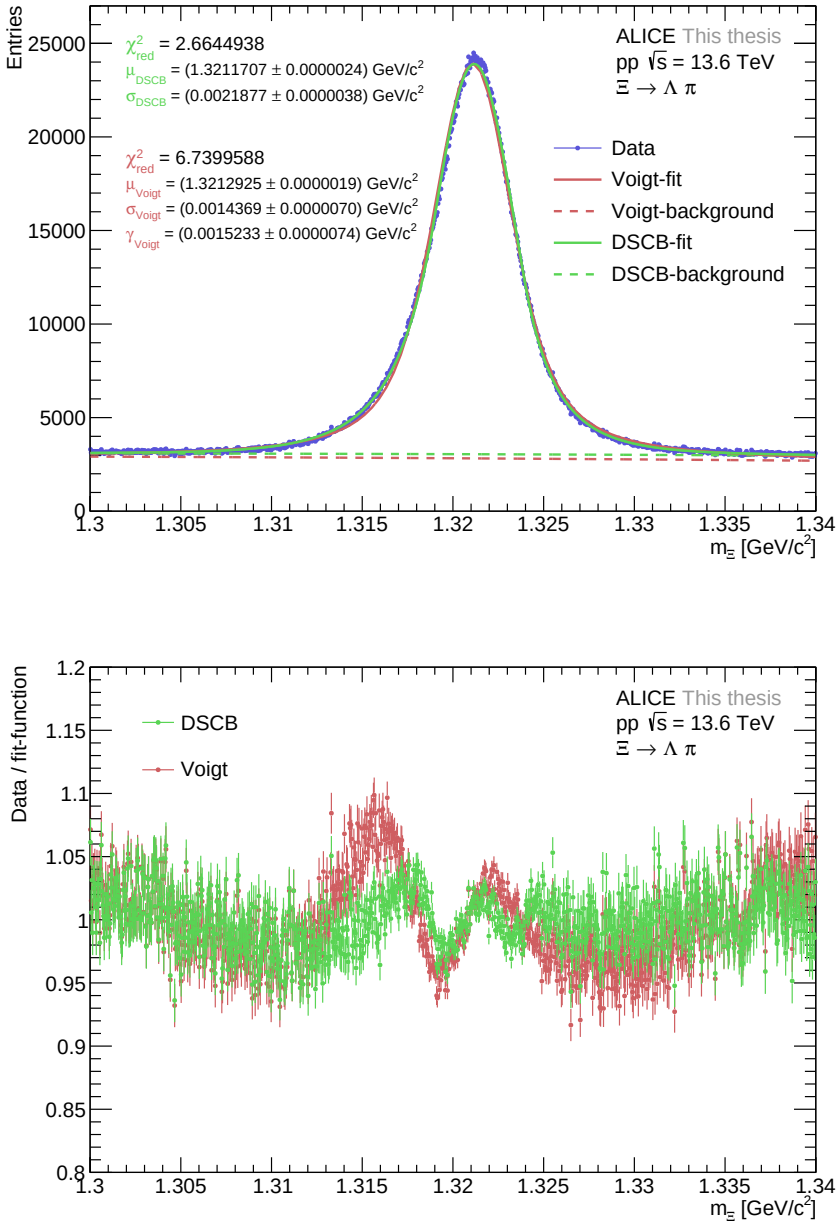

Figure 6: Comparison of different signal fit-functions, according to equation 13 (red) and 14 (green), for the invariant mass distribution of reconstructed cascade candidates with preselection criteria applied. Top: Invariant mass distribution with applied signal fit-functions (solid lines) and quadratic polynomial background fit (dashed lines). Bottom: Ratios between data and the total fit-functions.

quantity	description	value	uncertainty
s	signal candidates	3104738	8985
b	background candidates	998565	1115
s/b	signal-to-background ratio	3.109	0.010
P	signal purity $P = \frac{s}{s+b}$	0.757	0.004

Table 4: Signal extraction quantities from a DSCB-fit to the invariant mass distribution of the reconstructed cascade candidates distribution with preselection criteria applied.

As expected, the signal-to-background ratio reflects that the Ξ baryon is easily distinguished from the background because it is abundantly produced in pp collisions and the background is comparably low. In the defined 3σ signal region, the cascade candidates have a signal purity of about 76%. That means approximately 76% of these candidates are correctly reconstructed Ξ baryons given that the background below the signal peak is accurately modelled by the quadratic polynomial. With these restrictions, it is possible to compare "signal", defined as cascade candidates in the defined 3σ signal region, with background, defined as cascade candidates outside the Ξ mass window ($(m_{\Xi} - 1.32171\,\mathrm{GeV/c^2}) >= 0.015\,\mathrm{GeV/c^2}$), for different parameters. The chosen value of $0.015\,\mathrm{GeV/c^2}$ for background selection corresponds to cascade candidates outside a 6σ signal region and therefore ensures negligible amounts of Ξ baryons in the background sample. This allows to evaluate the performance of the different topological selections in the analysis selection criteria in table 3 and to demonstrate their ability to separate signal and background.

Figure 7 shows a "signal" vs. background comparison of the parameters used in the analysis selection criteria. For better visualisation, all distributions are plotted in logarithmic scale and the selections of the analysis selection criteria are indicated as dashed red lines with red arrows in the direction of rejection. In addition, the mean μ of each distribution is reported for a quantitative estimation of the difference between signal and background.
To validate this comparison, the distribution of MC signal is provided for the DCA between V0 daughters. The distribution matches well with the extracted signal distribution in data inside the accepted region. This confirms that the definition of "signal" in data is sufficient for the study of the different selections used in the analysis selection criteria. The used MC sample is discussed in detail in section 5.
The signal and background distributions are both normalised to their respective total number of entries. For the DCA between cascade daughters and the DCA between V0 daughters, the signal distributions tend to have smaller values of the DCAs compared to the background distributions which is also represented by the large deviations between the mean values of the signal and background distributions. The signal distribution of the pointing angle shows a stronger peak towards one compared to the background distribution. In all three cases, the mean of the signal distribution lies inside the accepted region and for all parameters except the DCA between cascade daughters the mean of the background distribution is in the rejected region. In summary, these observations demonstrate the parameters' ability to separate signal from background candidates.

To further quantify the effect of the analysis selection criteria in table 3 on background reduction and signal extraction, the invariant mass distribution shown in figure 5 with the additional analysis selection criteria applied is fitted with a DSCB function as a signal fit-function and a polynomial of second order as background fit. On the upper panel of figure 8, the fitted invariant mass distribution is plotted, whereas on the lower panel of figure 8 the ratio of the invariant mass distribution and the total fit-function is shown. As discussed in figure 6, the DSCB function provides a better description of the signal than the Voigt profile and is therefore used to extract signal from the invariant mass distribution according to equation 16 because ideally, only the background shape should change with additional selections. Both, the mean μ_{DSCB} and sigma σ_{DSCB} from the Gaussian part of the DSCB-fit are reported in figure 8. The results extracted within the defined 3σ region around the extracted mean of the signal fit to the invariant mass distribution are reported in table 5.

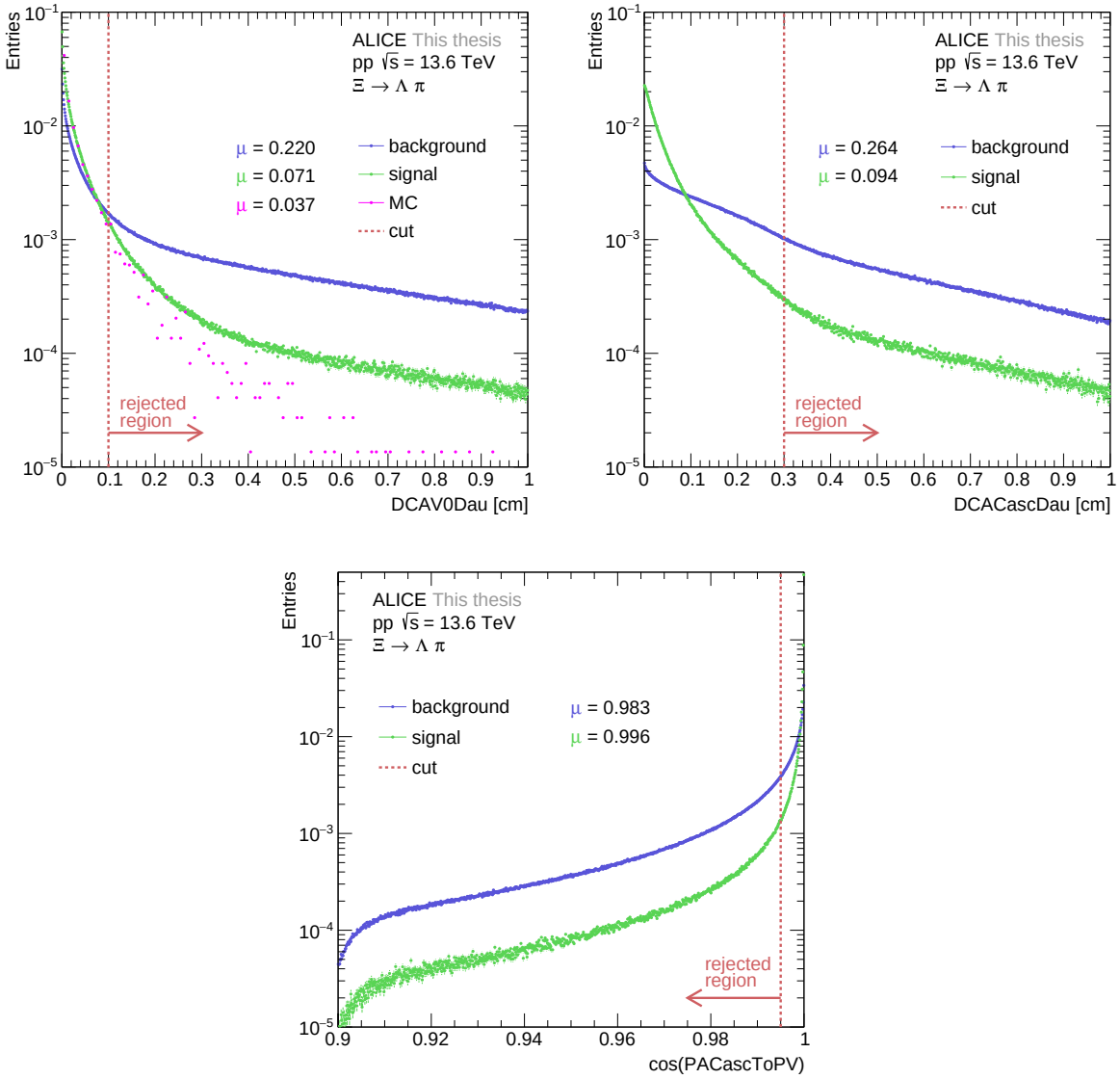

Figure 7: Comparison between "signal" (green markers), defined as cascade candidates in the defined 3σ signal region, and background (blue markers), defined as cascade candidates outside the Ξ mass window ($(m_{\Xi} - 1.32171\,\mathrm{GeV/c^2}) >= 0.015\,\mathrm{GeV/c^2}$), of the parameters used in the analysis selection criteria in table 3. Top Left: Distribution of the distance of closest approach between V0 daughters with additional MC signal distribution (pink markers). Top Right: Distribution of the distance of closest approach between cascade daughters. Bottom: Distribution of the cosine of the pointing angle of the cascade pointing back to the primary vertex.

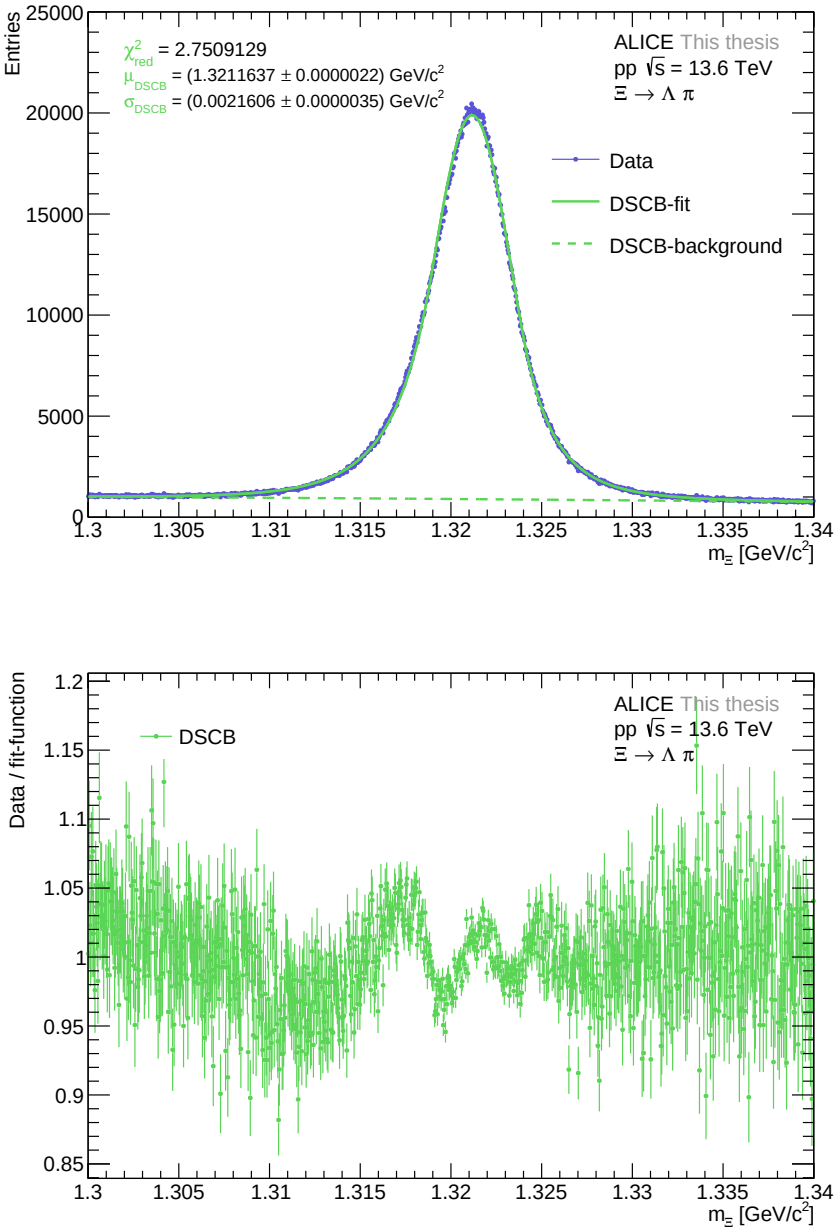

Figure 8: Comparison of different signal fit-functions, according to equation 13 (red) and 14 (green), for the invariant mass distribution of reconstructed cascade candidates with analysis selection criteria applied. Top: Invariant mass distribution with applied signal fit-functions (solid lines) and quadratic polynomial background fit (dashed lines). Bottom: Ratios between data and the total fit-functions.

quantity	description	value	uncertainty
s	signal candidates	2780230	8083
b	background candidates	289201	603
s/b	signal-to-background ratio	9.61	0.03
P	signal purity $P = \frac{s}{s+b}$	0.906	0.005

Table 5: Signal extraction quantities from a DSCB-fit to the invariant mass distribution of the reconstructed cascade candidates distribution with analysis selection criteria applied.

With the additional analysis selection criteria applied, the number of signal candidates decreases by about 10.5% while approximately 71% of background candidates are rejected compared to the numbers of signal and background candidates found in table 4. In addition, the value of the signal-to-background ratio increases from 3.1 to 9.6 and the signal purity increases from 76% to 91%. In summary, the three topological selections in the analysis selection criteria of table 3 are able to separate signal and background effectively. Therefore, the set of selections can serve as a reference and starting point for future physics analyses of Ξ and Ξ_c^+ baryons.

5 Performance studies in general purpose Monte-Carlo

In order to test the reconstruction performance of the two different reconstruction algorithms discussed in section 3.1, simulated Monte-Carlo (MC) data is used. Using the event generator PYTHIA8, primary collisions are simulated including the information of all emerging particles. The interaction with the detector material and the corresponding detector responses of all produced particles are simulated with the detector response simulation code GEANT4 according to the Run 3 ALICE detector setup described in section 2.1. The final data sample closely resembles the real recorded data and thus can be reconstructed and analysed in the same way.
For this part of the analysis, the used data sample consists of simulated pp collisions at the centre of mass energy $\sqrt{s} = 13.6$ TeV. The sample consists of about 761 million general purpose MC events with approximately 900 000 reconstructed cascade candidates. Here, general purpose means that no hadron species is preferentially generated in the simulated collision and the relative multiplicity of different hadron species closely resembles the one found in real collisions.

reconstruction case	propagation	vertex-fitting	material considerations
DCA	DCA fitter	DCA fitter	yes
KF + DCA	DCA fitter	KFParticle	yes
KF	KFParticle	KFParticle	no

Table 6: Reconstruction cases for general purpose Monte-Carlo performance studies.

All cascade candidates are reconstructed three times according to the reconstruction cases described in table 6 which allows for a direct comparison between the KFParticle package and the DCA fitter. The "DCA" and "KF" cases correspond to the different reconstruction algorithms described in section 3.1, which means that the propagation of the particles inside the detector as well as the vertex fitting is purely done with the DCA fitter and the KFParticle package respectively. Since the KFParticle package is designed to be independent of the detector geometry, it does not consider any material during the propagation of the daughter particles' parameters from their innermost measured point to the reconstructed vertex. The relevance of considering material during the propagation of the parameters of the daughter particles is explained in the following for the reconstruction of a decayed particle, such as the Λ baryon, whose decay is shown in figure 9.

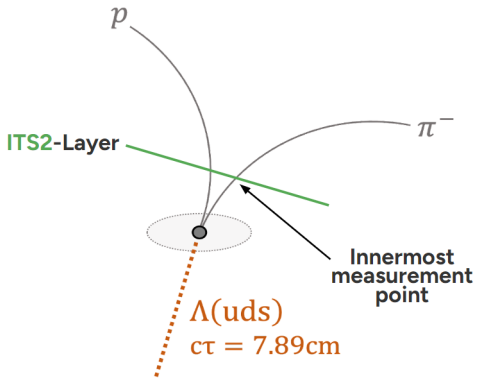

Figure 9: Sketch of the Λ-baryon decay with the innermost measurement point of the daughter tracks in one of the ITS2-layers.

In Run 3, the parameters of the measured tracks are stored at their innermost measurement point, often called *innermost update* (IU), inside the detector as discussed in section 2.2. Thus, for most of the tracks originating from a secondary vertex, it is expected that there is no detector material between the innermost update and the reconstructed vertex of the mother particle as depicted in figure 9. However, depending on the position of the reconstructed vertex relative to the detector layers, different amounts of air will be crossed by the daughter particles. This approximation is valid for mother particles like

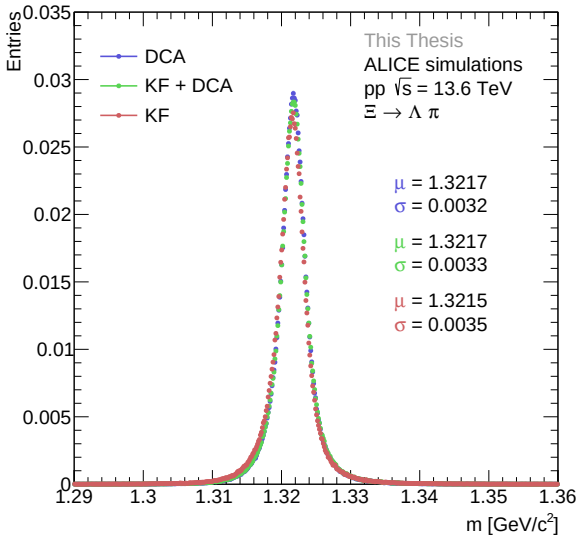

Figure 10: Invariant mass distribution of the reconstructed Ξ baryons for each reconstruction case listed in table 6. DCA case: (blue markers). KF+DCA case: (green markers). KF case: (red markers).

the Λ baryon which only decay into daughter particles with measured tracks. In the case of the Ξ baryon, which is reconstructed from the reconstructed Λ baryon itself and one additional measured π track, it is also possible to make the approximation that neglecting material might be a valid approach. The weakly decaying Λ baryon must be propagated from its measured decay point to its production point, namely the reconstructed decay vertex of the Ξ baryon. Due to its displaced decay topology, it is anticipated that it traverses several centimetres of air and may cross some detector layers. The Λ baryon has no electric charge and is therefore not affected by multiple scattering, as discussed in section 2.3, which is the main contribution when considering material.

In order to investigate the effect of material considerations, all cascade candidates are reconstructed a third time corresponding to the "KF+DCA" case. In this case, the propagation of the daughter tracks to a preliminary reconstructed decay vertex is done with the algorithm implemented in the DCA fitter to account for material. Subsequently, the vertex fit and the reconstruction of the mother particle are performed with the KFParticle package. Generally, considering material means correctly estimating the multiple scattering the particle undergoes in the material it traverses during the propagation by updating the covariance matrix of the track properly.

All reconstructed cascade candidates are preselected based on the topological selection criteria listed in table 9 and in addition, a mass constraint to the Λ mass is applied on the V0 candidates in the decay chain. In summary, the same conditions and selections are applied to the MC sample as to the real data analysed in section 4.

To compare the different reconstruction algorithms, only true signal Ξ baryons are analysed. Since the aim is to reach the best reconstruction performance for signal candidates, the crucial first step is to understand the reconstruction behaviour of true Ξ baryons in the analysed MC sample. Thus for this following part of the analysis, every cascade candidate is a true Ξ baryon decaying into a true Λ baryon and all daughter tracks are matched to the according daughters of the mother particle.

The analysis of the three cases listed in table 6 is performed for two different MC samples which differ in the available reconstruction because, during the time of the analysis, it was updated and improved. The following results focus on the older production as more statistics are available. Further differences between the productions and results from the newer production with the upgraded reconstruction are discussed in section 5.4.

The performance of the different reconstruction cases is compared regarding the secondary vertex, transverse momentum, and invariant mass resolutions of the Ξ baryon and its daughters.

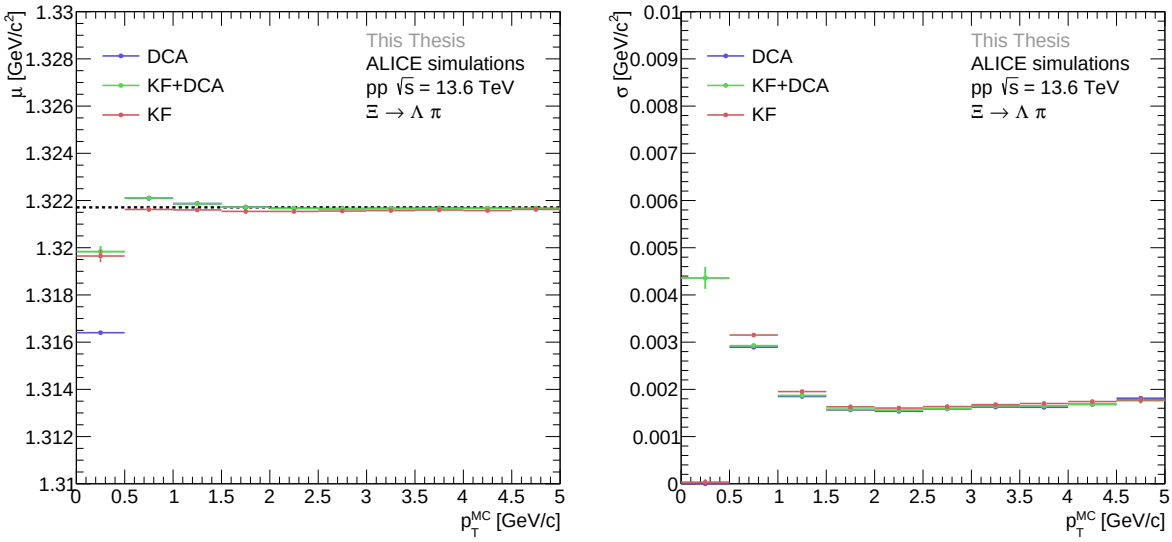

Figure 11: Extracted mean μ and standard deviation σ from a DSCB fit to the invariant mass distribution of the reconstructed Ξ baryons for each reconstruction case listed in table 6 as a function of transverse momentum p_{T}. Left: μ against p_{T}. Right: σ against p_{T}. DCA case: (blue markers). KF+DCA case: (green markers). KF case: (red markers).

5.1 Invariant mass resolution of reconstructed Ξ baryons

The invariant mass distributions of the reconstructed Ξ baryons corresponding to the different reconstruction cases are shown in figure 10. To improve consistency and visibility, the three different cases are plotted in figure 10 according to their corresponding colour in table 6 and will be plotted with this colour scheme in the following part of the analysis. In addition, the values of the mean μ and the standard deviation σ of the distributions for each reconstruction case are reported.
As only true Ξ baryons are analysed, no background is visible under the signal peak around the mass of the Ξ baryon.
Comparing the distributions of each reconstruction case and in particular the reported values of μ and σ, the invariant mass of the Ξ baryons is reconstructed with similar resolution in all three cases. To further investigate the reconstruction performance, the invariant mass of the Ξ baryons is analysed for different transverse momentum intervals and fitted with a DSCB according to equation 14 to model the signal shape.

Figure 11 presents extracted values of the mean μ and the standard deviation σ from the Gaussian part of the DSCB fit to the invariant mass distribution of the reconstructed Ξ baryons for each reconstruction case in table 6 as a function of their transverse momentum p_{T} up to 5 GeV/c. On the left panel, the extracted μ against p_{T} is plotted and in addition, the PDG value of the Ξ baryon mass from table 2 is indicated with the dashed black line. The extracted σ against p_{T} is shown on the right panel.
As discussed in section 4, the DSCB function provides a good description of the signal shape of reconstructed Ξ baryons and is therefore used to describe the mean and the width of the invariant mass distribution for each p_{T} interval. The width of the fitted DSCB to the invariant mass distribution is not fully described by the width of the Gaussian part alone. However, to compare the performance of the different reconstruction cases, this estimation for the width of the distributions is sufficient. The first p_{T} interval from 0 to 0.5 GeV/c should be taken out of consideration as there are too few reconstructed Ξ baryons with corresponding p_{T} to produce a reasonable fit as shown in figure 30 in the appendix.
The extracted mean values are very similar for each reconstruction case, especially the "KF+DCA" and the "DCA" cases are visually nearly identical. The values for the "KF" case deviate only up to 0.05 % from the values of the other reconstruction cases for each p_{T} interval. Still, the values of all

cases are compatible with the PDG mass value of the Ξ baryon and are in remarkable agreement for high p_{T}.
Similarly, the extracted width values are comparable for each reconstruction case, in particular going to high p_{T}. In the "KF" case the values of the width lie only up to 10 % above the other reconstruction cases, especially for low p_{T} and thus indicate are slightly worse invariant mass resolution in the case of the pure KFParticle package compared to the "KF+DCA" and the "DCA" case. However, the available statistic is not sufficient to permit a strong and final statement.
In general, the invariant mass resolution of a particle reconstructed with ALICE depends primarily on the momentum resolution of its measured daughter particles. The transverse momentum resolution of the reconstructed Ξ baryons and its daughters is investigated and explained in section 5.3.
In summary, all three reconstruction cases reconstruct the invariant mass of the Ξ baryons with very similar precision across the investigated p_{T} range.

5.2 Position resolution measurements

5.2.1 Secondary vertex resolution of reconstructed Ξ baryons

Figure 12 presents the residual distributions of the secondary vertex position of the reconstructed Ξ baryons in all three spatial directions according to the global coordinate system described in section 2.1. The three different reconstruction cases are plotted according to their corresponding colour in table 6 and in addition, the values of the mean μ and the standard deviation σ of the distributions for each reconstruction case are reported.
As described in section 3.2, investigating the residual distribution allows to quantify the deviations between the generated and reconstructed value of a parameter. All three spatial directions show a residual distribution for all three analysed cases which is symmetric and centred around 0, thus no bias is observed for the reconstruction of the secondary vertex position. As previously observed for the invariant mass, the distributions for each case are compatible which is further confirmed by the comparable reported values of μ and σ. Therefore, the secondary vertex position of the Ξ baryons is reconstructed with a very similar resolution in all investigated cases.
Comparing the distributions in the x- and y-direction with the one in the z-direction, the distributions' width (σ) and general shape are very similar. As discussed in section 2.1.1, the upgraded ITS2 provides a similar resolution in all three spatial directions.

To further compare the reconstruction performance of the secondary vertex between the three cases, the secondary vertex pull distributions of the reconstructed Ξ baryons are investigated. The pull distribution of a parameter allows to measure how the uncertainties are estimated for the investigated parameter, as discussed in section 3.2, by extracting the width of the distribution with a multi-Gaussian fit according to equation 10. This analysis is performed for different transverse momentum intervals of the Ξ baryons.
As an example, figure 13 shows the secondary vertex pull distribution in x-direction of the reconstructed Ξ-baryons with transverse momentum $1.6 < p_{\mathrm{T}} < 1.8$ GeV/c for each reconstruction case listed in table 6. On the upper panel, the three distributions are separately fitted with triple Gaussian functions according to equation 10 with $n = 3$. In addition, the corresponding reduced χ^2_{red} values are reported as an overall measure of the fit quality as well as the values of the weighted means μ_w and weighted standard deviations σ_w extracted from the fit according to equation 11. On the lower panel of figure 13 the ratio of the distribution and their corresponding fit-function is shown.
It is clearly visible that the three presented distributions deviate from each other, which is quantified by the reported values of σ_w. The blue distribution, corresponding to the "DCA" case, is the broadest distribution with $\sigma_w = 2.12$ which is larger than the expected value of $\sigma_w = 1$. This is, therefore, an indication that the uncertainties are underestimated during the reconstruction of the secondary vertex performed with only the DCA fitter. As mentioned in section 2.2, the DCA fitter is neglecting correlations between spatial and momentum parameters and therefore might not be able to correctly estimate the uncertainties of the reconstructed secondary vertex which is supported by the presented result. On the other hand, the green distribution, corresponding to the mixed "KF+DCA" case, is the narrowest distribution with $\sigma_w = 0.77$ which is smaller than $\sigma_w = 1$, and thus the uncertainties might be overestimated during the reconstruction of the secondary vertex. Finally, the red distribution,

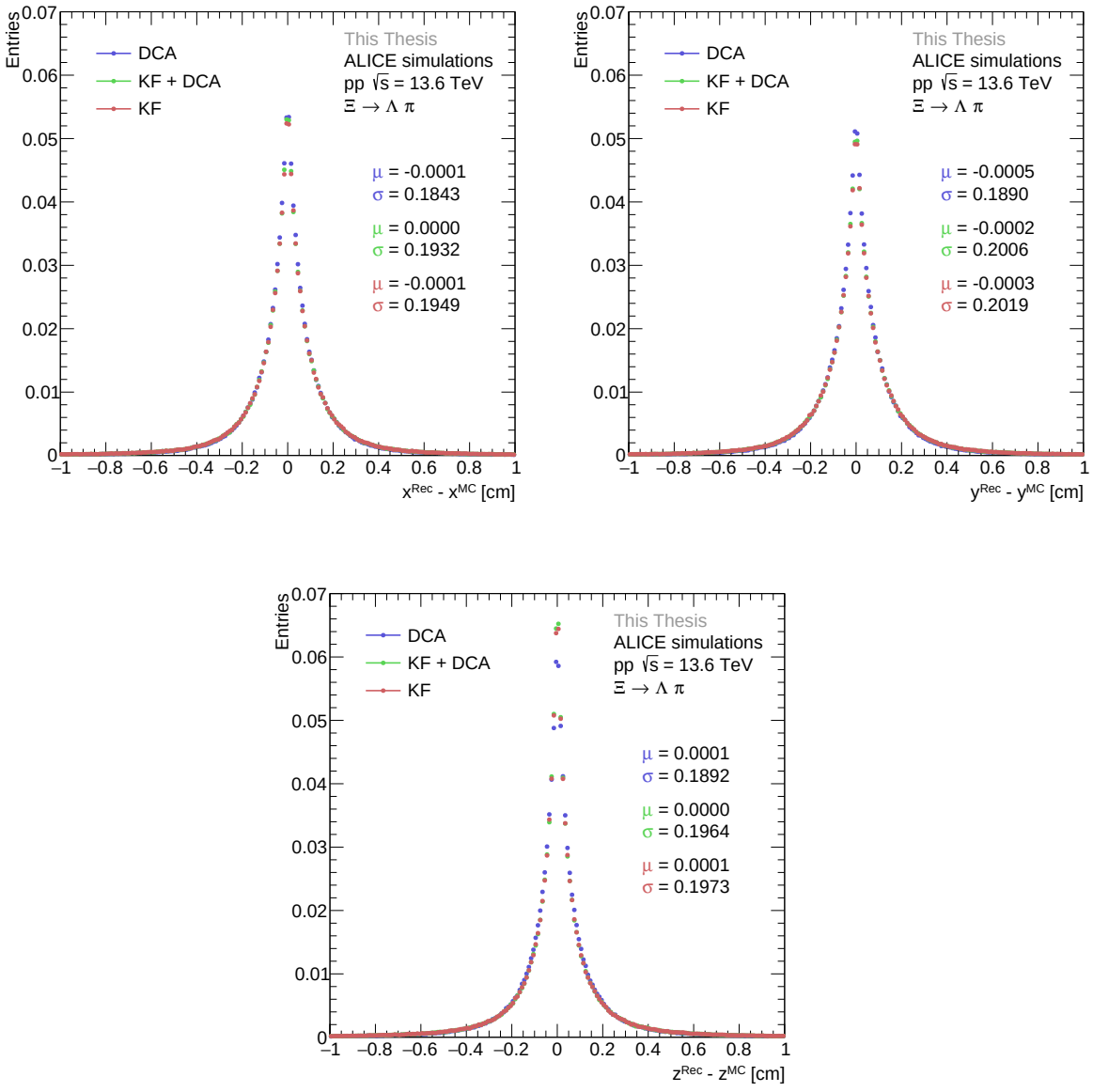

Figure 12: Secondary vertex residual distributions of reconstructed Ξ baryons for each reconstruction case listed in table 6 according to the coordinate system described in section 2.1. Top Left: SV residual distribution in x-direction. Top Right: SV residual distribution in y-direction. Bottom: SV residual distribution in z-direction. DCA case: (blue markers). KF+DCA case: (green markers). KF case: (red markers).

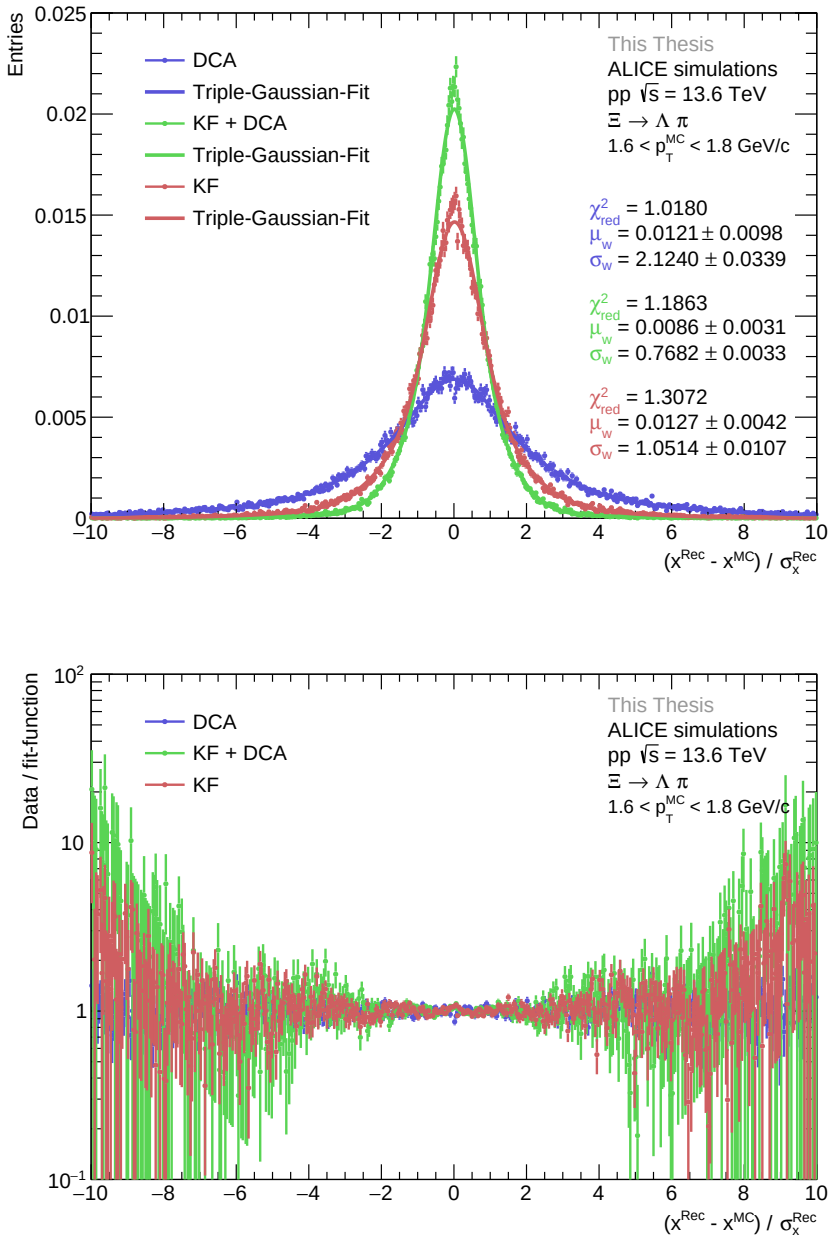

Figure 13: Fits of a triple Gaussian according to equation 10 with $n = 3$ to the secondary vertex pull distribution in x-direction of the reconstructed Ξ baryons for each reconstruction case listed in table 6 with transverse momentum $1.6 < p_{\mathrm{T}} < 1.8$ GeV/c. Top: SV pull distributions with fitted triple Gaussians (solid lines). Bottom: Ratios between data and the fit-functions. DCA case: (blue markers). KF+DCA case: (green markers). KF case: (red markers).

corresponding to the "KF" case, has a value of $\sigma_w = 1.05$ which is closest to $\sigma_w = 1$. Therefore, the secondary vertex uncertainties in the investigated p_{T} interval are most accurately estimated for the case in which only the KFParticle package is used for the vertex reconstruction.
Similar results are found for the y- and z-direction shown in figure 31 and 32 in the appendix. In general, the secondary vertex pull distributions of the reconstructed Ξ baryons in y-direction are very similar to the distributions in x-direction which are reflected by the very similar values of σ_w of each reconstruction case, respectively. The pull distributions in z-direction are broader for each reconstruction case, respectively, compared to the distributions in x- and y-direction which is reflected by the larger values of σ_w.

Figure 14 shows the weighted standard deviations σ_w obtained from triple Gaussian fits to the secondary vertex pull distributions of the Ξ baryons for each reconstruction case in all three spatial directions as a function of their p_{T} up to 5 GeV/c. In addition, $\sigma_w = 1$ is indicated with a black dashed line. Values of $\sigma_w > 1$ correspond to an underestimation of the reconstructed SV uncertainties while values of $\sigma_w < 1$ correspond to an overestimation of the SV uncertainties.
For each investigated case, a similar p_{T} dependence is observed for each spatial direction. As described before, the distributions of σ_w for the pulls in x- and y-direction are very similar while the distributions of σ_w for the pulls in z-direction are shifted towards larger values of σ_w.
In all three spatial directions, the blue distribution of σ_w corresponding to the "DCA" case shows values of $\sigma_w > 1$ over the whole p_{T} range with increasing values going to higher p_{T}. This indicates that the vertex reconstruction with the DCA fitter underestimates the SV uncertainties in all analysed p_{T} intervals with stronger underestimation at high p_{T}. The green and red distributions on the other hand, corresponding to the "KF+DCA" and "KF" case, respectively, show slightly decreasing values of σ_w going to higher p_{T}. This means that in the case of the pure KF Particle package and the mixed "KF+DCA" case, the uncertainties of the reconstructed secondary vertex are somewhat overestimated going to higher p_{T}.
In general, the values of σ_w of the "KF" and the "KF+DCA" case are closer to $\sigma_w = 1$ across the investigated transverse momentum range and especially at low p_{T} compared to the "DCA" case for which σ_w deviates strongly towards larger values. This further indicates that the DCA fitter is not able to correctly estimate the uncertainties of the reconstructed secondary vertex, especially at high p_{T}.
For reconstructed Ξ baryons with high p_{T}, the "KF" and the "KF+DCA" case approach each other to similar values of σ_w, which is expected as considering material in the propagation step, discussed in section 5, has a smaller impact on the position resolution of Ξ baryon daughters with high p_{T}. The material considerations are mainly due to multiple scattering inside the detector material where the root mean square of the scattering angle scales inversely with p as discussed in section 2.3. In the case of negligible or no multiple scattering in the material, the "KF" and the "KF+DCA" case should be the same which is further investigated in section 5.2.2.

5.2.2 Secondary vertex resolution of reconstructed Λ baryons in the cascade decay

Sample selection to study dependence on daughter track propagation As previously discussed, the Ξ baryons investigated in section 5.2.1 are reconstructed by combining a measured pion and a Λ baryon, which itself must be reconstructed from measured protons and pions. The Λ baryon has no electric charge and is therefore not directly measurable by the detector which introduces significant uncertainty into the reconstructed decay vertex position of the Ξ baryon. In order to disentangle the effects of the propagation of particles and the vertex fit on the secondary vertex reconstruction, the Λ baryons involved in the reconstructed cascade decay are investigated since both of its daughters are directly measured by the detector.
For the reconstruction of the Λ decay vertex, the daughter particle parameters have to be propagated from their innermost measurement point to the decay vertex position of the Λ baryon as explained in figure 9. In order to disentangle the effects of the vertex fit itself and the daughter particle parameter propagation through material, Λ baryons with different decay radii and radial positions of their corresponding daughter tracks are selected. As previously discussed in section 5.2.1, the material considerations during the propagation of the particles‘ parameters are mainly due to multiple scattering, discussed in section 2.3, and of course depend on the amount of material between the innermost measurement point and decay vertex position of the Λ baryon. Consequently, investigating Λ baryons

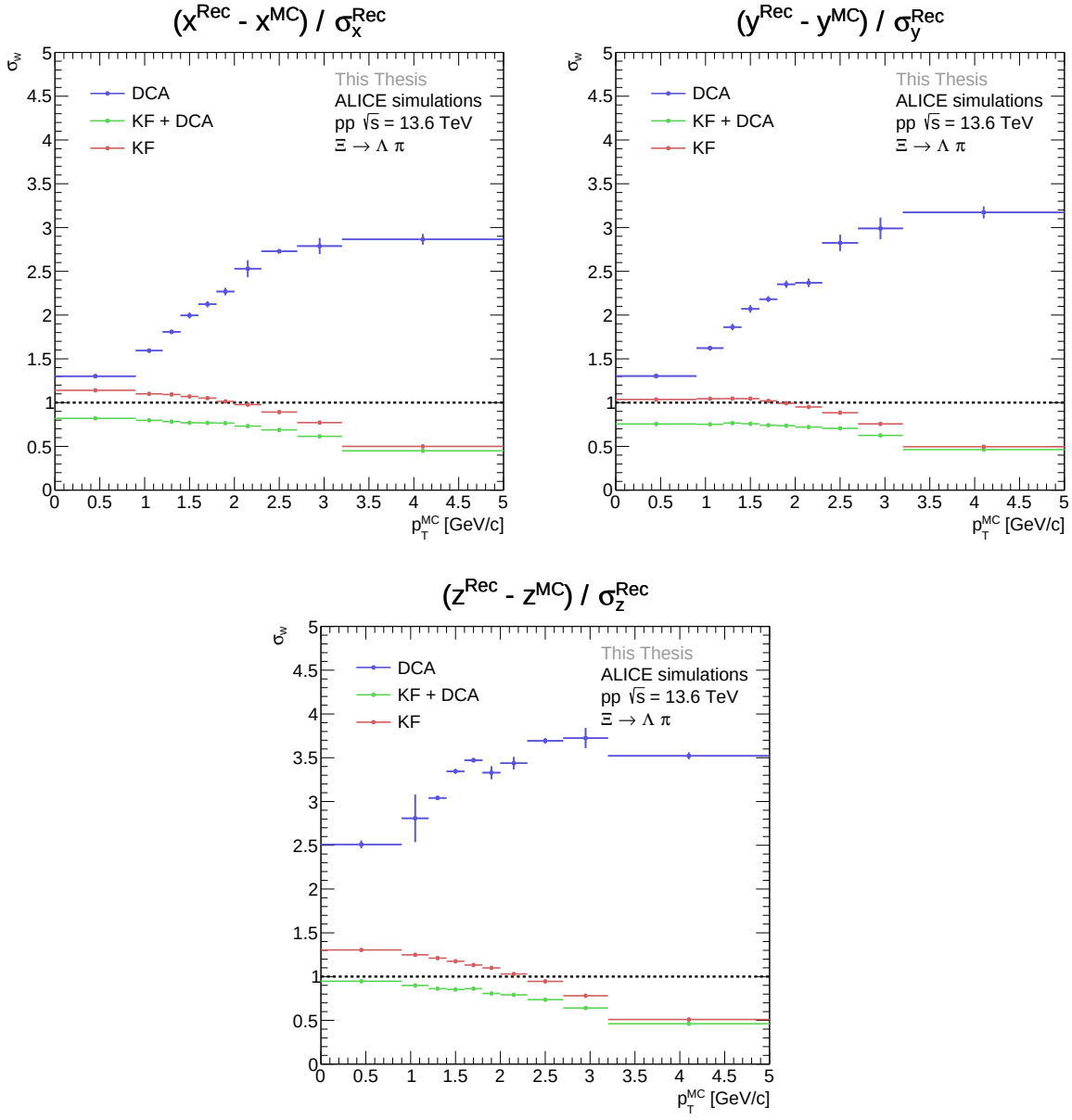

Figure 14: Weighted standard deviations σ_w of secondary vertex pull distributions of reconstructed Ξ baryons for each reconstruction case listed in table 6 obtained from triple Gaussian fits as a function of p_{T}. Top Left: σ_w-values from SV pull distribution in x-direction. Top Right: σ_w-values from SV pull distribution in y-direction. Bottom: σ_w-values from SV pull distribution in z-direction. DCA case: (blue markers). KF+DCA case: (green markers). KF case: (red markers).

enables a comparison of the three different reconstruction cases outlined in table 6 with regard to their performance in reconstructing the secondary vertex for varying amounts of material traversed by the daughter particles during the propagation step.

Figure 15 shows the radial position of the Λ baryon daughters at their respective innermost measurement points inside the ITS2. The average ITS2 layer positions from table 1 are indicated with dashed pink lines. The numbering of the ITS2 layers starts at zero as described in table 1. Therefore, layer no. 2 is the last layer of the inner barrel module of the ITS2 and layer no. 3 is the first layer of the outer barrel module of the ITS2.
In the investigated MC sample, all secondary vertices were reconstructed from ITS2-TPC matched tracks as described in section 2.2. Thus the protons and pions shown in the upper panel of figure 15 are all daughter particles of every reconstructed Λ baryon in the analysed sample as each track must be measured in the ITS2. In addition, a track needs to have hits in at least two different ITS2 layers to be reconstructed inside the ITS2. Therefore, no proton or pion has its innermost measurement point at the last ITS2 layer.
The majority of the daughter particles have their innermost measurement point at one of the layers of the outer barrel module of the ITS2 as seen in the upper panel of figure 15. Comparing the decay lengths of the Ξ ($c\tau$ = 4.9 cm) and Λ baryons ($c\tau$ = 7.9 cm) to the radial positions of the 3 inner barrel module layers of the ITS2, it becomes clear that most of the Λ baryons decay after the third ITS2 layer. In addition, it has to be kept in mind that the Ξ and Λ baryons reconstructed in the investigated sample are required to decay at a radial position larger than 1 cm as listed in table 9.
On the lower panels of figure 15, the radial position distribution of the Λ baryon daughters at the 3 layers of the inner barrel module (left panel) and at the first layer of the outer barrel module (right panel) of the ITS2 are shown in detail. In the case of the fourth ITS2 layer, two distributions are observed because the structure of all outer barrel modules is different from the inner barrel modules. The ITS2 layers are divided into azimuthally segmented units, designated as *Staves*. The degree and structure of the overlap between these Staves determine the potential radial positions of the innermost measurement points of particles [10].

In order to study the effect of the daughter parameter propagation through different amounts of air or detector material on the secondary vertex resolution, six Λ baryon samples are selected corresponding to different decay positions with respect to the detector material and varying daughter track measurement points. The different investigation cases are listed in table 7 together with their corresponding topological selections.

	both at layer no. 3	one at layer no. 3
$4.2 < r_\Lambda < 9.2$ cm	$\approx$ 12.5 cm air; no detector material	$>$ 12.5 cm air; $1-2$ ITS2 layer of material for one daughter
$9.2 < r_\Lambda < 14.2$ cm	$\approx$ 7.5 cm air; no detector material	$>$ 7.5 cm air; $1-2$ ITS2 layer of material for one daughter
$14.2 < r_\Lambda < 19.2$ cm	$\approx$ 2.5 cm air; no detector material	$>$ 2.5 cm air; $1-2$ ITS2 layer of material for one daughter

Table 7: Investigation cases with different radial positions of the Λ decay vertex r_Λ and innermost measurement points of daughter tracks to study the effect of varying amounts of material in the propagation of the Λ baryon daughters.

The case of both Λ baryon daughters having their respective IU positions at layer no. 3 of the ITS2 corresponds to propagating both daughter track parameters only through air to reconstruct the Λ decay vertex. The amount of air in this case is determined by the Λ baryon decay radius r_Λ. As described in table 7, r_Λ in the range 4.2 - 9.2 cm corresponds to an average of about 12.5 cm of air, r_Λ between 9.2 - 14.2 cm corresponds to an average of about 7.5 cm of air, and r_Λ within the interval 14.2 - 19.2 corresponds to an average of only about 2.5 cm of air.
Furthermore, in addition to the varying amounts of air, one or more detector layers are considered in the material budget between the daughter tracks' IU and their production point. For that purpose, Λ baryon candidates are selected which decay between layer no. 2 and layer no. 3 of the ITS2 and for

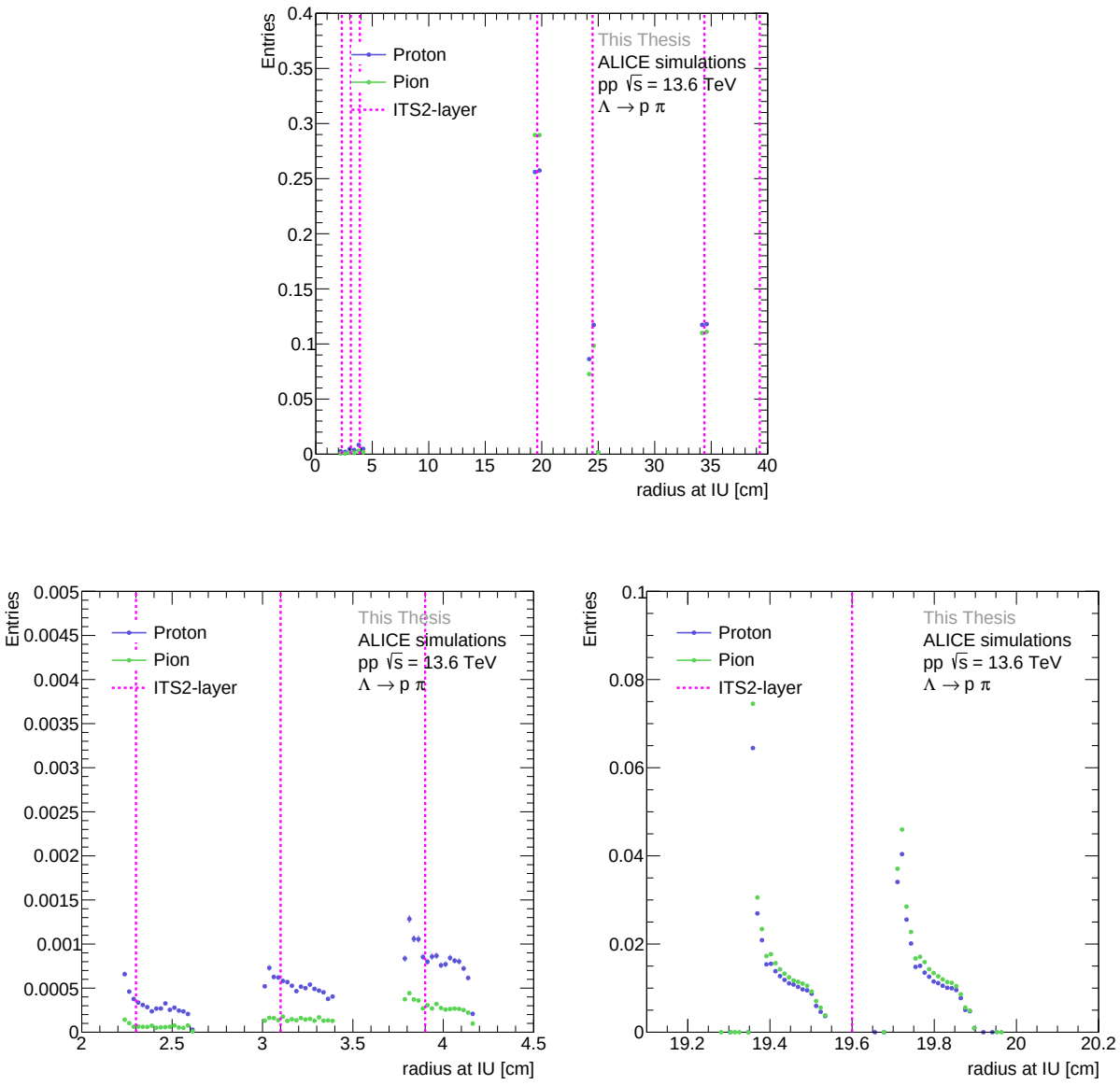

Figure 15: Radial position distribution of daughter particles of reconstructed Λ baryons at their respective innermost measurement point inside the ITS2 with ITS-layer positions (pink dashed lines) from table 1. Top: IU positions from 0 to 40 cm. Bottom Left: IU positions from 2 to 4.5 cm (layer no. 0-2). Bottom Right: IU positions from 19.1 to 20.2 cm (layer no. 3). Proton: (blue markers). Pion: (green markers).

which one of the daughter tracks is not measured at layer no. 3. In those cases, one of the daughter track parameters must be propagated through one or more ITS2 layers in addition to air in order to reconstruct the Λ baryon decay vertex. It is important to note that in instances where the daughter track IU position is lying further out than the ITS2 layer no. 3, additional air between the layers is added to the considered material budget on top of the detector material to account for the additional space between the layers.
Quantitatively, the case of "both at layer no. 3" corresponds to about 85 % of all Λ baryons and the case of "one at layer no. 3" corresponds to about 14 % of all Λ baryons of which about 80 % of the times, the other daughter particle is measured at layer no. 4. Furthermore, the cases in which the Lambda baryon decays between layer no. 2 and layer no. 3 of the ITS2 but both daughter tracks are not measured at layer no. 3 was also investigated. However, those cases correspond to less than 1 % of all Λ baryons, thus the statistics are too low to be analysed in this section and therefore this case will not be considered further.

As in section 5.2.1, the residual and pull distributions of the secondary vertex of the reconstructed Λ baryons are investigated for the six material cases of table 7 to investigate the effect of different amounts of material in the daughter parameter propagation. The analysis is performed for different transverse momentum intervals of the reconstructed Λ baryons. The results of investigating the Λ decay vertex position residuals (pulls) are presented in figure 16 (18) for the case of both Λ baryon daughters having their respective IU positions at layer no. 3 of the ITS2 and in figure 17 (19) for the case of only one Λ baryon daughter having its respective IU position at layer no. 3 of the ITS2.

Λ vertex position residuals Figure 16 presents the extracted standard deviations σ of the secondary vertex residual distributions in x-direction of reconstructed Λ baryons as a function of p_{T}. The three panels of figure 16 show Λ baryons with different decay radii corresponding to the three cases listed in the first column of table 7. In all three cases, the daughter track parameters were only propagated through air for the reconstruction of the Λ decay vertex.
The values of σ are compatible between the different reconstruction cases ("KF", "KF+DCA", "DCA") within the statistical uncertainties across the investigated p_{T} range for all three decay radii intervals of the Λ baryon. Therefore, the secondary vertex of the Λ baryon is reconstructed with a similar resolution in all reconstruction cases. In the "KF" case, no material is considered during the propagation of particles, in contrast to the "KF+DCA" and "DCA" cases, as explained in section 5. Thus, considering material for the different amounts of air corresponding to the different Λ baryon decay radii intervals in the propagation step of the daughter particles does not seem to influence the secondary vertex resolution of the reconstructed Λ baryons as all three reconstruction cases produce similar values of σ.
In general, the secondary vertex resolution improves as the Λ baryon decay radius is closer to the radial position of the ITS2 layer no. 3, which is expected because of two different effects: The amount of air decreases as discussed before and the Λ decay vertex position lies closer to the innermost measurements of its associated daughter particles. As the material considerations for the air during the propagation step of the daughter particles do not influence the secondary vertex resolution of the reconstructed Λ baryons, the dominant effect for the increasing vertex resolution is the geometric effect discussed in section 2.4.2. The closer the daughter tracks' innermost measurement point is to the reconstructed decay vertex, the shorter the extrapolation length of the daughter particles' parameters to the secondary vertex and the better the vertex resolution.
For all three decay radii intervals, the values of σ decrease slightly across the investigated p_{T} range and therefore indicate a slightly better secondary vertex resolution for Λ baryons going to higher p_{T}. In general. the secondary vertex resolution of the Λ baryon strongly depends on the position resolution of its daughter tracks independently of the reconstruction case. Thus, a possible explanation for this result is that high momentum Λ baryon daughter tracks are less affected by multiple scattering as discussed in section 2.3.
Similar results are found for the secondary vertex residual distributions of the Λ baryon in the y- and z-direction presented in figure 33 and 35 in the appendix.

Similarly to "both at layer no. 3" cases discussed before, figure 17 shows the extracted width of the secondary vertex residual distribution in x-direction of reconstructed Λ baryons as a function of p_{T}

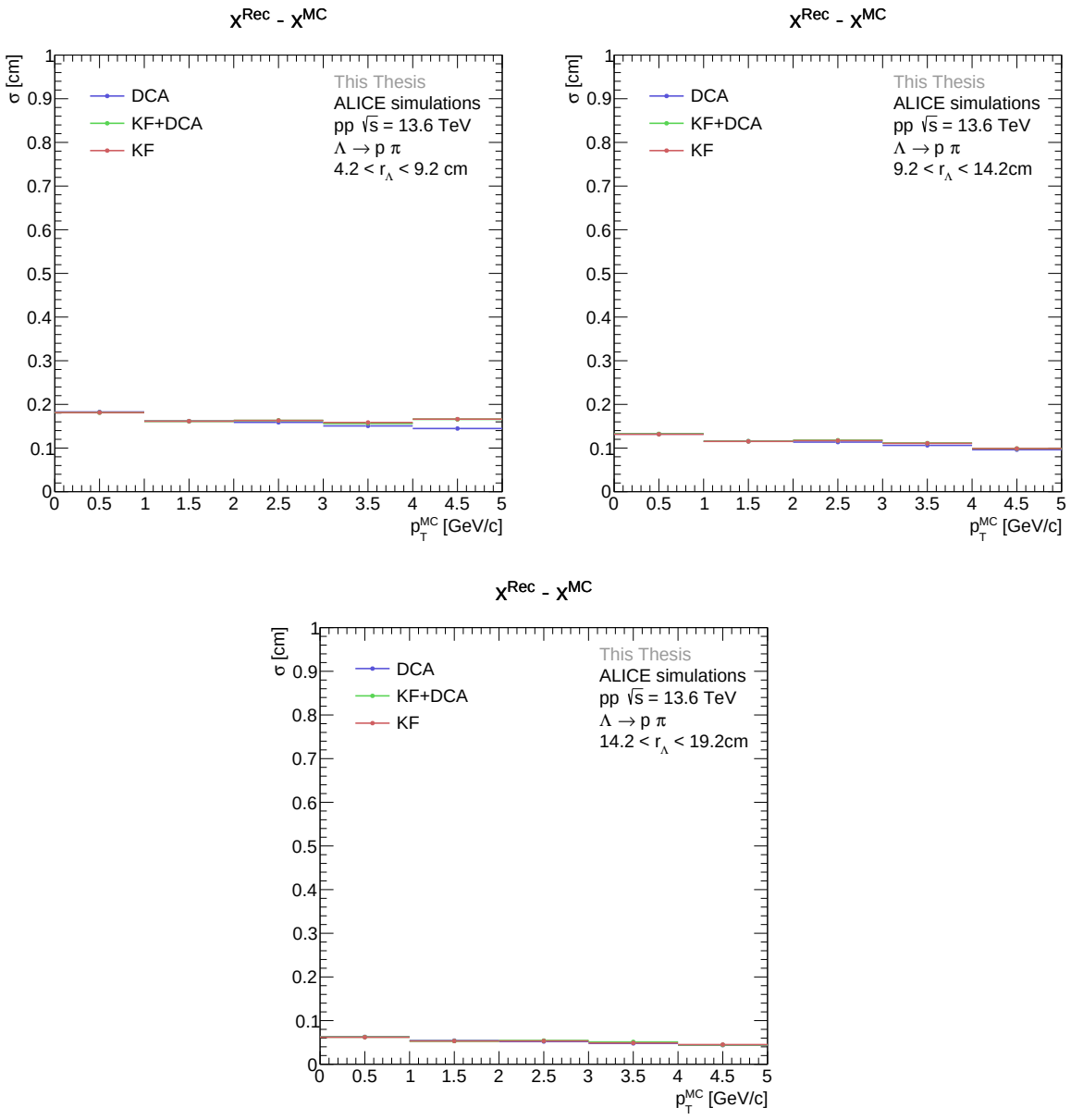

Figure 16: Extracted standard deviations σ of secondary vertex **residual distributions** in x-direction of reconstructed Λ baryons for each reconstruction case listed in table 6 as a function of p_{T} corresponding to the case **"both at layer no. 3"**. Top Left: σ against p_{T} for $4.2 < r_\Lambda < 9.2$ cm. Top Right: σ against p_{T} for $9.2 < r_\Lambda < 14.2$ cm. Bottom: σ against p_{T} for $14.2 < r_\Lambda < 19.2$ cm. DCA case: (blue markers). KF+DCA case: (green markers). KF case: (red markers).

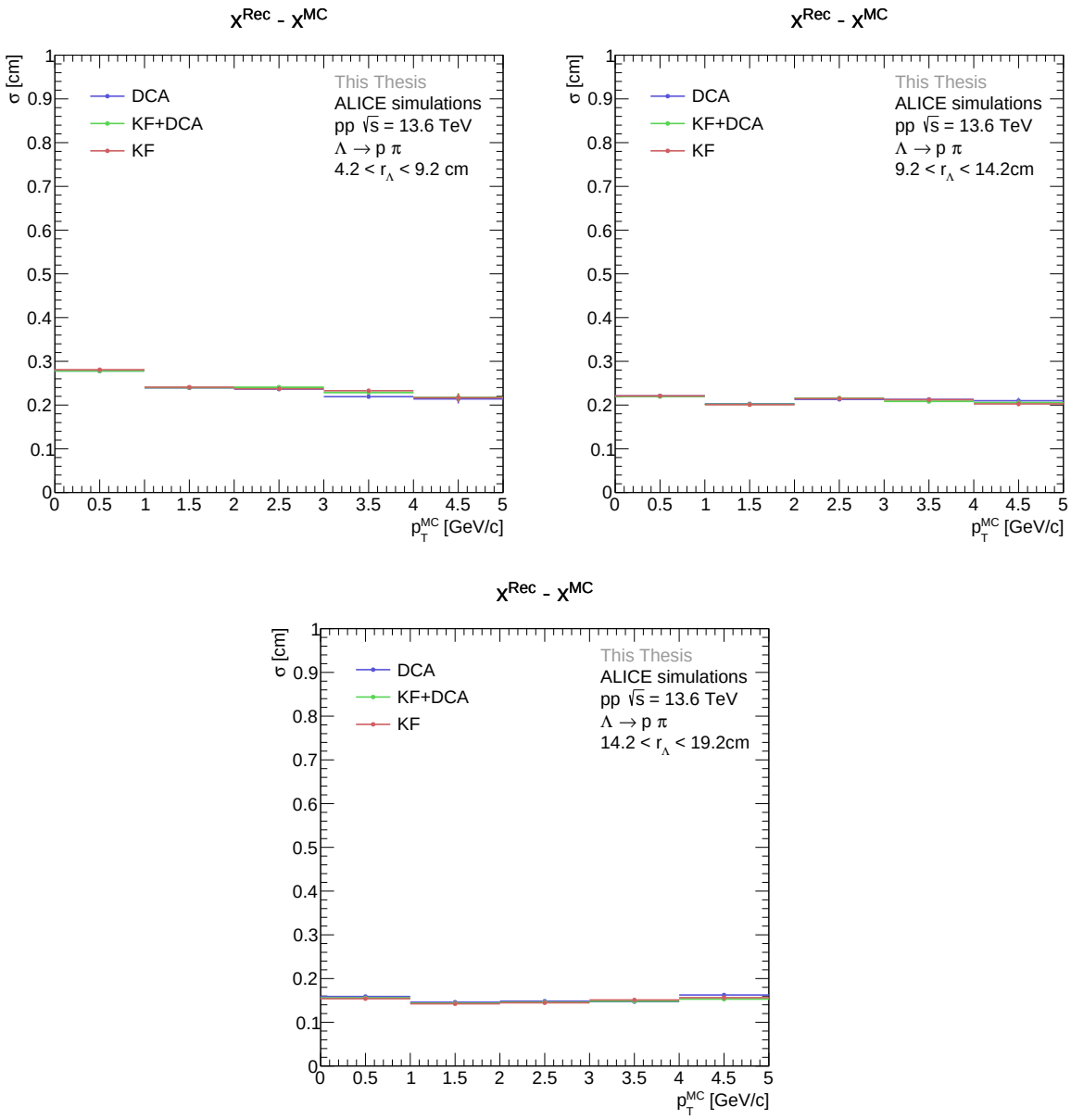

Figure 17: Extracted standard deviations σ of secondary vertex **residual distributions** in x-direction of reconstructed Λ baryons for each reconstruction case listed in table 6 as a function of p_{T} corresponding to the case **"one at layer no. 3"**. Top Left: σ against p_{T} for $4.2 < r_\Lambda < 9.2$ cm. Top Right: σ against p_{T} for $9.2 < r_\Lambda < 14.2$ cm. Bottom: σ against p_{T} for $14.2 < r_\Lambda < 19.2$ cm. DCA case: (blue markers). KF+DCA case: (green markers). KF case: (red markers).

corresponding to the case "one at layer no. 3".
As already observed before, the residual distributions presented in the three panels of figure 17 are compatible between the different reconstruction cases ("KF", "KF+DCA", "DCA"). This result further indicates that the vertex position resolution is independent of the material considered in the propagation step of the daughter particles with the code of the DCA fitter even if one of the Λ daughters is propagated through an ITS2 layer of material.
Compared to figure 16, the observed resolutions are larger in the different decay radii intervals. In the investigated p_{T} range, the multiple scattering of one Λ daughter track in at least one ITS2 layer is the dominant contribution to its position resolution. In addition, one of the Λ daughter particles has to be propagated a larger distance from its innermost measurement point at layer no. 4 or layer no. 5 to the reconstructed secondary vertex of the Λ baryon. Both effects contribute to the secondary vertex resolution of the Λ baryon in the analysed "one at layer no. 3". However, further investigation is necessary to discuss the behaviour of the single reconstruction case.
Similar results are found for the secondary vertex residual distributions of the Λ baryon in y- and z-direction in figure 37 and 39 in the appendix.

Λ vertex position pulls As with the residual distributions, figure 18 presents the weighted standard deviations σ_w of the secondary vertex pull distributions in x-direction of reconstructed Λ baryons obtained from triple Gaussian fits as a function of p_{T}. Similarly to figure 16, the three panels of figure 18 correspond to different decay radii intervals of the Λ baryon and thus the daughter track parameters were only propagated through air to reconstruct the Λ decay vertex. In addition, $\sigma_w = 1$ is indicated with the black dashed line.
The values of σ_w for the "DCA" case are larger than $\sigma_w = 1$ across the investigated p_{T} range for all three decay radii intervals of the Λ baryon. This result is the same as for the secondary vertex pull distributions of the Ξ baryons discussed in section 5.2.1 and further indicates that the DCA fitter is not able to estimate the uncertainties of the reconstructed secondary vertex correctly. In the "KF" case, where no material is considered, the values of σ_w are compatible within the statistical uncertainties between all three decay radii intervals of the Λ baryon in each p_{T} interval respectively. In the event that the uncertainties are treated correctly, the pull distributions are anticipated to remain unchanged and thus be independent of the amount of material traversed by the daughter particles during the propagation step. However, in all cases, σ_w is larger than $\sigma_w = 1$ over the whole analysed p_{T} range which indicates a slight underestimation of the uncertainties of the reconstructed vertex position. In the "KF+DCA" case, $\sigma_w^{\mathrm{KF+DCA}}$ is smaller compared to σ_w^{KF} in the upper two panels of figure 18 but is compatible with σ_w^{KF} over the whole p_{T} range in the case of minimal material (bottom panel). In that case, the "KF" and "KF+DCA" reconstructions are similar and are therefore expected to yield the same result. Together with the comparable residual distributions in figure 16, the observed result for the pull distributions indicates that the inclusion of material considerations with the DCA fitter code in the reconstruction of the Λ decay vertex leads to an increasing overestimation of the position uncertainties with increasing amount of material. The effects of the propagation with the code of the DCA fitter on the Λ baryon daughter track parameters are discussed further in section 5.2.3.
The observed σ_w p_{T} dependence is compatible with the one found for the Ξ baryon decay vertex position shown in figure 14 for all three reconstruction cases within the statistical uncertainties.
Similar results are found for the secondary vertex pull distributions of the Λ baryon in y- and z-direction in figure 34 and 36 in the appendix.

Analogous to "both at layer no. 3" cases discussed before, figure 19 shows the extracted width of the secondary vertex pull distribution in x-direction of reconstructed Λ baryons as a function of p_{T} corresponding to the case "one at layer no. 3".
The available statistic for the "one at layer no. 3" case, where one Λ daughter has to be propagated through at least one ITS2 layer of material, is about 17 % of the statistic of the "both at layer no. 3" case discussed before. Thus, the p_{T} interval from 4 to 5 GeV/c should be taken out of consideration for the analysis of the pull distributions since the statistics are too low to produce a reasonable fit.
Similarly to figure 18, the extracted values of σ_w from the pull distributions for the "DCA" case in figure 19 are larger than $\sigma_w = 1$ in the investigated p_{T} range for all three decay radii intervals of the Λ baryon.

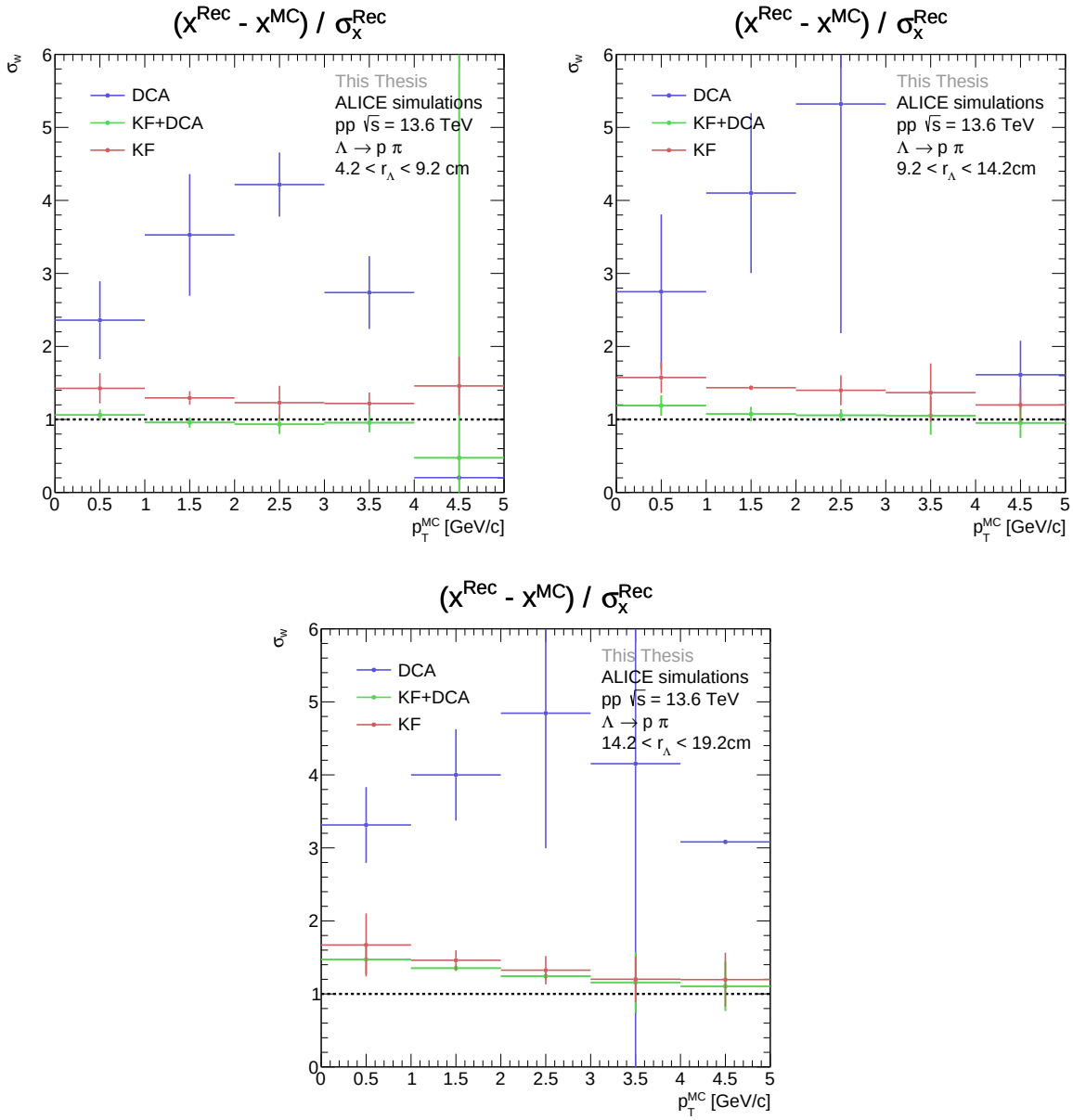

Figure 18: Weighted standard deviations σ_w of secondary vertex **pull distributions** in x-direction of reconstructed Λ baryons for each reconstruction case listed in table 6 obtained from triple Gaussian fits as a function of p_{T} corresponding to the case **"both at layer no. 3"**. Top Left: σ_w against p_{T} for $4.2 < r_\Lambda < 9.2$ cm. Top Right: σ_w against p_{T} for $9.2 < r_\Lambda < 14.2$ cm. Bottom: σ_w against p_{T} for $14.2 < r_\Lambda < 19.2$ cm. DCA case: (blue markers). KF+DCA case: (green markers). KF case: (red markers).

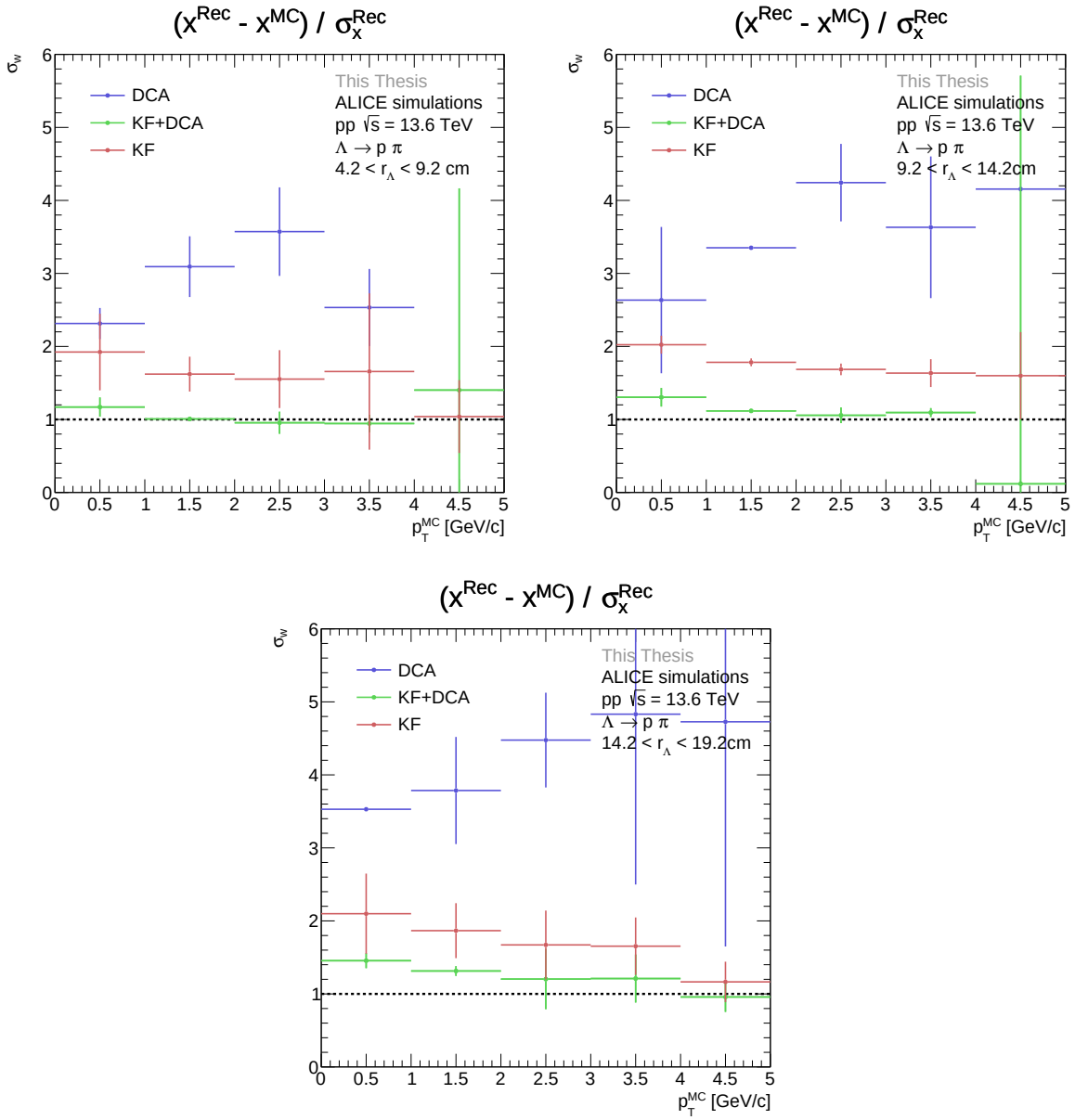

Figure 19: Weighted standard deviations σ_w of secondary vertex **pull distributions** in x-direction of reconstructed Λ baryons for each reconstruction case listed in table 6 obtained from triple Gaussian fits as a function of p_{T} corresponding to the case **"one at layer no. 3"**. Top Left: σ_w against p_{T} for $4.2 < r_\Lambda < 9.2$ cm. Top Right: σ_w against p_{T} for $9.2 < r_\Lambda < 14.2$ cm. Bottom: σ_w against p_{T} for $14.2 < r_\Lambda < 19.2$ cm. DCA case: (blue markers). KF+DCA case: (green markers). KF case: (red markers).

In the "KF" case similar behaviour to figure 18 is observed. The σ_w^{KF} values are compatible between all three decay radii intervals of the Λ baryon. However, in all cases, σ_w^{KF} is larger than the values observed in figure 18 over the whole analysed p_{T} range which indicates a worse underestimation of the uncertainties of the reconstructed vertex position if one of the Λ daughters is propagated through an ITS2 layer of material.
In contrast to figure 18, the $\sigma_w^{\mathrm{KF+DCA}}$ values are not compatible with σ_w^{KF} in all three decay radii intervals of the Λ baryon. This result is expected as the amount of material is not negligible even in the Λ decay radius interval closest to the radial position of ITS2 layer no. 3 (bottom panel) because one of the daughters must be propagated through at least one ITS2 layer of material to the decay vertex position of the Λ baryon. Quantitatively, the $\sigma_w^{\mathrm{KF+DCA}}$ values are closest to $\sigma_w = 1$ and thus indicate that the secondary vertex uncertainties are most accurately estimated when the track propagation is performed with the DCA fitter code in the presence of considerable amounts of material. Still the $\sigma_w^{\mathrm{KF+DCA}}$ values slightly increase going to higher decay radius intervals of the Λ baryon. Therefore a similar conclusion as in figure 18 is possible, that the inclusion of material considerations with the DCA fitter code in the reconstruction of the Λ decay vertex leads to changing pull widths depending on the amount of material considered. The effects of the propagation with the code of the DCA fitter on the Λ baryon daughter track parameters are discussed further in section 5.2.3.
Similar results are found for the secondary vertex pull distributions of the Λ baryon in y- and z-direction in figure 38 and 40 in the appendix.

5.2.3 Position resolution of Λ baryon daughters

In the previous section, it was found that in the mixed "KF+DCA" case, where the code of the DCA fitter is used to propagate the Λ baryon daughter particle parameters and the KFParticle package is used to fit the secondary vertex and reconstruct the Λ baryon, the addition of the propagation with the DCA fitter code to account for material changes the width of the secondary vertex position pull distribution depending on the amount of material considered.
To isolate and investigate the effect of the propagation with the code of the DCA fitter on the Λ baryon daughter particle parameters, the position resolution of the daughter tracks is analysed at the point of the generated Λ decay vertex. Therefore, the proton and pion track parameters are propagated from their respective innermost measurement point to the generated decay vertex position of the Λ baryon. Similarly to section 5.2.2, the analysis of the position resolution of the Λ daughters is performed for different amounts of material in the propagation step. By constraining the Λ decay radius r_Λ and the IU position of the respective Λ daughter, similar material cases as in table 7 are investigated for the proton and the pion which are listed in table 8 with their corresponding topological selections.

	at layer no. 3	at layer no. 4 or no. 5
$4.2 < r_\Lambda < 9.2$ cm	≈ 12.5 cm air; no detector material	> 12.5 cm air; $1-2$ ITS2 layer of material
$9.2 < r_\Lambda < 14.2$ cm	≈ 7.5 cm air; no detector material	> 7.5 cm air; $1-2$ ITS2 layer of material
$14.2 < r_\Lambda < 19.2$ cm	≈ 2.5 cm air; no detector material	> 2.5 cm air; $1-2$ ITS2 layer of material

Table 8: Investigation cases of different amounts of material in the propagation step of the proton and pion from their respective innermost measurement point to the generated Λ baryon decay vertex position.

Analogous to table 7, the Λ baryon is constrained to decay between ITS2 layer no. 2 and layer no. 3 in all six material investigation cases.
In the "at layer no. 3" case, the proton or pion has its respective IU position at layer no. 3 of the ITS2 and is therefore propagated only through air to the generated decay vertex position of the Λ baryon. Similarly to section 5.2.2, the amount of air in the propagation step is determined by the Λ decay radius r_Λ. Quantitatively, this case corresponds to about 90 % of all the protons and pions which stem from a Λ baryon decay.

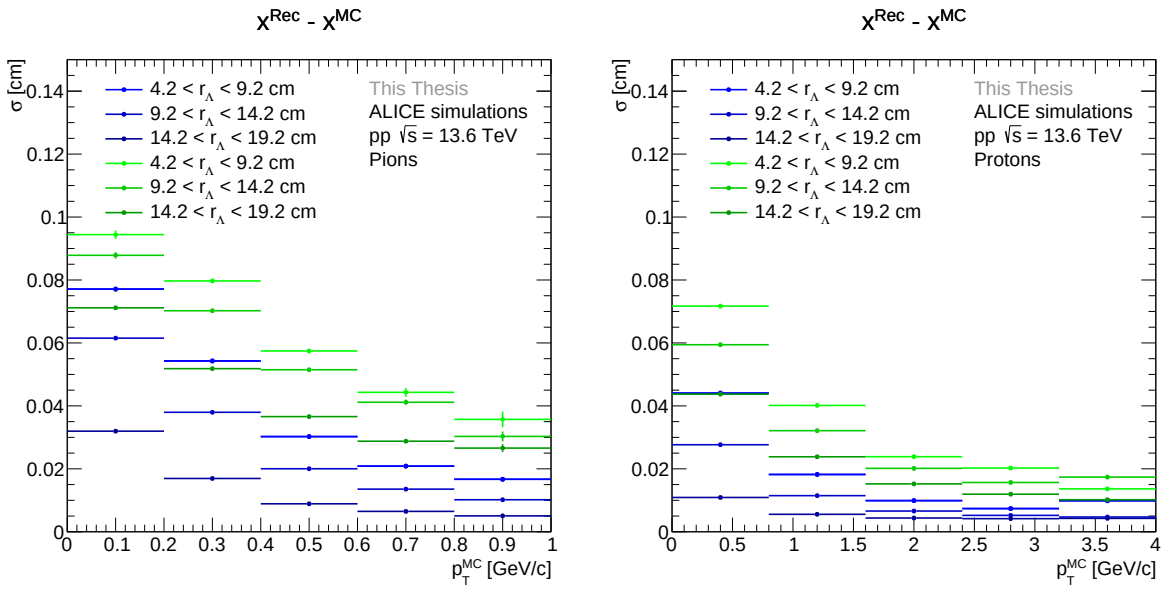

Figure 20: Extracted standard deviations σ of **residual distributions** of the spatial position in x-direction of protons and pions at the generated Λ decay vertex for each material case listed in table 8 as a function of p_T. Left: σ against p_T for pions. Right: σ against p_T for protons. "at layer no. 3" case: (blue markers). "at layer no. 4 or no. 5" case: (green markers).

In the "at layer no. 4 or no. 5" case, the proton or pion has its respective IU position at layer no. 4 or layer no. 5 of the ITS2 depending on whether it is measured in the corresponding layer and is therefore propagated through at least one ITS2 layer of material in addition to air to the generated decay vertex position of the Λ baryon. This case corresponds to the remaining 10 % of the protons and pions, of which about 80 % have their innermost measurement point at layer no. 4.

The residual and pull distributions of the Lambda daughter particles' spatial positions at the generated decay vertex of the respective Λ baryon are investigated for the six material cases of table 8. In this context, the residuals and therefore also the pulls, as discussed in section 3.2, are calculated as the difference between the reconstructed spatial position of the Λ baryon daughter particle after the propagation step to the generated decay vertex of the Λ baryon and the spatial position of the generated Λ baryon decay vertex itself. Since solely the propagation step of the Λ daughter particles is investigated, no secondary vertex fitting or reconstruction of the Λ baryon is involved.
The analysis is performed for different transverse momentum intervals of the proton and the pion, respectively. The results of the investigated material cases of table 8 are shown in figure 20 for the residual distributions and in figure 21 for the pull distributions.

Figure 20 presents the extracted standard deviations σ of the Λ daughters position residual distributions in x-direction at the generated Λ decay vertex for each material case in table 8 as a function of p_T. The p_T-differential distributions of the pion and proton daughters are shown in the left and right panels, respectively. The different material cases are plotted according to their corresponding colour in table 8. The "at layer no. 3" case is displayed in shades of blue and the "at layer no. 4 or no. 5" case is displayed in shades of green. Darker shades indicate that the Λ decay radius interval is closer to the radial position of the fourth ITS2 layer and therefore the Λ baryon daughter is propagated through less air.
Similarly to section 5.2.2, the values of σ decrease and thus the position resolution improves as the distance between the Λ decay vertex and the radial position of the fourth ITS2 layer decreases, both for the blue "at layer no. 3" case and for the green "at layer no. 4 or no. 5" case. In contrast to section 5.2.2, a strong p_T dependence is observed for the σ value distribution for all material cases of table 8 and both Λ baryon daughters. The observed p_T dependence is explained by multiple scattering in the material considered during the propagation of the daughter track parameters. As discussed in section 2.3, the root mean square of the scattering angle scales inversely with p. Thus, the amount of material

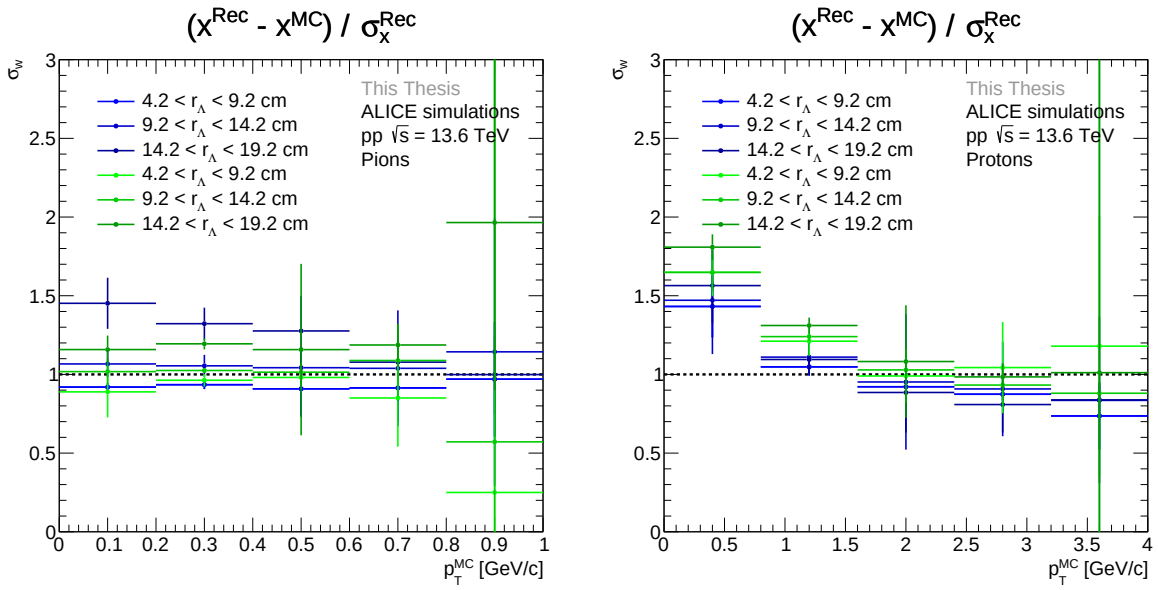

Figure 21: Weighted standard deviations σ of **pull distributions** of the spatial position in x-direction of protons and pions at the generated Λ decay vertex for each material case listed in table 8 obtained from triple Gaussian fits as a function of p_{T}. Left: σ_w against p_{T} for pions. Right: σ_w against p_{T} for protons. "at layer no. 3" case: (blue markers). "at layer no. 4 or no. 5" case: (green markers).

considered during the propagation of the daughter particle parameters contributes to the position resolution at the decay vertex. The aforementioned geometric effect, which is driven by the extrapolation length between the innermost measurement point of the daughter particle and the generated decay vertex of the Λ baryon, also contributes to the distribution of the σ values.
In general, the position resolution of a daughter particle at the decay vertex of the mother particle is driven by the same two effects which drive the impact parameter resolution of a track to the primary vertex discussed in section 2.4.2.
In all three Λ baryon decay radii intervals, the σ values for the green "at layer no. 4 or no. 5" case are larger than for the blue "at layer no. 3" case which can also be explained by the combination of both contributing effects. Firstly, the multiple scattering in a 1 or $2 \times 50\,\mu m$ of silicon in the ITS2 layers is large compared to the multiple scattering in a few centimetres of air in between the ITS2 layers and secondly, in the "at layer no. 4 or no. 5" case the Λ baryon daughter particle is propagated a larger distance from its innermost measurement point to the generated Λ decay vertex compared to the "at layer no. 3" case.
The average p_{T} of the proton is higher than the average p_{T} of the pion, as shown in figure 45 in the appendix. Thus the effect of multiple scattering on the position resolution is stronger for the pion as the root mean square of the scattering angle is inversely proportional to p. As different p_{T} ranges are investigated, the effects explain the differences between the distributions of both Λ daughters.
Similar results are found for the Λ daughter position residuals in y- and z-direction at the generated Λ decay vertex in figure 41 and 43 in the appendix.
The results indicate that the propagation with the code of the DCA fitter might properly treat the discussed effects on the Λ daughter position resolution. However, a quantitative analysis of both effects according to this setup is necessary in order to be able to make a clear and definitive statement.

To estimate how the uncertainties are treated during the propagation step with the DCA fitter code, figure 21 shows the weighted standard deviations σ_w of the Λ daughter position pull distributions at the generated Λ decay vertex in x-direction for each material case in table 8 obtained from triple Gaussian fits as a function of p_{T}. Similarly to figure 20, the left panel shows the values of σ_w against p_{T} for pions whereas the right panel displays the values of σ_w against p_{T} for protons and the different material cases are plotted according to their corresponding colour in table 8. In addition, $\sigma_w = 1$ is indicated with the black dashed line.
Especially in the highest p_{T} interval, it was not possible to produce a reasonable fit of the pull distri-

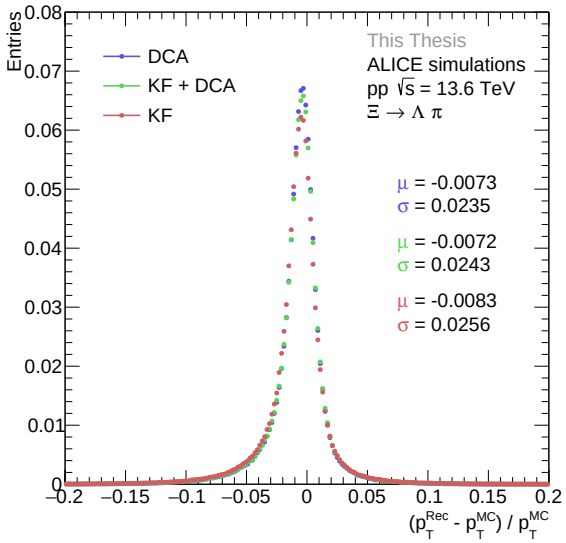

Figure 22: Transverse momentum scaled residual distributions $((p_{\mathrm{T}}^{\mathrm{Rec}} - p_{\mathrm{T}}^{\mathrm{MC}})/p_{\mathrm{T}}^{\mathrm{MC}})$ of the reconstructed Ξ baryons for each reconstruction case listed in table 6. DCA case: (blue markers). KF+DCA case: (green markers). KF case: (red markers).

butions in some of the investigated material cases since the statistics decrease strongly with increasing p_{T}.
For both the blue "at layer no. 3" case and the green "at layer no. 4 or no. 5" case, the values of σ_w increase as the distance between the Λ decay vertex and the radial position of the fourth ITS2 layer decreases. This trend is less pronounced for the protons compared to the pions. Furthermore, for the proton, the σ_w values of the green "at layer no. 4 or no. 5" case are larger than the σ_w values of blue "at layer no. 3" case in all analysed p_{T} intervals. In the case of the pion, on the other hand, no ordering between the "at layer no. 3" and the "at layer no. 4 or no. 5" cases can be observed.
For the σ_w value distribution of the proton (right panel), a p_{T} dependence is observed to larger values of σ_w for decreasing p_{T} which is similar for all investigated material cases listed in table 8 and matches the p_{T} dependence of the σ_w values for the "KF+DCA" case discussed in section 5.2.2. For low p_{T} protons, the pull width even increases to $1.5 - 1.8$, depending on the amount of material, and thus is not compatible with $\sigma_w = 1$ within the statistical uncertainties. The width of the pion pull distributions (left panel), on the other hand, is compatible between the investigated p_{T} intervals within the statistical uncertainties for all presented cases respectively.
The results indicate that the propagation step with the code of the DCA fitter does not properly handle the estimation of the position uncertainties of the Λ daughter particles. This influences the uncertainties of the reconstructed secondary vertex of the Λ baryons which changes the width of the secondary vertex pull distributions depending on the amount of material in the propagation step. In the case of correctly estimated uncertainties, the width and centre of the pull distributions should be independent of the amount of material and the p_{T}.
Similar results for the pull distributions of the spatial positions of the Λ baryon daughters in y- and z-direction at the generated Λ decay vertex are shown in figure 42 and 44 in the appendix.

5.3 Transverse momentum resolution measurements

5.3.1 Transverse momentum resolution of reconstructed Ξ baryons

Figure 22 presents the p_{T} scaled residual distribution of the reconstructed Ξ baryons for the different reconstruction cases ("KF", "KF+DCA", "DCA"). The investigated cases are plotted according to their corresponding colour in table 6 and in addition, the values of the mean μ and the standard deviation σ of the distributions for each reconstruction case are reported.
As described in section 3.2, the scaled residual is calculated as the residual between the reconstructed

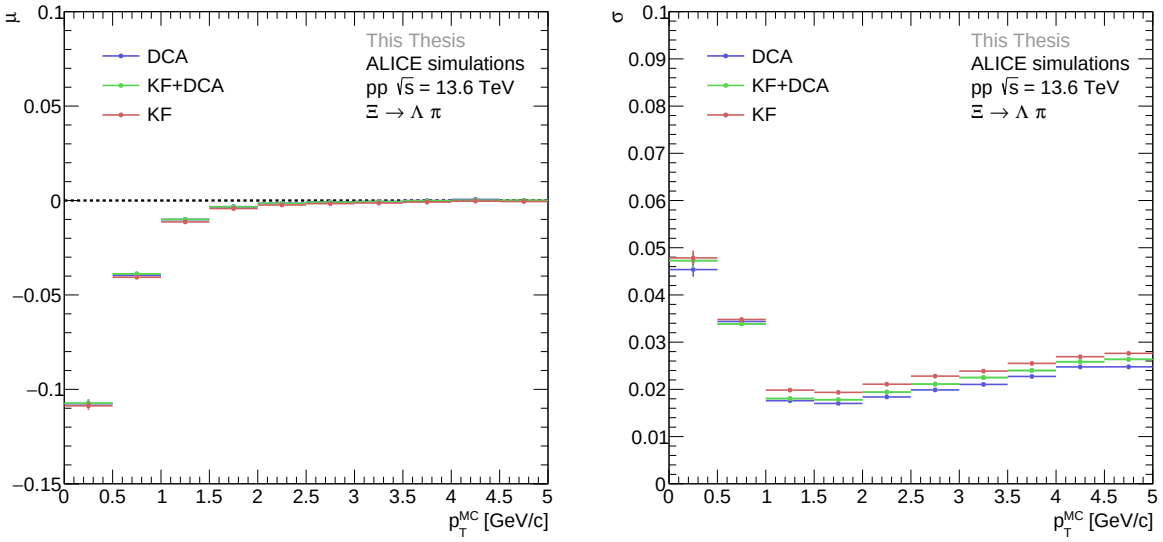

Figure 23: Extracted mean μ and standard deviation σ from the p_{T} scaled **residual distributions** of the **reconstructed Ξ baryons** for each reconstruction case listed in table 6 as a function of p_{T}. Left: μ against p_{T}. Right: σ against p_{T}. DCA case: (blue markers). KF+DCA case: (green markers). KF case: (red markers).

and generated value of a parameter divided (scaled) by its generated value. Investigating the scaled residual distribution allows for quantifying the relative deviations between the generated and reconstructed value of the parameter and estimating its resolution. Comparing the distributions of each reconstruction case and in particular the reported values of μ and σ, the p_{T} of the Ξ baryons is reconstructed with similar resolution in all three cases. Unexpectedly, all three reconstruction cases show a scaled residual distribution which is shifted from 0 to the left and is even asymmetric with a significant tail on the left side, indicating a bias in reconstructing p_{T}. Quantitatively the shift, which is indicated by the value of the mean μ, corresponds to a bias of about $0.7 - 0.8\,\%$ for all three reconstruction cases.
To further investigate the reconstruction performance of the three different reconstruction cases and to find the origin of the observed bias, the reconstructed p_{T} of the Ξ baryons is analysed for different p_{T} intervals.

Figure 23 shows the extracted mean μ and standard deviation σ of the p_{T} scaled residual distributions of the reconstructed Ξ baryons for each reconstruction case listed in table 6 as a function of p_{T} up to 5 GeV/c. On the left panel, the extracted values of μ as a function of p_{T} are plotted and in addition, $\mu = 0$ is indicated with the dashed black line. The extracted σ as a function of p_{T} is shown on the right panel.
The μ values are visually nearly identical for all investigated cases across the analysed p_{T} range thus confirming that the observed bias in reconstructing p_{T} of the Ξ baryons is independent of the reconstruction method. Furthermore, the shift is observed only for low p_{T} Ξ baryons. For Ξ baryons with $p_{\mathrm{T}} > 2$ GeV/c, the values of μ are consistent with $\mu = 0$. The observed shift was analysed not only as a function of p_{T} but also as a function of e.g. the decay radius of the Ξ baryon and other reconstructed features of the Ξ baryon decay chain. However, no significant correlation was found between the shift and each investigated feature. To further investigate the origin of the observed bias, the reconstructed p_{T} of the Λ baryon and its daughters are analysed in section 5.3.2 and section 5.3.3 respectively.
Concerning the values of σ, the "DCA" case has the smallest values of σ whereas the "KF" case has the largest values of σ in all investigated p_{T} intervals. It can be therefore concluded, that the DCA fitter has an up to about 10 % better resolution in reconstructing the p_{T} of Ξ baryons compared to the KFParticle package with and without the propagation step with the code of the DCA fitter. Comparing just the "KF" and the "KF+DCA" case, the p_{T} resolution is up to 7 % worse for the KFParticle package

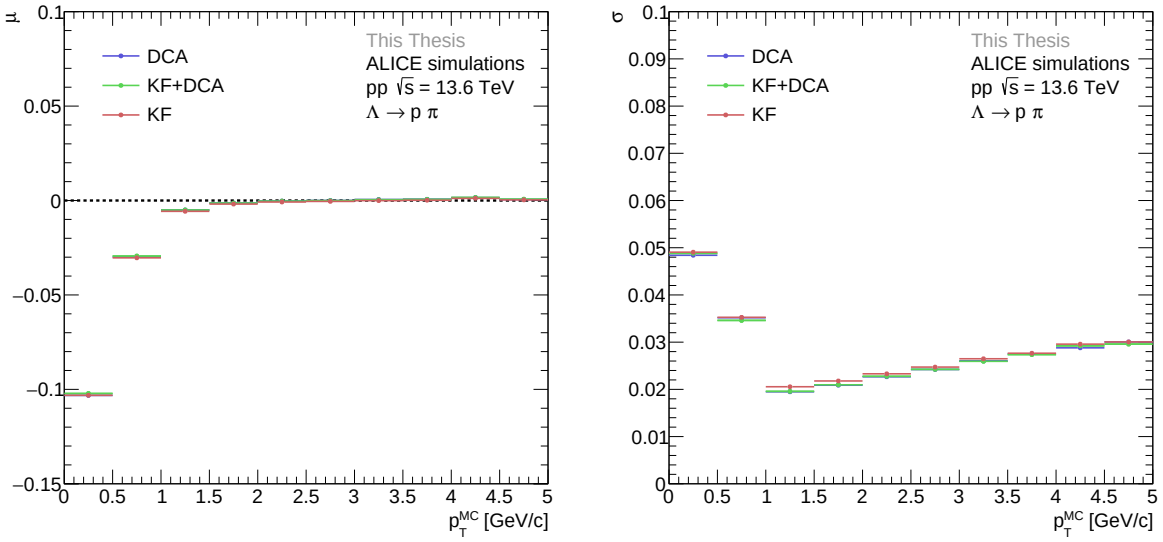

Figure 24: Extracted mean μ and standard deviation σ from the p_{T} scaled **residual distributions** of the **reconstructed Λ baryons** for each reconstruction case listed in table 6 as a function of p_{T}. Left: μ against p_{T}. Right: σ against p_{T}. DCA case: (blue markers). KF+DCA case: (green markers). KF case: (red markers).

without the addition of the propagation with code of the DCA fitter to account for material in the propagation of the Ξ baryon daughters.
Generally, the p_{T} resolution of a particle measured inside the detector is driven by two different effects as discussed in section 2.4.1: Firstly, multiple scattering inside the detector material and air for which the root mean square of the scattering angle scales inversely with p and is therefore mainly relevant for low p_{T} particles as discussed in section 2.3. Secondly, for high p_{T} particles, the measured track is straighter compared to low p_{T} particles which complicates the p_{T} measurement via the radius of curvature due to the limited resolution of the position measurements. Thus, the p_{T} resolution decreases because of the two discussed effects for low and high p_{T} particles. The Ξ baryon is reconstructed from measured particles as the investigated decay of the Ξ baryon is into a measured pion and a Λ baryon which further decays into a measured proton and pion. Therefore, the p_{T} resolution of the Ξ baryon, displayed in the right panel of figure 23, is explained by the two discussed effects which drive the p_{T} resolution of its measured daughters independently of the reconstruction case.
Furthermore, the two discussed effects explain the observed invariant mass resolution of the Ξ baryons shown in figure 11 as the invariant mass resolution mainly depends on the momentum resolution of the Ξ baryon daughters.

5.3.2 Transverse momentum resolution of reconstructed Λ baryons

Figure 24 shows the extracted mean μ and standard deviation σ from the p_{T} scaled residual distributions of the reconstructed Λ baryons for each reconstruction case listed in table 6 as a function of p_{T} up to 5 GeV/c. On the left panel, the extracted values of μ as a function of p_{T} are plotted and in addition, $\mu = 0$ is indicated with the dashed black line. The extracted σ as a function of p_{T} is shown on the right panel.
Analogous to the Ξ baryons investigated before in section 5.3.1, the μ values of the Λ baryon are compatible for the three different reconstruction cases which confirms that the observed bias in reconstructing p_{T} is independent of the reconstruction method for both the Ξ and the Λ baryon. Furthermore, a similar shift as for the Ξ baryons in the values of μ at low p_{T} is observed for the Λ baryon. As the p_{T} of the Λ baryon is reconstructed from its measured daughter particles with their corresponding p_{T}, the reconstructed p_{T} of both Λ baryon daughters is analysed in section 5.3.3 to investigate the origin of the observed bias for the Ξ and the Λ baryon.
Concerning the values of σ, the "KF" case has the largest values of σ across the investigated p_{T} range

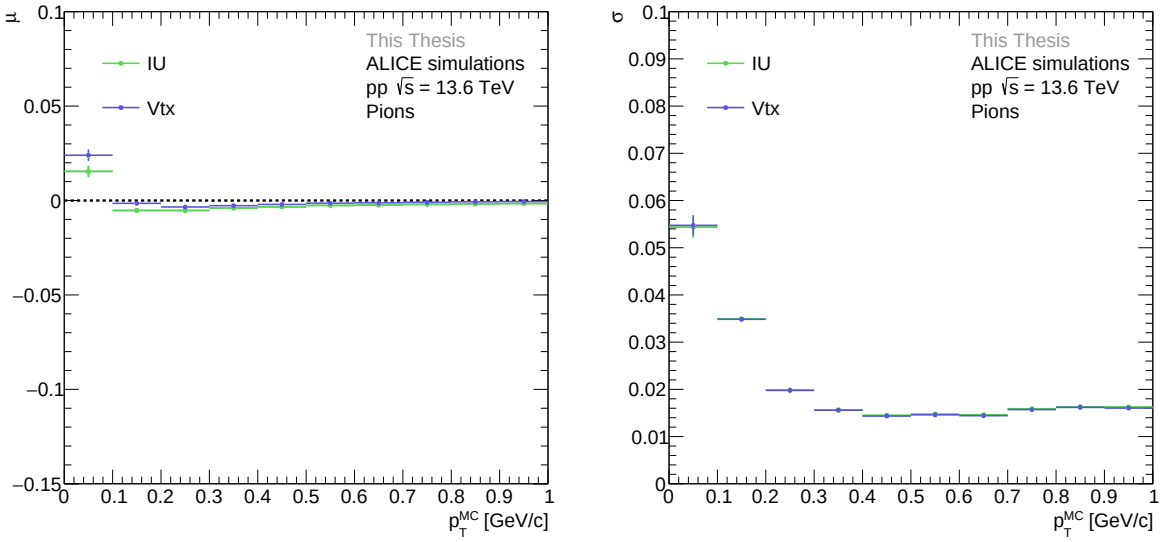

Figure 25: Extracted mean μ and standard deviation σ from the p_{T} scaled **residual distributions** of **pions** at their IU and the decay vertex of the Λ baryon as a function of p_{T}. Left: μ against p_{T}. Right: σ against p_{T}. at IU: (green markers). at Vtx: (blue markers).

and is even incompatible with the other analysed cases in some p_{T} intervals. In contrast to section 5.3.1, the "KF+DCA" and the "DCA" case are compatible within the statistical uncertainties. It could therefore be concluded, that the p_{T} resolution of the reconstructed Λ baryon is up to about 3 % worse in the case of the pure KFParticle package compared to the "KF+DCA" and the "DCA" cases. However, the available statistics are not sufficient to permit a strong and final statement. Generally, the p_{T} resolution of the Λ baryon is similar to the p_{T} resolution of the Ξ baryon displayed in figure 23 as the Λ baryon is reconstructed from measured daughter particles as well and therefore its transverse momentum resolution is explained by the two discussed effects in section 5.3.1.
In summary, similar results are observed for the p_{T} resolution of the Λ baryon compared to the p_{T} resolution of the Ξ baryon.

5.3.3 Transverse momentum resolution of Λ baryon daughters

In the previous sections, a bias to reconstruct smaller values of p_{T} compared to the generated value p_{T}^{MC} was found for both the Ξ and the Λ baryon at low p_{T} independently of the reconstruction case. The p_{T} resolution of the Λ baryon daughters is investigated to check whether the propagation of the particles‘ parameters deteriorates the p_{T} measurement and to find the origin of the observed bias for the Ξ and the Λ baryon. Therefore, the p_{T} resolution of the Λ baryon daughters is analysed at their respective innermost measurement points and at the generated secondary vertex position of the Λ baryon. Since solely the propagation step of the Λ daughter particles is investigated, no secondary vertex fitting or reconstruction of the Λ baryon is involved. Therefore, the transverse momentum resolution is analysed only twice, before and after the propagation with the code DCA fitter which is used in the "DCA" and the "KF+DCA" case.
In addition, the p_{T} pull distributions of the Λ baryon daughters are analysed to verify whether the propagation step with the code of the DCA fitter deteriorates the p_{T} uncertainties similar to section 5.2.3 for the position uncertainties of the Λ baryon daughter particles. The analysis is performed for different p_{T} intervals of the protons and the pions respectively. The results of the investigated scaled residual distributions are shown in figure 25 for the pions and figure 26 for the protons. Furthermore, the results of the investigated pull distributions are shown in figure 27 for the protons and the pions.

Figure 25 and figure 26 show the extracted means μ and standard deviations σ from the transverse momentum scaled residual distributions of pions and protons respectively at their respective innermost

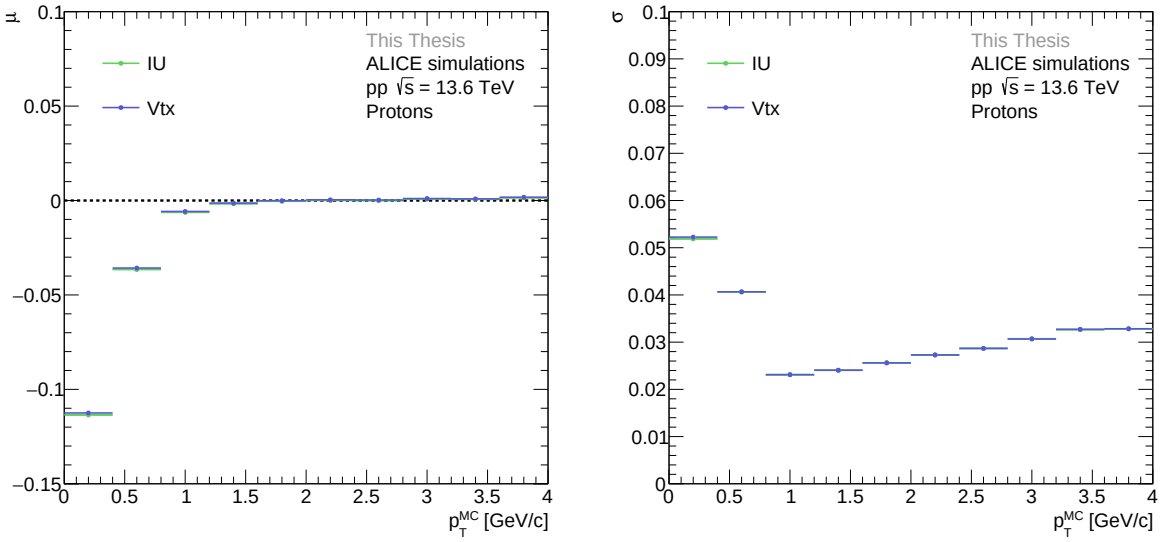

Figure 26: Extracted mean μ and standard deviation σ from the p_{T} scaled **residual distributions** of **protons** at their IU and the decay vertex of the Λ baryon as a function of p_{T}. Left: μ against p_{T}. Right: σ against p_{T}. at IU: (green markers). at Vtx: (blue markers).

measurement points and at the generated decay vertex position of the Λ baryon as a function of p_{T} up to 1 GeV/c for the pions and 4 GeV/c for the protons. On the left panels, the extracted values of μ as a function of p_{T} are plotted and in addition, $\mu = 0$ is indicated with the dashed black line. The extracted values of σ as a function of p_{T} are shown on the right panels.
As a first observation, the values of μ and σ at the innermost measurement points are compatible within the statistical uncertainties with the values at the generated decay vertex position of the Λ baryon for both Λ baryon daughters. Only for the pions at very low p_{T}, the values of μ deviate about 1 % between the investigated cases. This is expected as the propagation step with the code of the DCA fitter slightly impacts the p_{T} measurement for particles with very low p_{T} because of multiple scattering inside the detector discussed in section 2.3. Therefore, the propagation step does not deteriorate the p_{T} measurements.
For the extracted values of μ, the pion is compatible with $\mu = 0$ across the investigated p_{T} range and only for low p_{T}, where the statistics decrease rapidly, the values deviate about 2 % from $\mu = 0$. The small shift indicates that the reconstructed p_{T} is larger than the generated value p_{T}^{MC} which is contrary to the observed shifts for the Ξ and the Λ baryon. Thus, the pion seems not to be the origin of the observed bias as the p_{T} of the pion is reconstructed correctly.
For the extracted μ values of the protons, a shift to values below $\mu = 0$ is observed which is very similar to the shifts for the Ξ and the Λ baryon discussed before. It can be thus inferred that the proton is the most probable origin of the observed shift for the Ξ and the Λ baryon, given that the measured p_{T} of the proton influences the reconstructed p_{T} of its mother particles.
According to section 2.2 in which the track reconstruction in the ITS2 and the TPC is discussed, tracking of charged particles is done with the information of a preliminary PID and at the start of Run 3 of the LHC, according to which the investigated MC sample is modelled, all charged particles are tracked as pions. For protons which are tracked with the PID hypothesis of a pion but have a larger mass than the pions, the reconstructed p_{T} is smaller than if it was tracked correctly as a proton. This is mainly due to the increased energy loss via ionisation and excitation according to the Bethe-Bloch formula of a proton compared to a pion with the same momentum which results in a larger change of the radius of curvature which is used to measure the transverse momentum as discussed in section 2.4.1. This effect should be particularly noticeable at low p_{T} where the energy loss is larger compared to high p_{T}. Therefore, the discussed effect is a possible explanation for the observed bias in reconstructing p_{T} of the proton and subsequently for the observed shifts for the Ξ and Λ baryon.
For the extracted values of σ, the shape of the distributions for the protons and pions respectively are comparable to the distribution of the Ξ and Λ baryons discussed before but shifted towards smaller p_{T}

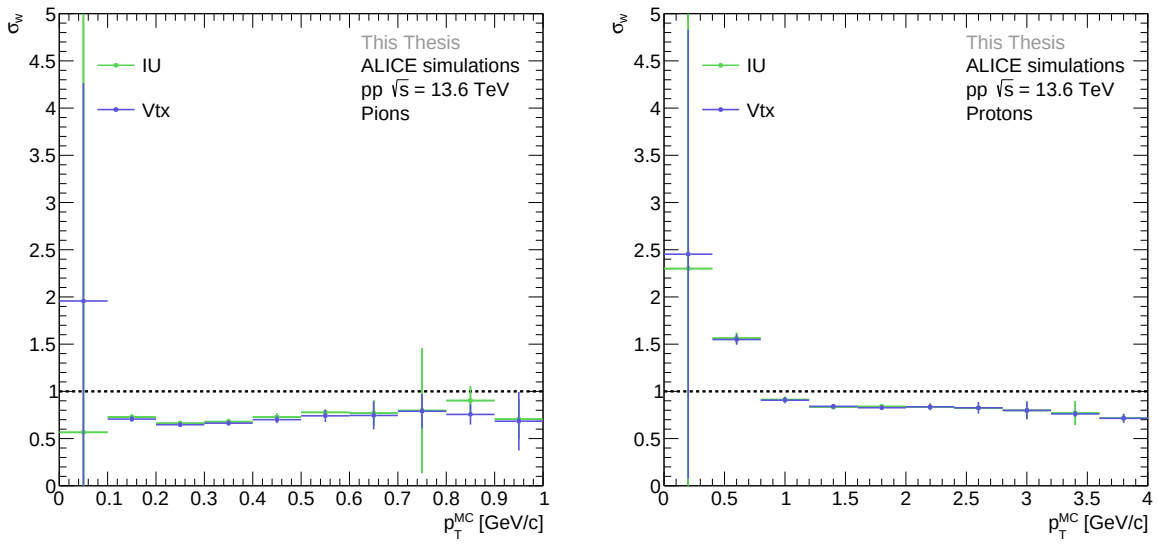

Figure 27: Weighted standard deviation σ_w from the p_{T} **pull distributions** of **protons and pions** at their respective IU and the decay vertex of the Λ baryon obtained from a triple Gaussian fit as a function of p_{T}. Left: σ_w against p_{T} for pions. Right: σ_w against p_{T} for protons. at IU: (green markers). at Vtx: (blue markers).

which is particularly noticeable for the pions. The p_{T} resolution for the protons and pions is explained by the two different effects for the charged particles measured inside the detector which are discussed in section 2.4.1. The contribution due to multiple scattering is inversely proportional to p and β. The second contribution due to the limited resolution of position measurements scales linearly with p_{T} and is relevant for high-momentum particles as their tracks become straighter. Thus, the point or p_{T} value which indicates whether multiple scattering or track straightness is the dominant contribution to the p_{T} resolution of the measured particle, is different for the protons and pions because of their different masses. In summary, these effects describe the σ value distribution for the protons and pions respectively which subsequently explain the observed p_{T} resolutions of the reconstructed Ξ and Λ baryons.

To estimate how the p_{T} uncertainties are treated during the propagation step with the DCA fitter, figure 27 shows the weighted standard deviations σ_w from the p_{T} pull distributions of protons and pions at their respective innermost measurement points and at the generated decay vertex position of the Λ baryon obtained from triple Gaussian fits as a function of p_{T}. The left panel shows the extracted values of σ_w as a function of p_{T} up to 1 GeV/c for pions whereas the right panel displays the values of σ_w as a function of p_{T} up to 4 GeV/c for protons. In addition, $\sigma_w = 1$ is indicated with the black dashed line and therefore values of $\sigma_w > 1$ correspond to an underestimation of the p_{T} uncertainties while values of $\sigma_w < 1$ correspond to an overestimation of the p_{T} uncertainties. The first p_{T} intervals should be taken out of consideration for both Λ baryon daughters as there are too few protons or pions respectively to produce a reasonable fit.
Similarly to the p_{T} scaled residual distributions discussed before, the values of σ_w at the innermost measurement points are compatible with the values at the generated decay vertex position of the Λ baryon for both the protons and the pions across the investigated p_{T} range. Therefore, the propagation step with the code of the DCA fitter does not deteriorate the p_{T} measurements or the estimation of the p_{T} uncertainties.
Furthermore, the σ_w values are compatible within the statistical uncertainties between all analysed p_{T} intervals for both Λ baryon daughters. In the case of correctly estimated uncertainties, the width and centre of the pull distributions should be independent of the p_{T} and are anticipated to remain unchanged. Only for protons at low p_{T}, the σ_w values increase which is most probably due to the observed shift in reconstructing the p_{T} of the proton. Since the deviation between the reconstructed and the generated value of p_{T} increases at low p_{T}, the uncertainties underestimate the deviation and thus the σ_w value of the pull increases. Quantitatively, the values of σ_w are up to 25 % below $\sigma_w = 1$

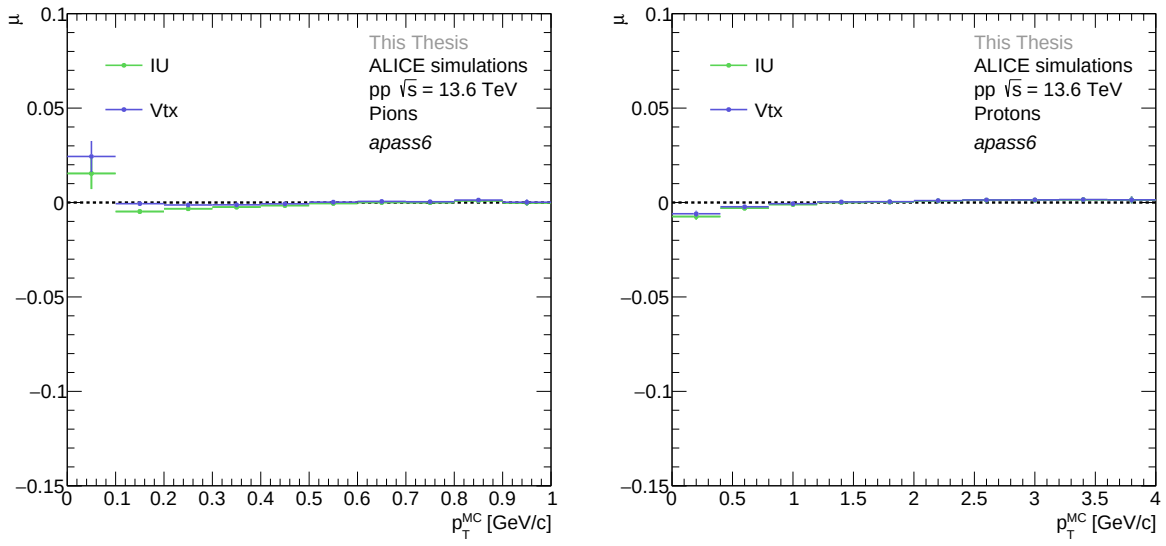

Figure 28: Extracted means μ from the p_{T} scaled residual distributions of **protons and pions** at their respective IU and the decay vertex of the Λ baryon as a function of p_{T}. Left: μ against p_{T} for pions. Right: μ against p_{T} for protons. at IU: (green markers). at Vtx: (blue markers). **Monte-Carlo anchored to apass6**.

for both Λ baryon daughters and therefore indicate a slight overestimation of the p_{T} uncertainties.

5.4 Performance studies with improved data production sample

As described in section 5, the general purpose Monte Carlo investigated before was modelled using the Run 3 ALICE setup of 2022 and closely resembles the real recorded data. Generally, the data obtained during the runs are reconstructed on multiple occasions, for instance, in the context of updates to the detector calibration and reconstruction software. These reconstruction passes over the entire data set are referred to as *apass*. To mimic the reconstruction of the data, the analysed Monte Carlo sample is anchored to the latest available apass, in this instance to the so-called *apass4*, which means that the sample is generated with the same reconstruction software version and the same detector calibration as used in data at that particular time. Furthermore, anchoring takes into account possible errors in the detector during data acquisition, for example, dead channels etc.
The results regarding the bias in the reconstruction of smaller p_{T} values discussed before were reported and during the time of the analysis, the reconstruction in data was improved and a new data reconstruction pass called *apass6* was produced. Subsequently, a new Monte-Carlo sample was produced with the exact specifications as discussed in section 5 but anchored to the apass6 reconstruction pass. Among other things, the calibration of the data and the reconstruction software have been improved. In addition, PID was introduced during tracking, which was not included in the previous apass4 reconstruction pass. Therefore, protons and pions can be tracked with a preliminary PID hypothesis as discussed in section 2.2 and not only as pions as in the reconstruction of apass4.
A difference between the two data reconstruction passes was found for the p_{T} residuals of the Ξ baryon, the Λ baryon and the proton track coming from the decay of the Λ baryon. The results are discussed in the following.

Figure 28 presents the extracted means μ from the scaled p_{T} residual distributions of pions and protons at their respective innermost measurement points and at the decay vertex position of the Λ baryon as a function of p_{T}. The extracted values of μ against p_{T} are displayed for pions on the left panel and for protons presented on the right panel. In addition, $\mu = 0$ is indicated with the black dashed line.
Similarly to section 5.3.3, the values of μ at the innermost measurement points are compatible with those at the decay vertex of the Λ baryon for both daughter particles. Furthermore, the μ value

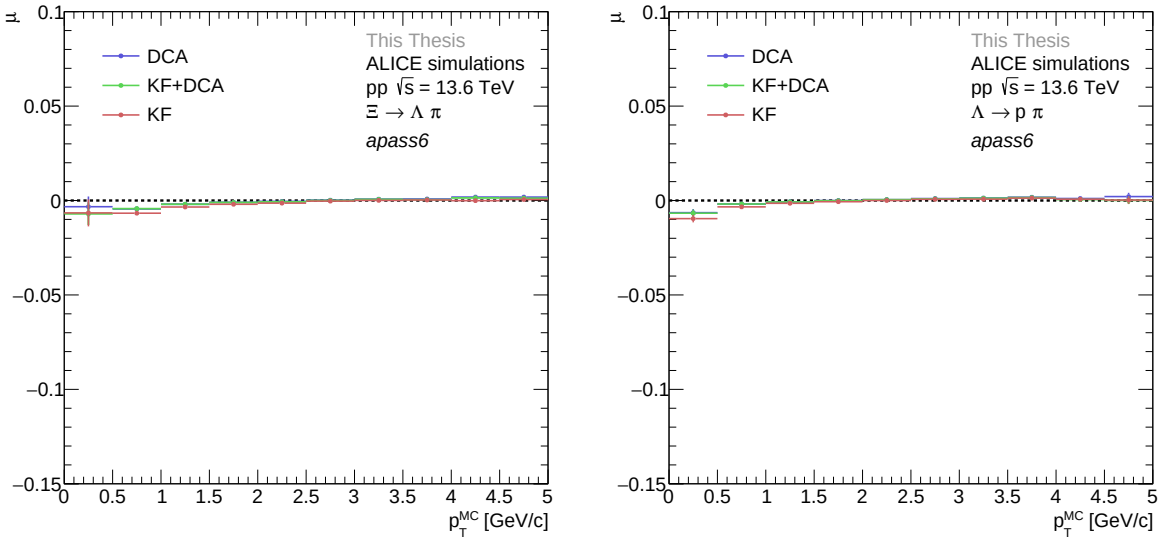

Figure 29: Extracted means μ from the p_T scaled residual distributions of Ξ **and** Λ **baryons** for each reconstruction case listed in table 6 as a function of p_T. Left: μ against p_T for Ξ baryon. Right: μ against p_T for Λ baryons. DCA case: (blue markers). KF+DCA case: (green markers). KF case: (red markers). **Monte-Carlo anchored to apass6**.

distributions of the pions (left panel) are found to be compatible with the apass4 reconstruction pass presented in figure 25. In the case of the protons (right panel), the shift to negative values which was observed at low p_T for the apass4 reconstruction pass shown in figure 26 is not measured anymore and only small deviations, below 1 % from $\mu = 0$ are observed. Therefore, the bias towards reconstructing smaller p_T values compared to the generated value for low p_T protons is not observed anymore in the improved data reconstruction. As PID in tracking is enabled in the apass6 reconstruction pass, this result further indicates that the observed shift in the MC sample anchored to the apass4 reconstruction pass is due to the unused PID hypothesis.

Analogous to the Λ daughters discussed before, figure 29 shows the extracted means μ from the scaled p_T residual distributions of Ξ and Λ baryons for each reconstruction case listed in table 6 as a function of p_T.
The shift towards negative values of μ at low p_T is not observed anymore for Ξ and Λ baryons in the MC sample anchored the apass6 reconstruction pass. This result further indicates that the bias towards reconstructing smaller p_T values compared to the generated value of protons is most likely the origin of the observed shifts for the Ξ and Λ baryons. Nevertheless, the Ξ and Λ p_T resolutions (σ distributions) were found to be compatible between the two data reconstruction passes.
Similarly, all other remaining results discussed in this chapter were found to be compatible between the apass4 and the apass6 reconstruction passes.

6 Summary and Outlook

This thesis investigated the reconstruction of the Ξ baryon via its weak hadronic decay in proton-proton collisions at $\sqrt{s} = 13.6$ TeV with ALICE in LHC Run 3. Starting with studies of signal extraction in data, a set of topological selections was developed to serve as a reference and starting point for future physics analyses of Ξ and Ξ_c^+ baryons. Using Monte Carlo simulations for the decay of $\Xi \to \Lambda\,\pi \to p\,\pi\,\pi$, the secondary vertex, invariant mass and transverse momentum resolution were analysed for Ξ and Λ baryons reconstructed with the KFParticle package and the DCA fitter with the aim to enhance the reconstruction precision of the Ξ baryon decay.
For the comparison of the two reconstruction algorithms, three reconstruction cases were investigated which differ in whether the propagation of particle tracks within the detector and the complete vertex fit with the reconstruction of the mother particle is performed with the KFParticle package or the DCA fitter. It was found that the choice of reconstruction algorithm does not affect the invariant mass resolution of the reconstructed Ξ baryons. Similar observations have been made for the transverse momentum resolution of the Ξ baryons. A bias towards an underestimation of the transverse momentum was observed independently of the reconstruction case both for the reconstructed Ξ and the Λ baryon in the cascade decay. In a next step, the transverse momentum resolution of the Ξ baryon daughters i.e. the reconstructed Λ baryon and its daughter tracks were investigated to determine the origin of the observed shift. By comparing to an improved MC production sample including PID information during the tracking, it was found that a wrong mass hypothesis during the tracking procedure for low p_{T} proton tracks might contribute to a bias towards reconstructing smaller p_{T} values.
The position resolution of the reconstructed Ξ and Λ baryon decay vertex was found to be compatible between the three investigated reconstruction cases. However, it was shown that the secondary vertex position uncertainties are significantly underestimated by the DCA fitter during the reconstruction. The uncertainty estimation improves if the KFParticle package is employed for the vertex fit itself. The KFParticle package is independent of the detector geometry and does not take into account any material during track propagation.
Consequently, the secondary vertex resolution of the Λ baryon and the position resolution of the Λ baryon daughters were investigated for different amounts of material considered during the propagation of the daughter parameters from their measurement point to the reconstructed decay vertex position. It was demonstrated that the track parameter propagation with the code of the DCA fitter changes the width of the secondary vertex pull distributions of the Λ baryon depending on the amount of material considered during the propagation of the Λ daughters. In particular, it was shown that the position uncertainties of the propagated Λ daughters at the reconstructed decay vertex tend to get underestimated especially at low p_{T} for increasing amounts of material in the propagation. The results serve as evidence that the daughter particle position uncertainties may not be treated correctly during the propagation of their parameters with the DCA fitter code.
A quantitative analysis within the material studies revealed that the material considered by the DCA fitter is primarily relevant for only about 15 % of the reconstructed Λ baryon candidates, where the daughters were propagated through an ITS2 layer to reconstruct the secondary vertex. Together with the result that the secondary vertex resolution is compatible between all investigated reconstruction cases, independently of the inclusion of material, it can be concluded that the KFParticle package alone is the best choice for the reconstruction of the decay chain of the Ξ baryon.

At the time of the analysis, the ALICE Run 3 data reconstruction is still under development. Therefore, the results presented in this thesis reflect the status of the Run 3 data reconstruction at the time of its submission. Consequently, it would be advantageous to conduct a continuous investigation of the various reconstruction methods employed in the latest reconstruction passes. This investigation should also consider future reconstruction passes with possible reconstruction improvements. Furthermore, it would be beneficial to extend the studies to heavy-ion collisions. This would allow for a comparison of the reconstruction performance in the high charged particle multiplicity environment observed in heavy-ion collisions to the performance in pp collisions. Here, the methods developed in this thesis could be employed to assess the reconstruction performance of the Ξ baryon. In addition, analogous material-dependent studies could be conducted utilising primary tracks to investigate their impact parameter resolution. The mentioned studies could potentially permit further insights into the effect of the propagation of track parameters with the code of the DCA fitter.

In conclusion, this thesis presented a comparison of different algorithms for the reconstruction of the decay of the Ξ baryon to a Λ baryon and a pion. The results presented in this thesis provide valuable input for the full reconstruction of Ξ and Ξ_c^+ baryons in ALICE Run 3 data.

References

[1] N. Cabibbo and G. Parisi. Exponential hadronic spectrum and quark liberation. *Physics Letters B*, 59(1):67–69, 1975.

[2] P. Koch, B. Muller, and J. Rafelski. Strangeness Production and Evolution in Quark Gluon Plasma. *Z. Phys. A*, 324:453–463, 1986.

[3] J. Adam et al. ALICE Collaboration. Enhanced production of multi-strange hadrons in high-multiplicity proton–proton collisions. *Nature Physics*, 13(6):535–539, Apr 2017.

[4] S. Acharya et al. ALICE Collaboration. Charm production and fragmentation fractions at midrapidity in pp collisions at $\sqrt{s} = 13$ tev. *Journal of High Energy Physics*, 2023(12), Dec 2023.

[5] S. Acharya et al. ALICE Collaboration. Charm-quark fragmentation fractions and production cross section at midrapidity in pp collisions at the lhc. *Physical Review D*, 105(1), Jan 2022.

[6] S. Acharya et al. ALICE Collaboration. Λ_c^+ production and baryon-to-meson ratios in pp and p-pb collisions at $\sqrt{s_{\rm NN}} = 5.02$ TeV at the lhc. *Phys. Rev. Lett.*, 127:202301, Nov 2021.

[7] Carolina Reetz. Measurement of Ξ_c^+ in proton–proton collisions at $\sqrt{s} = 13$ TeV with ALICE detector. Master Thesis, 2022.

[8] Arturo Tauro. ALICE Schematics. General Photo, May 2017.

[9] ALICE Collaboration. Alice upgrades during the lhc long shutdown 2, Feb 2023.

[10] B. Abelev et al. ALICE Collaboration. Technical Design Report for the Upgrade of the ALICE Inner Tracking System. Technical report, J. Phys. G: Nucl. Part. Phys. 41 087002, 2014.

[11] Hermann Kolanoski and Norbert Wermes. *Particle Detectors: Fundamentals and Applications.* Oxford University Press, Jun 2020.

[12] R. L. Workman et al. Particle Data Group. Review of Particle Physics. *Progress of Theoretical and Experimental Physics*, 2022(8):083C01, Aug 2022.

[13] Sergey Gorbunov. *On-line reconstruction algorithms for the CBM and ALICE experiments.* doctoralthesis, Universitätsbibliothek Johann Christian Senckenberg, 2013.

[14] Maksym Zyzak. *Online selection of short-lived particles on many-core computer architectures in the CBM experiment at FAIR.* doctoralthesis, Universitätsbibliothek Johann Christian Senckenberg, 2016.

[15] Valentina Akishina, Ivan Kisel, Igor Kulakov, and Maksym Zyzak. FLES - First Level Event Selection Package for the CBM Experiment. In *GPU Computing in High-Energy Physics*, pages 23–29, 2015.

[16] Lisa-Katrin Kümmerer. Optimization of CBM physics performance for Ξ_- baryon yield measurements with machine learning techniques. Bachelor Thesis, 2023.

[17] Phil Lennart Stahlhut. Performance test of the KF Particle package for open heavy-flavour baryon reconstruction with ALICE. Bachelor Thesis, 2023.

Appendix

Signal extraction studies in data

V0s

Cut	Description
V0Rad >= 1.0 cm	Reconstructed decay radius of a V0 inside the detector
DCAV0Dau <= 1.0 cm	Distance of closest approach between V0 daughters
abs(DCANegToPV) >= 0.1 cm	Distance of closest approach between negative V0 daughter and PV
abs(DCAPosToPV) >= 0.1 cm	Distance of closest approach between positive V0 daughter and PV
cos(PAV0ToPV) >= 0.5	Pointing angle of V0 pointing back to the PV

Cascades

Cut	Description
CascRad >= 1.0 cm	Reconstructed decay radius of a cascade inside the detector
DCACascDau <= 1.0 cm	Distance of closest approach between Cascade daughters
abs(DCABachToPV) >= 0 cm	Distance of closest approach between bachelor particle and PV
abs(MassV0 - 1.116 GeV/c^2) <= 0.01 GeV/c^2	Invariant mass window of the V0
cos(PACascToPV) >= 0.9	Pointing angle of Cascade pointing back to the PV

Table 9: Preselection criteria used for the reconstruction of cascade candidates.

Invariant mass resolution of reconstructed Ξ baryons

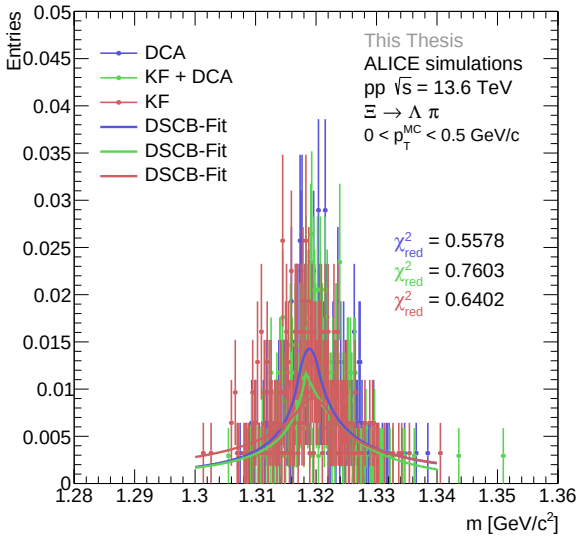

Figure 30: Fits of a DSCB according to equation 14 to invariant mass distribution of the reconstructed Ξ baryons for each reconstruction case listed in table 6 with transverse momentum $0 < p_{\mathrm{T}} < 0.5$ GeV/c. DCA case: (blue markers). KF+DCA case: (green markers). KF case: (red markers).

Secondary vertex resolution of reconstructed Ξ baryons

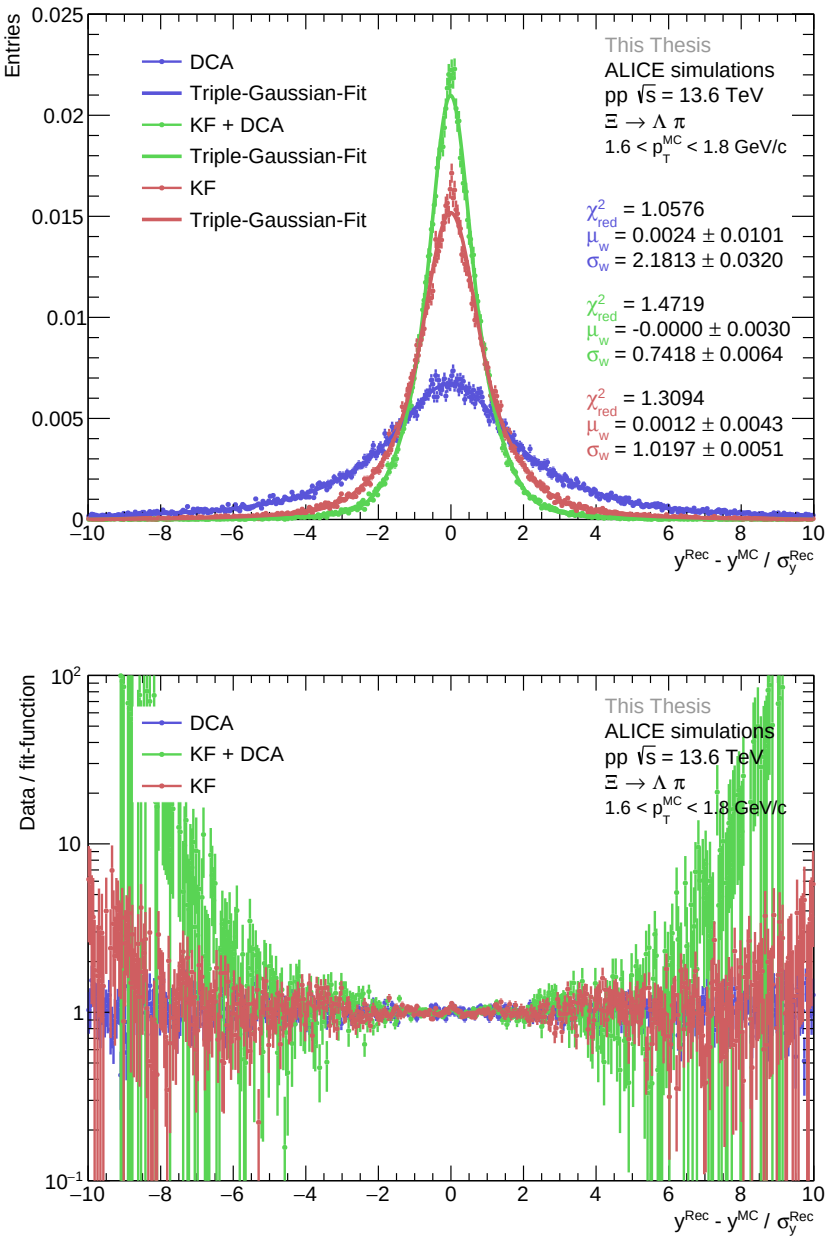

Figure 31: Fits of a triple Gaussian according to equation 10 with $n = 3$ to the secondary vertex pull distribution in y-direction of the reconstructed Ξ-baryons for each reconstruction case in table 6 with transverse momentum $1.6 < p_{\mathrm{T}} < 1.8$ GeV/c. Top: SV pull distribution with fitted triple Gaussian. Bottom: Ratio plot between data and the fit-functions.

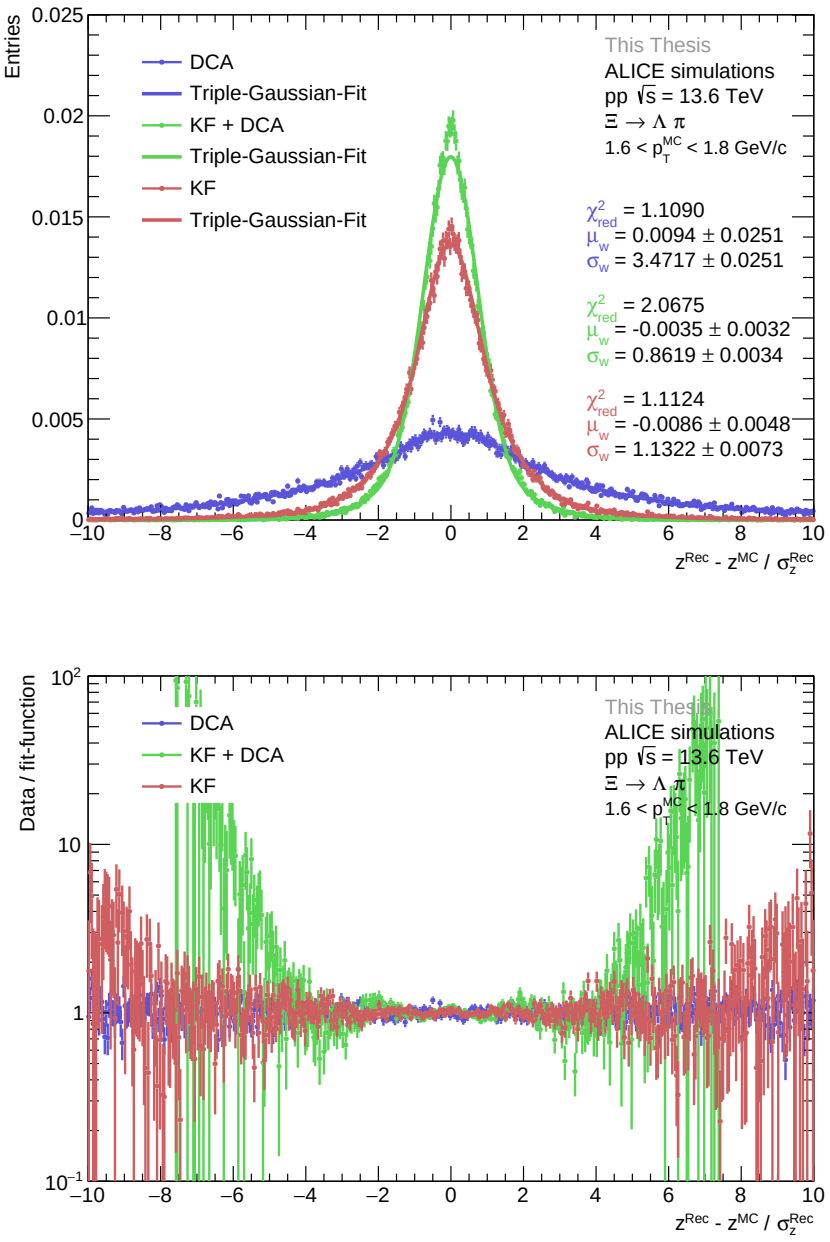

Figure 32: Fits of a triple Gaussian according to equation 10 with $n = 3$ to the secondary vertex pull distribution in z-direction of the reconstructed Ξ-baryons for each reconstruction case in table 6 with transverse momentum $1.6 < p_{\mathrm{T}} < 1.8$ GeV/c. Top: SV pull distribution with fitted triple Gaussian. Bottom: Ratio plot between data and the fit-functions.

Secondary vertex resolution of reconstructed Λ baryons

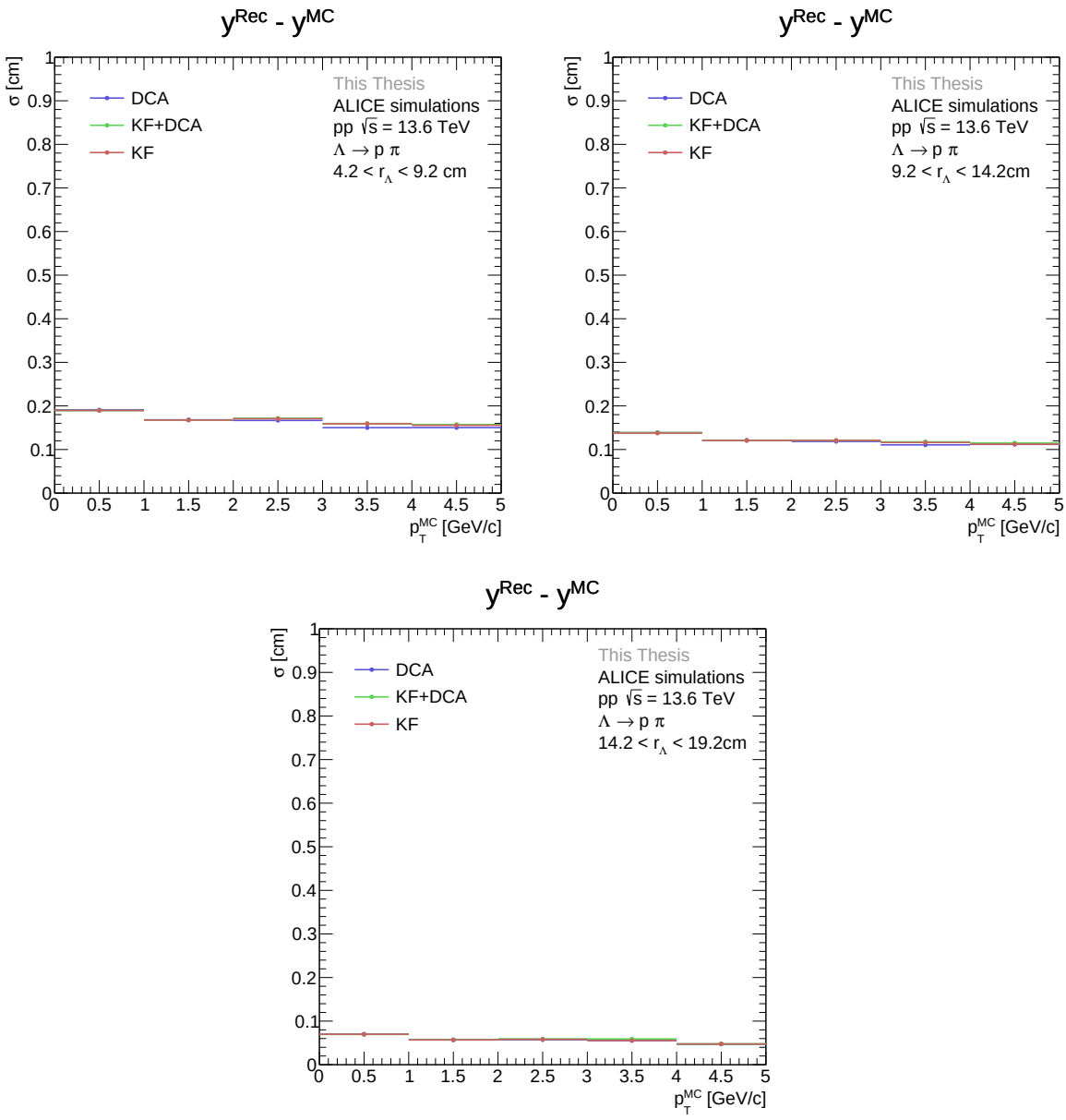

Figure 33: Extracted standard deviations σ of secondary vertex residual distributions in y-direction of reconstructed Λ baryons for each reconstruction case in table 6 as a function of p_{T} corresponding to the case "both at layer no. 3". Top Left: σ against p_{T} for $4.2 < r_\Lambda < 9.2$ cm. Top Right: σ against p_{T} for $9.2 < r_\Lambda < 14.2$ cm. Bottom: σ against p_{T} for $14.2 < r_\Lambda < 19.2$ cm. DCA case: (blue markers). KF+DCA case: (green markers). KF case: (red markers).

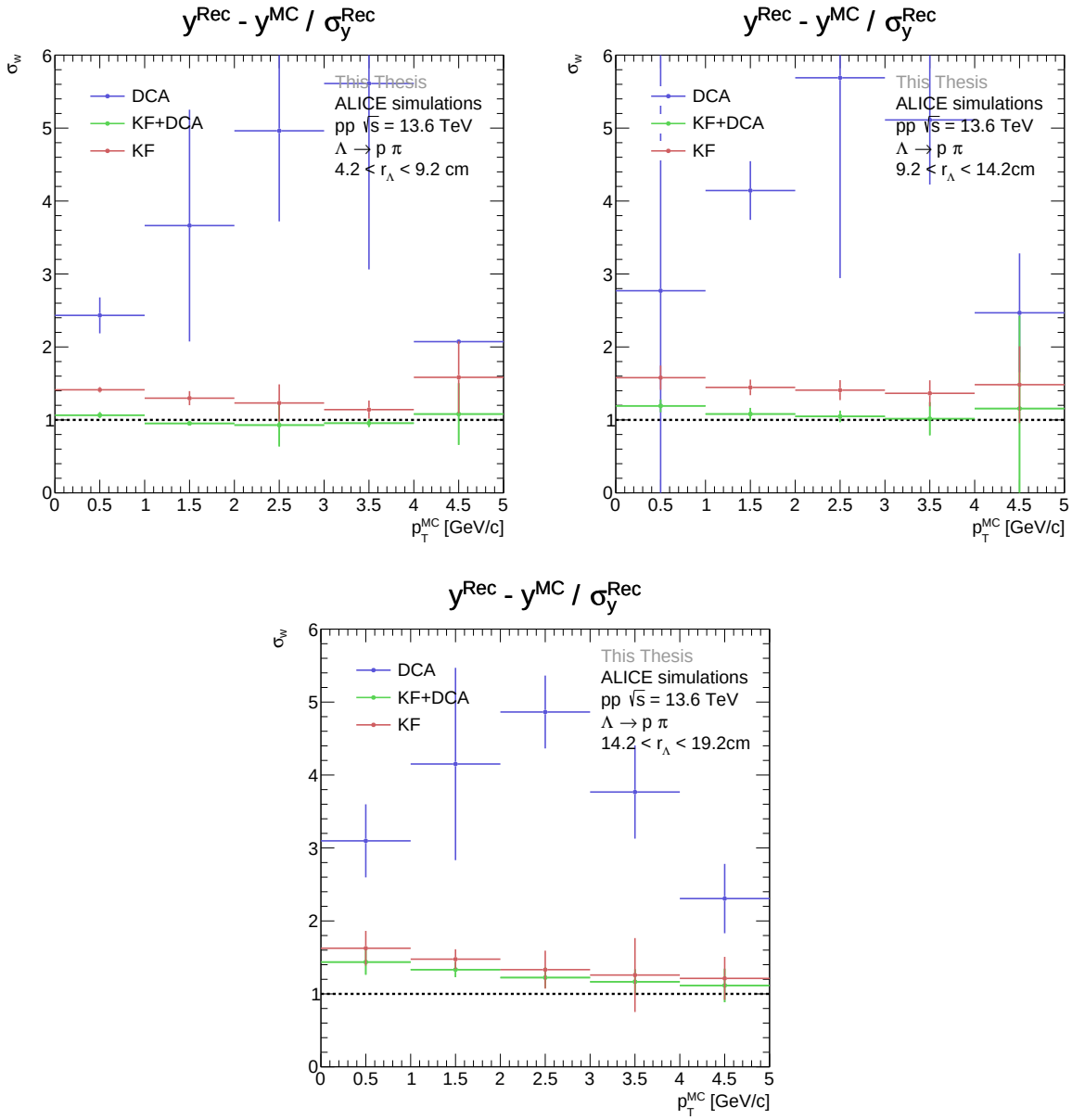

Figure 34: Weighted standard deviations σ_w of secondary vertex pull distributions in y-direction of reconstructed Λ baryons for each reconstruction case in table 6 obtained from triple Gaussian fits as a function of p_{T} corresponding to the case "both at layer no. 3". Top Left: σ_w against p_{T} for $4.2 < r_\Lambda < 9.2$ cm. Top Right: σ_w against p_{T} for $9.2 < r_\Lambda < 14.2$ cm. Bottom: σ_w against p_{T} for $14.2 < r_\Lambda < 19.2$ cm. DCA case: (blue markers). KF+DCA case: (green markers). KF case: (red markers).

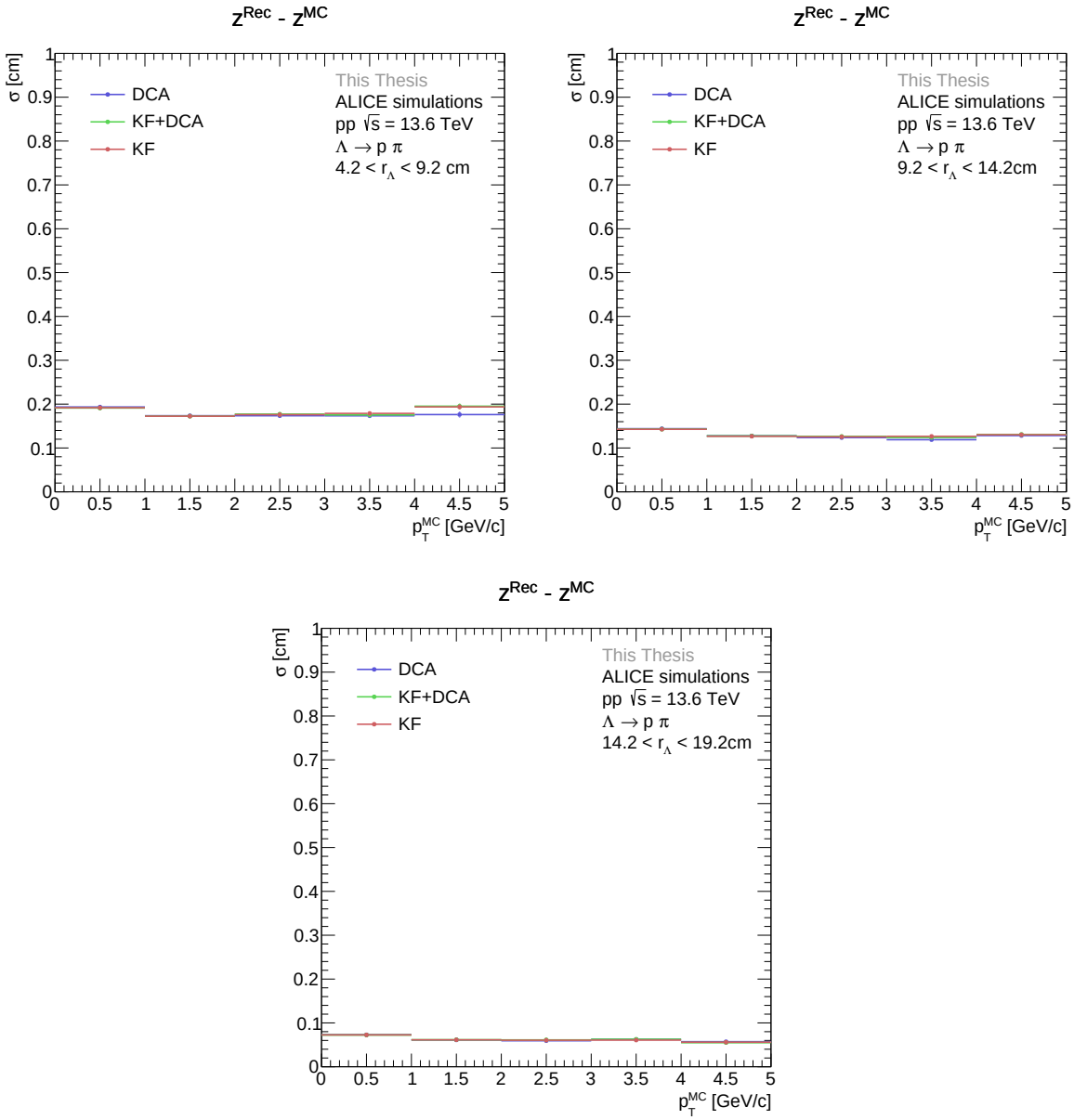

Figure 35: Extracted standard deviations σ of secondary vertex residual distributions in z-direction of reconstructed Λ baryons for each reconstruction case in table 6 as a function of p_{T} corresponding to the case "both at layer no. 3". Top Left: σ against p_{T} for $4.2 < r_{\Lambda} < 9.2$ cm. Top Right: σ against p_{T} for $9.2 < r_{\Lambda} < 14.2$ cm. Bottom: σ against p_{T} for $14.2 < r_{\Lambda} < 19.2$ cm. DCA case: (blue markers). KF+DCA case: (green markers). KF case: (red markers).

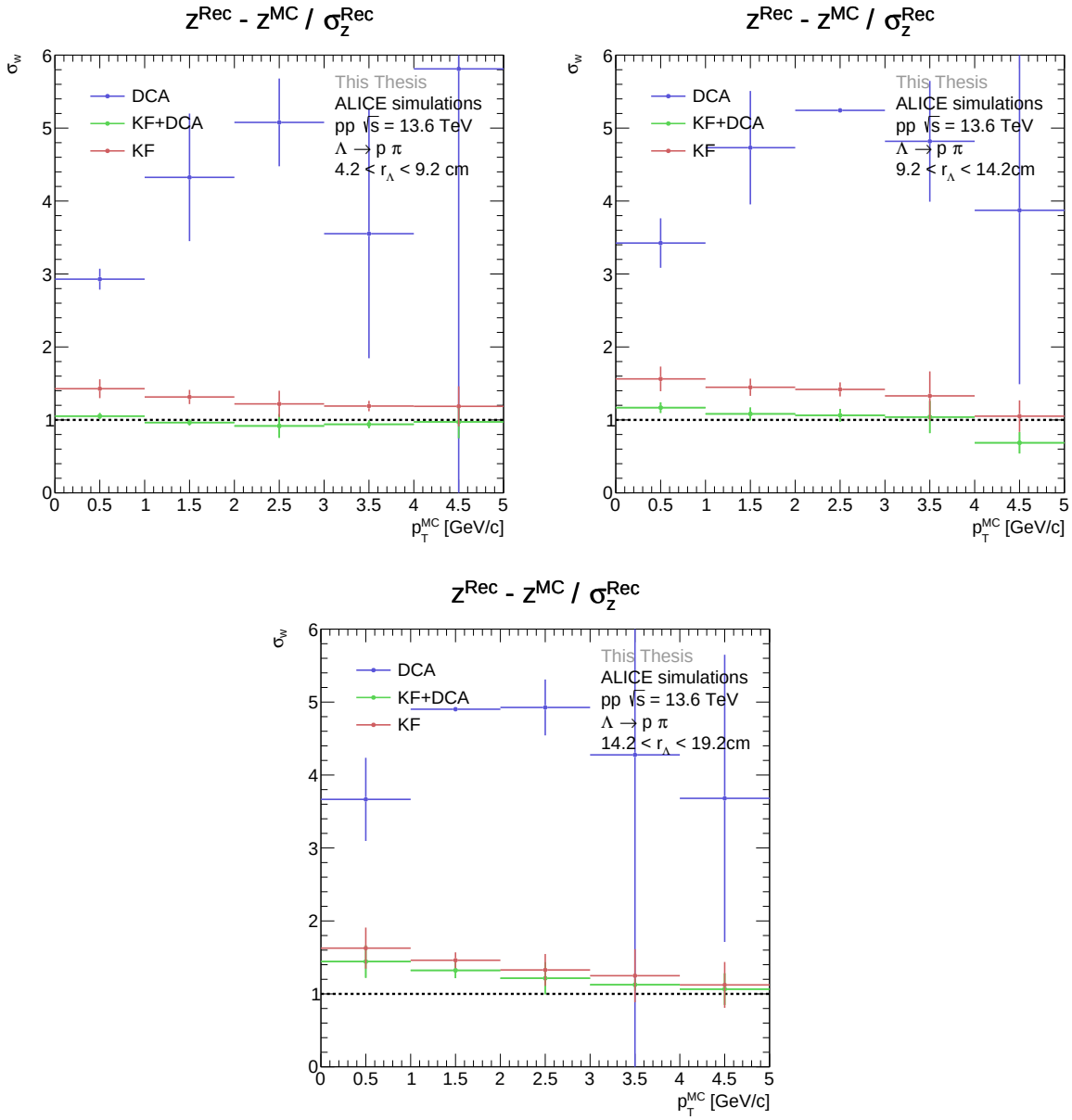

Figure 36: Weighted standard deviations σ_w of secondary vertex pull distributions in z-direction of reconstructed Λ baryons for each reconstruction case in table 6 obtained from triple Gaussian fits as a function of p_{T} corresponding to the case "both at layer no. 3". Top Left: σ_w against p_{T} for $4.2 < r_\Lambda < 9.2$ cm. Top Right: σ_w against p_{T} for $9.2 < r_\Lambda < 14.2$ cm. Bottom: σ_w against p_{T} for $14.2 < r_\Lambda < 19.2$ cm. DCA case: (blue markers). KF+DCA case: (green markers). KF case: (red markers).

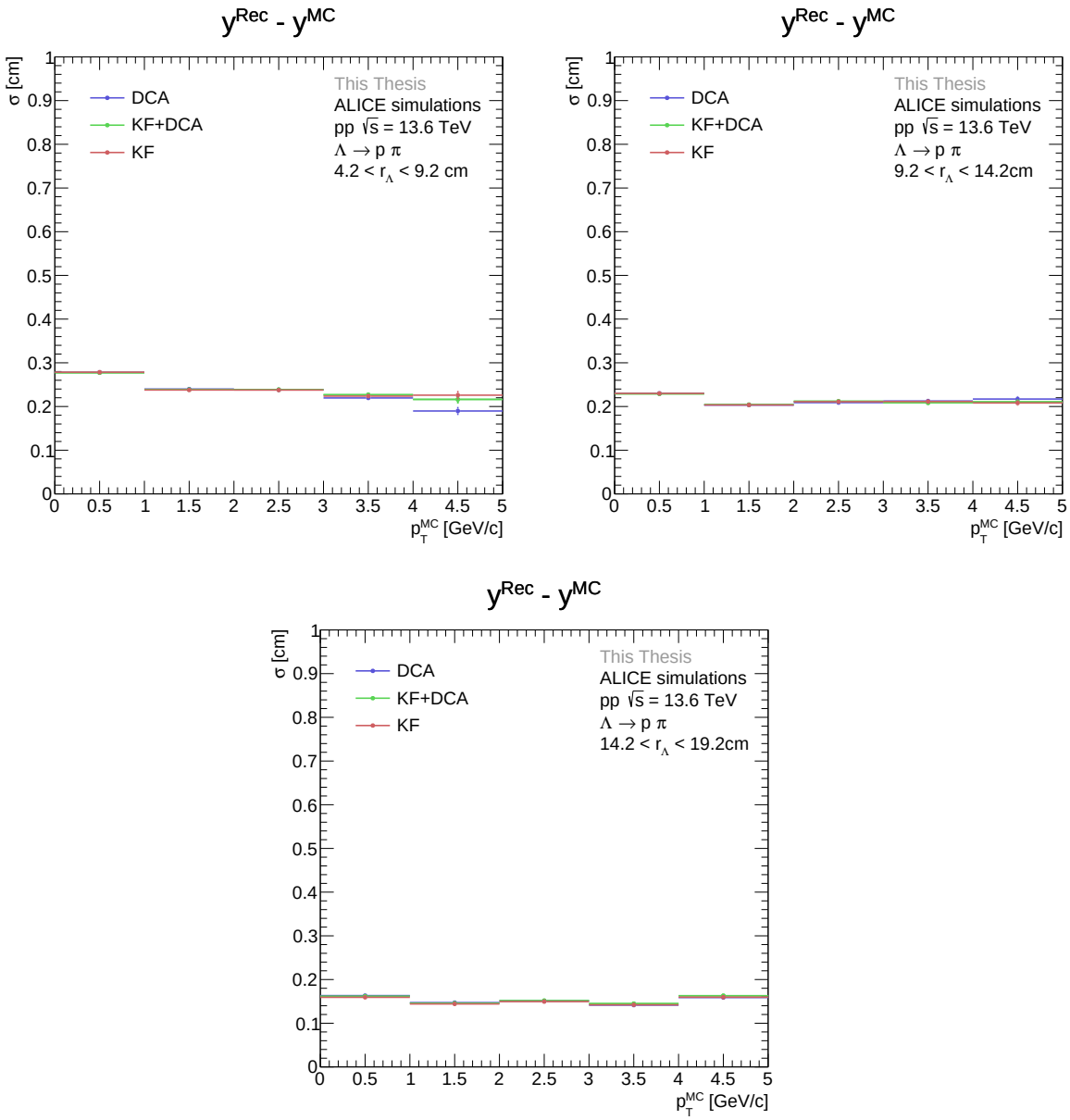

Figure 37: Extracted standard deviations σ of secondary vertex residual distributions in y-direction of reconstructed Λ baryons for each reconstruction case in table 6 as a function of p_{T} corresponding to the case "one at layer no. 3". Top Left: σ against p_{T} for $4.2 < r_{\Lambda} < 9.2$ cm. Top Right: σ against p_{T} for $9.2 < r_{\Lambda} < 14.2$ cm. Bottom: σ against p_{T} for $14.2 < r_{\Lambda} < 19.2$ cm. DCA case: (blue markers). KF+DCA case: (green markers). KF case: (red markers).

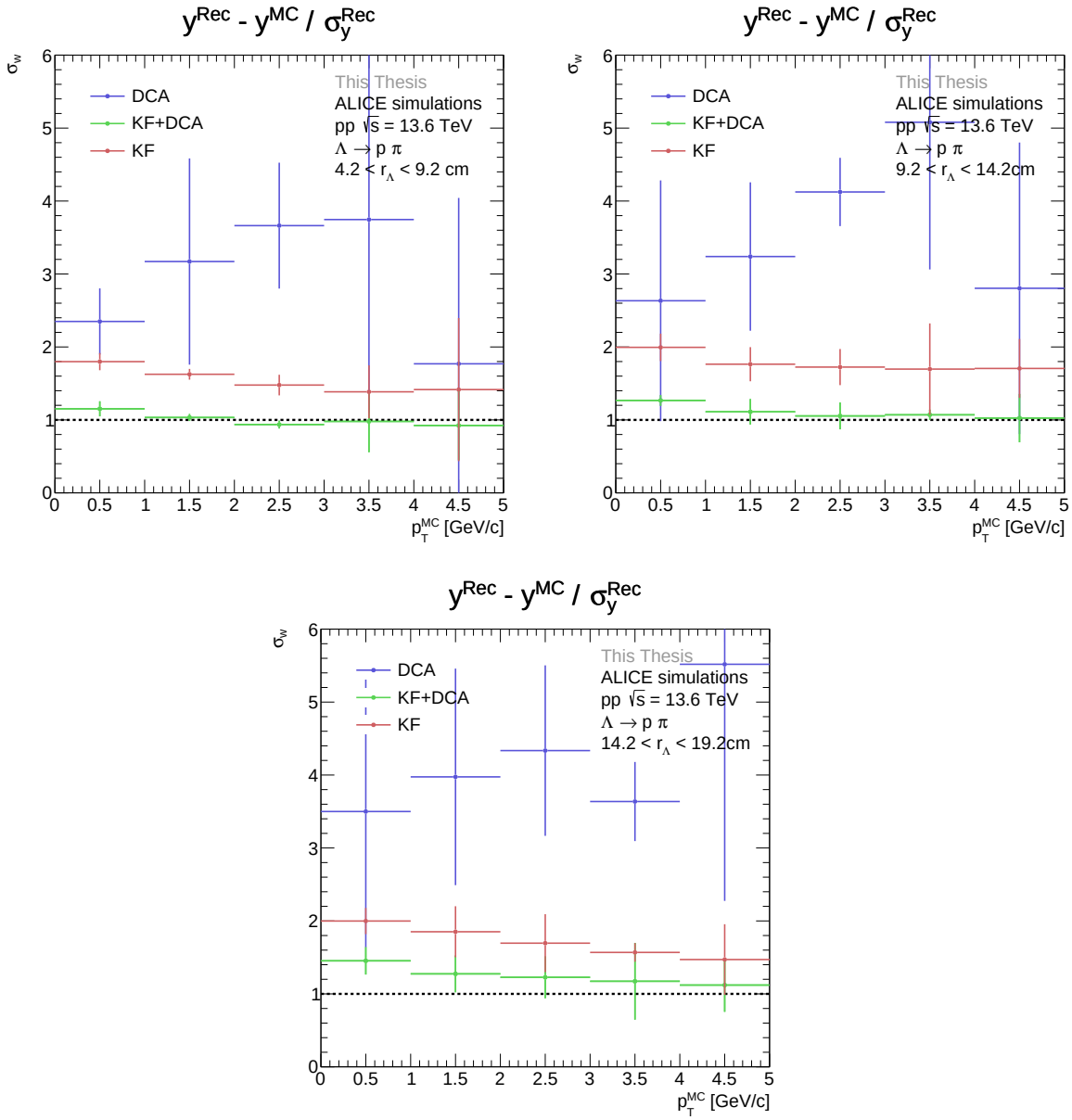

Figure 38: Weighted standard deviations σ_w of secondary vertex pull distributions in y-direction of reconstructed Λ baryons for each reconstruction case in table 6 obtained from triple Gaussian fits as a function of p_{T} corresponding to the case "one at layer no. 3". Top Left: σ_w against p_{T} for $4.2 < r_\Lambda < 9.2$ cm. Top Right: σ_w against p_{T} for $9.2 < r_\Lambda < 14.2$ cm. Bottom: σ_w against p_{T} for $14.2 < r_\Lambda < 19.2$ cm. DCA case: (blue markers). KF+DCA case: (green markers). KF case: (red markers).

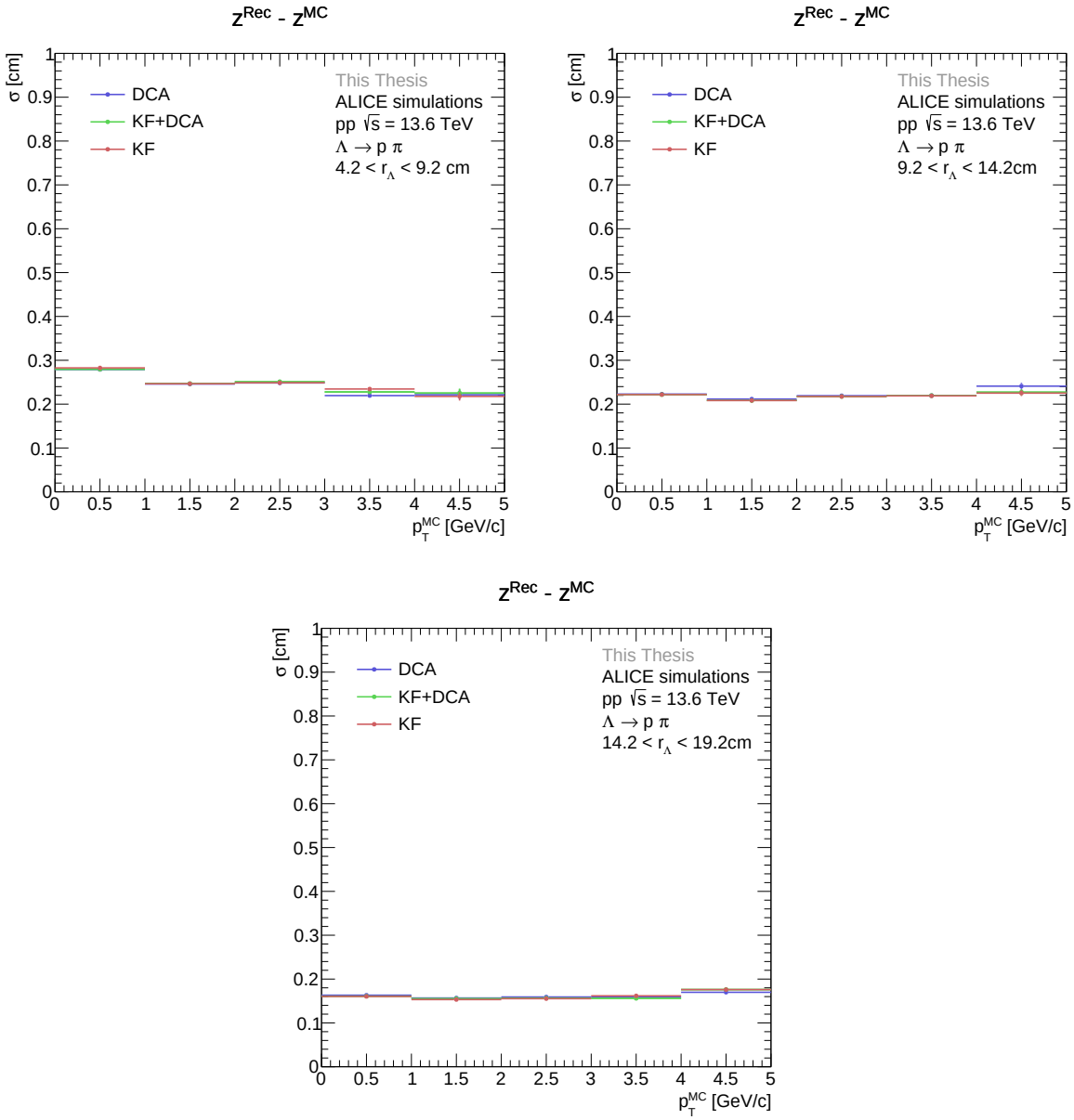

Figure 39: Extracted standard deviations σ of secondary vertex residual distributions in z-direction of reconstructed Λ baryons for each reconstruction case in table 6 as a function of p_{T} corresponding to the case "one at layer no. 3". Top Left: σ against p_{T} for $4.2 < r_{\Lambda} < 9.2$ cm. Top Right: σ against p_{T} for $9.2 < r_{\Lambda} < 14.2$ cm. Bottom: σ against p_{T} for $14.2 < r_{\Lambda} < 19.2$ cm. DCA case: (blue markers). KF+DCA case: (green markers). KF case: (red markers).

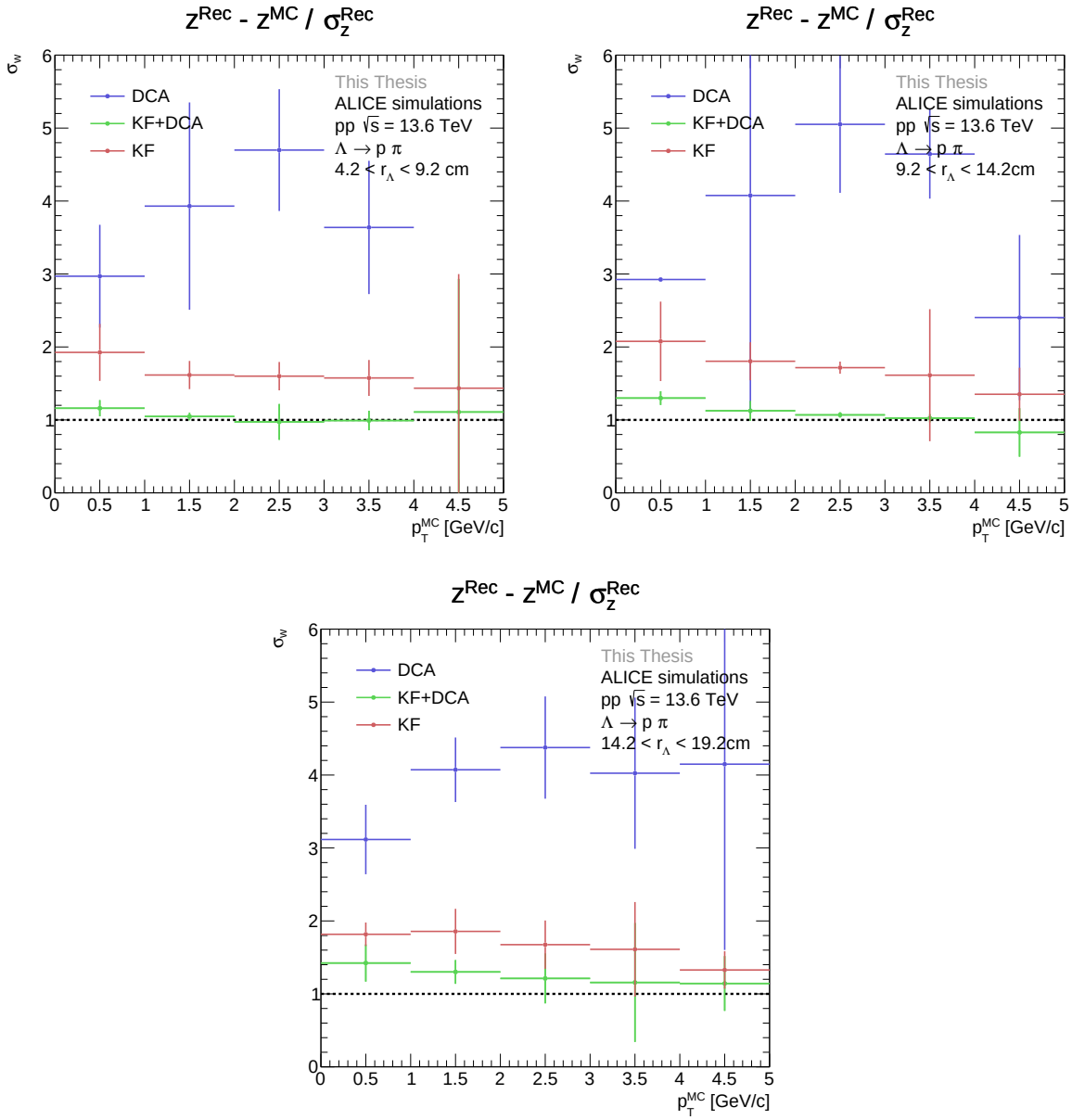

Figure 40: Weighted standard deviations σ_w of secondary vertex pull distributions in z-direction of reconstructed Λ baryons for each reconstruction case in table 6 obtained from triple Gaussian fits as a function of p_{T} corresponding to the case "one at layer no. 3". Top Left: σ_w against p_{T} for $4.2 < r_\Lambda < 9.2$ cm. Top Right: σ_w against p_{T} for $9.2 < r_\Lambda < 14.2$ cm. Bottom: σ_w against p_{T} for $14.2 < r_\Lambda < 19.2$ cm. DCA case: (blue markers). KF+DCA case: (green markers). KF case: (red markers).

Position resolution of Λ baryon daughters

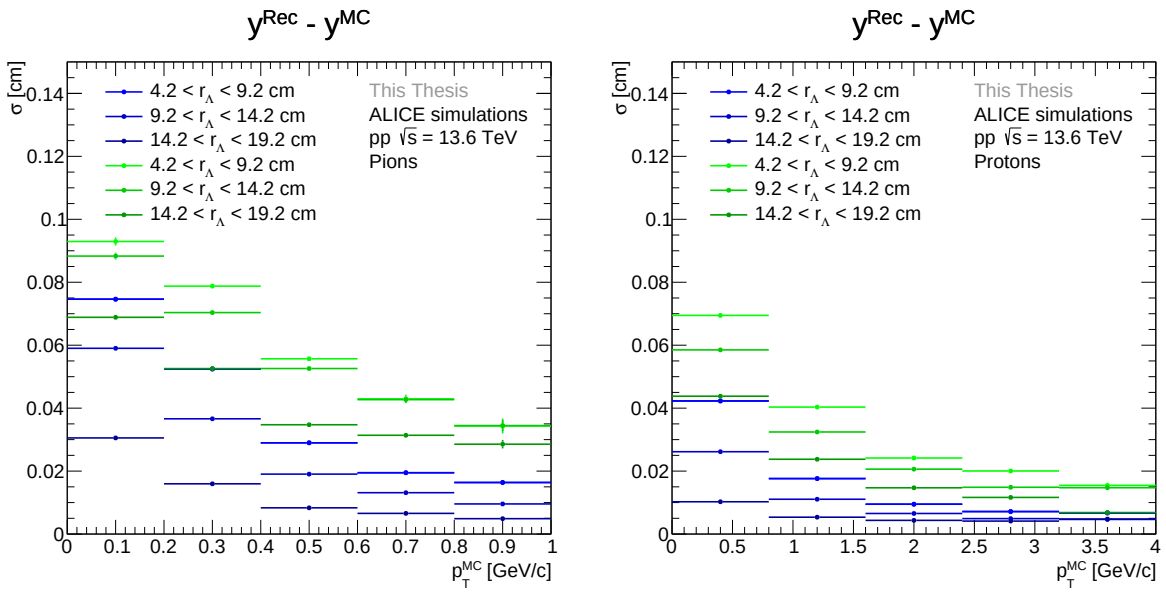

Figure 41: Extracted standard deviations σ of residual distributions of the spatial position in y-direction of protons and pions at the generated Λ decay vertex for each material case in table 8 as a function of p_{T}. Left: σ against p_{T} for pions. Right: σ against p_{T} for protons. "at layer no. 3" case: (blue markers). "at layer no. 4 or no. 5" case: (green markers).

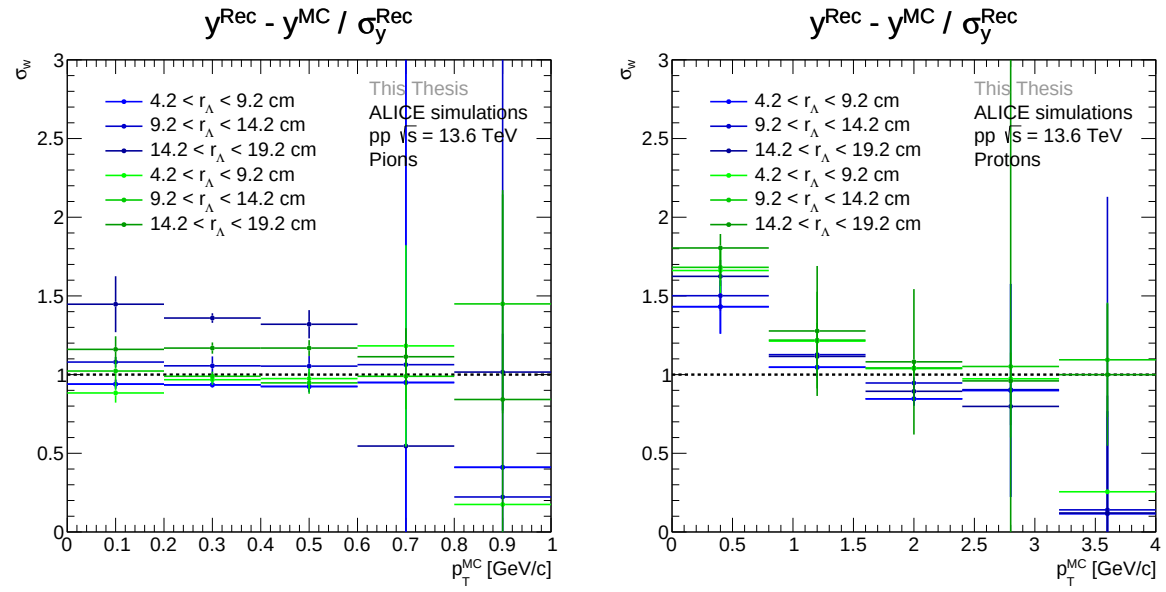

Figure 42: Weighted standard deviations σ of pull distributions of the spatial position in y-direction of protons and pions at the generated Λ decay vertex for each material case in table 8 obtained from triple Gaussian fits as a function of p_{T}. Left: σ_w against p_{T} for pions. Right: σ_w against p_{T} for protons. "at layer no. 3" case: (blue markers). "at layer no. 4 or no. 5" case: (green markers).

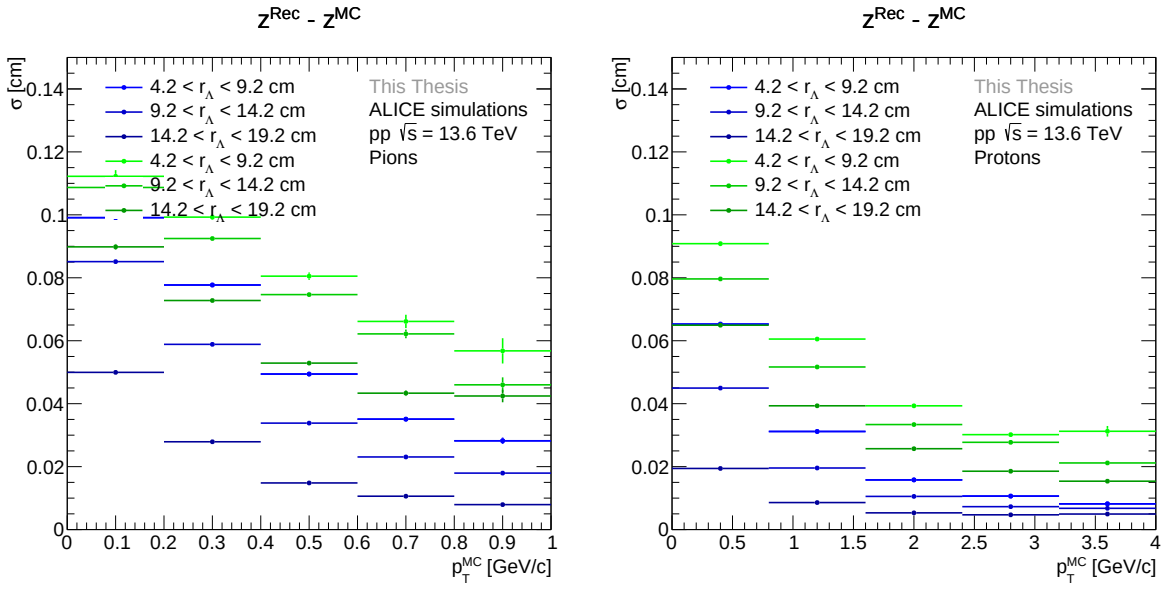

Figure 43: Extracted standard deviations σ of residual distributions of the spatial position in z-direction of protons and pions at the generated Λ decay vertex for each material case in table 8 as a function of p_T. Left: σ against p_T for pions. Right: σ against p_T for protons. "at layer no. 3" case: (blue markers). "at layer no. 4 or no. 5" case: (green markers).

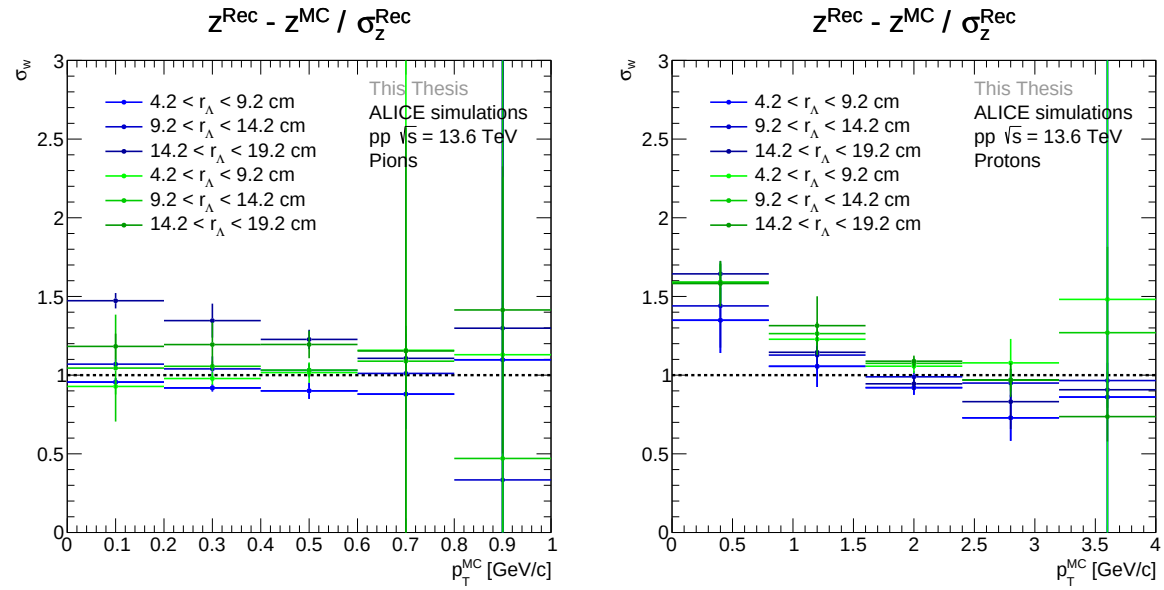

Figure 44: Weighted standard deviations σ of pull distributions of the spatial position in z-direction of protons and pions at the generated Λ decay vertex for each material case in table 8 obtained from triple Gaussian fits as a function of p_T. Left: σ_w against p_T for pions. Right: σ_w against p_T for protons. "at layer no. 3" case: (blue markers). "at layer no. 4 or no. 5" case: (green markers).

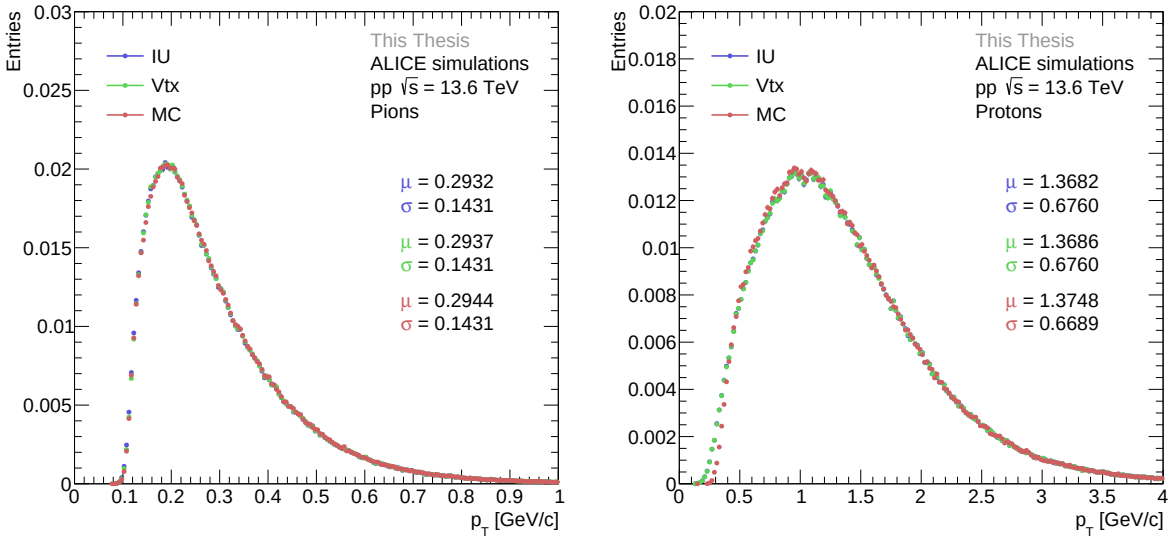

Figure 45: p_{T} distributions of protons and pions at their respective IU and the decay vertex of the Λ baryon as a function of p_{T} with the generated p_{T} spectrum at the decay vertex position. Left: p_{T} of pions. Right: p_{T} of protons. at IU: (green markers). at Vtx: (blue markers). MC: (red markers).

Declaration of Authorship

Ich versichere, dass ich diese Arbeit selbstständig verfasst und keine anderen als die angegebenen Quellen und Hilfsmittel benutzt habe.

Heidelberg, den 17. Juni 2024